Report No. SC5055.21 FR

Copy No. 1

A STUDY OF WALL JETS AND TANGENTIALLY BLOWN WINGS

N.D. Malmuth, W.D. Murphy
Rockwell International Science Center
Thousand Oaks, California 91360

and

J.D. Cole
University of California at Los Angeles
Los Angeles, California 90024

July, 1981

Final Report for Period January 1, 1976 through March 31, 1981

Prepared for

Office of Naval Research
800 N. Quincy Street
Arlington, VA 22217

This research was sponsored by the office of Naval Research under Contract No. N00014-76-C-0350.

Rockwell International
Science Center

Unclassified

SECURITY CLASSIFICATION OF THIS PAGE (When Data Entered)

REPORT DOCUMENTATION PAGE	READ INSTRUCTIONS BEFORE COMPLETING FORM
1. REPORT NUMBER	2. GOVT ACCESSION NO. AD-A106986	3. RECIPIENT'S CATALOG NUMBER
4. TITLE (and Subtitle) (6) A STUDY OF WALL JETS AND TANGENTIALLY BLOWN WINGS.	5. TYPE OF REPORT & PERIOD COVERED Final report for period 01/01/76 thru 03/31/81
	6. PERFORMING ORG. REPORT NUMBER (14) SC5055.21FR
7. AUTHOR(s) (10) N.D. Malmuth, W.D. Murphy and J.D. Cole	8. CONTRACT OR GRANT NUMBER(s) (15) N00014-76-C-0350
9. PERFORMING ORGANIZATION NAME AND ADDRESS Rockwell International Science Center P.O. Box 1085 Thousand Oaks, California 91360	10. PROGRAM ELEMENT, PROJECT, TASK AREA & WORK UNIT NUMBERS NR061-234
11. CONTROLLING OFFICE NAME AND ADDRESS Office of Naval Research 800 N. Quincy Street Arlington, VA 22217 (12) 177	12. REPORT DATE (11) Jul[illegible]981
	13. NUMBER OF PAGES 175
14. MONITORING AGENCY NAME & ADDRESS (If different from Controlling Office) Office of Naval Research 800 N. Quincy Street Arlington, VA 22217	15. SECURITY CLASS. (of this report) Unclassified
	15a. DECLASSIFICATION/DOWNGRADING SCHEDULE

16. DISTRIBUTION STATEMENT (of this Report)

Approved for public release; distribution unlimited.

(9) Final rept. 1 Jan 76-31 Mar 81

17. DISTRIBUTION STATEMENT (of the abstract entered in Block 20, if different from Report)

18. SUPPLEMENTARY NOTES

None

19. KEY WORDS (Continue on reverse side if necessary and identify by block number)

Transonic flow, jets, lift, propulsion systems, shock waves, augmentor wings, partial differential equations.

20. ABSTRACT (Continue on reverse side if necessary and identify by block number)

A study of transonic wall jets and tangentially blown wings has been performed by using asymptotic and computational methods. For the portion of the effort dealing with wall jets, both submerged and coflowing cases have been investigated. For the submerged configurations, the nature of the decay process for disturbances emanating from the jet exit has been examined. In this analysis, the Kutta condition on the nozzle rim can be satisfied merely by requiring streamwise continuity of the potential across the rim as a

DD FORM 1 JAN 73 1473 EDITION OF 1 NOV 65 IS OBSOLETE

Unclassified

SECURITY CLASSIFICATION OF THIS PAGE (When Data Entered)

389949

trailing edge for the flow. With this model, the slip line boundaries create an exponential damped sinusoidal relaxation of the disturbances as compared to algebraic decay for analogous unconfined flows. A similar observation applies to wind tunnel far fields. The nonlinear case differs from the linear one in that the amplitude of the downstream propagated disturbance interacts nonlinearly with the near field in the former case. For these wall jets, acceleration to criticality is accomplished by stream tube contractions and throats induced by upstream influence of the turning. In the coflowing case, selection rules defining various jet flow regimes in terms of the jet transonic similarity parameter and pressure level are given. Conditions are prescribed which define the penetration length for supersonic disturbances downstream from the exit as well as the location of the throats in the jet. The criticality of the flow far downstream is also quantified in terms of these parameters.

Models are described for the complete problem for a tangentially blown airfoil in incompressible and transonic flow. An important feature of these configurations is the foregoing wall jet structures. A systematic theory based on matched asymptotic expansions for the fine structure of the jets away from their exits is developed which shows that in a small deflection approximation the pressure jumps associated with Spence's theory prevail, even if the flow is rotational and compressible. Furthermore, the asymptotic developments provided allow further systematic refinements in which the effects of initial skewness and vorticity inaccessible to other theories can be assessed. A study of the trailing edge region of the blown airfoil problem reveals that for finite trailing edge angles, the dividing streamline leaves tangent to the higher stagnation side if upper and lower stagnation pressure are unequal. If these pressures are equal, the dividing streamline leaves along the bisector. Computational results based on an inviscid model reveal that significant enhancements of lifting pressures are possible with tangential blowing on transonic airfoils. Comparisons with experiment indicate the need for refinements incorporating wave interaction phenomena near the jet exit as well as viscous interaction processes in the downstream portion of the wall jet. Based on this requirement, a finite difference module has been developed which characterizes the development of blown laminar boundary layers and wakes in the transonic regime. Solutions arising from this phase are being utilized to quantify not only viscous interaction effects over blown airfoils, but also the degree of delay in shock-induced separation achievable with slot injection. Substantial downstream movement in the shock-induced separation point has been inexpensively quantified with the computational procedure as compared to experimental methods. The viscous studies show also that the propulsive wake generated by blowing gives a nearly Gaussian normalized velocity profile, in spite of a lack of self similarity which occurs in submerged and self-propelled cases. This result is of significance to assessment of net thrust in experimental simulations and theoretical far field modeling.

TABLE OF CONTENTS

LIST OF TABLES

LIST OF ILLUSTRATIONS

LIST OF ILLUSTRATIONS

LIST OF ILLUSTRATIONS

LIST OF ILLUSTRATIONS

SUMMARY

A study of transonic wall jets and tangentially blown wings has been performed by using asymptotic and computational methods. For the portion of the effort dealing with wall jets, both submerged and coflowing cases have been investigated. For the submerged configurations, the nature of the decay process for disturbances emanating from the jet exit has been examined. In this analysis, the Kutta condition on the nozzle rim can be satisfied merely by requiring streamwise continuity of the potential across the rim as a trailing edge for the flow. With this model, the slip line boundaries create an exponential damped sinusoidal relaxation of the disturbances as compared to algebraic decay for analogous unconfined flows. A similar observation applies to wind tunnel far fields. The nonlinear case differs from the linear one in that the amplitude of the downstream propagated disturbance interacts nonlinearly with the near field in the former case. For these wall jets, acceleration to criticality is accomplished by stream tube contractions and throats induced by upstream influence of the turning. In the coflowing case, selection rules defining various jet flow regimes in terms of the jet transonic similarity parameter and pressure level are given. Conditions are prescribed which define the penetration length for supersonic disturbances downstream from the exit as well as the location of the throats in the jet. The criticality of the flow far downstream is also quantified in terms of these parameters.

Models are described for the complete problem for a tangentially blown airfoil in incompressible and transonic flow. An important feature of these configurations is the foregoing wall jet structures. A systematic theory based on matched asymptotic expansions for the fine structure of the jets away from their exits is developed which shows that, in a small deflection approximation, the pressure jumps associated with Spence's theory prevail, even if the flow is rotational and compressible. Furthermore, the asymptotic developments provided allow further systematic refinements in which the effects of initial skewness and vorticity inaccessible to other theories can be assessed. A study of the trailing edge region of the blown airfoil problem reveals that for finite

trailing edge angles, the dividing streamline leaves tangent to the higher stagnation side if upper and lower stagnation pressures are unequal. If these pressures are equal, the dividing streamline leaves along the bisector. Computational results based on an inviscid model reveal that significant enhancements of lifting pressures are possible with tangential blowing on transonic airfoils. Comparisons with experiment indicate the need for refinements incorporating wave interaction phenomena near the jet exit as well as viscous interaction processes in the downstream portion of the wall jet. Based on this requirement, a finite difference module has been developed which characterizes the development of blown laminar boundary layers and wakes in the transonic regime. Solutions arising from this phase are being utilized to quantify not only viscous interaction effects over blown airfoils, but also the degree of delay in shock induced separation achievable with slot injection. Substantial downstream movement in the shock-induced separation point has been inexpensively quantified with the computational procedure as compared to experimental methods. The viscous studies show also that the propulsive wake generated by blowing gives a nearly Gaussian normalized velocity profile, in spite of a lack of self similarity which occurs in submerged and self-propelled cases. This result is of significance for assessment of net thrust in experimental simulations and theoretical far field modeling.

NOMENCLATURE

a	Characteristic submerged jet height
b	Slip line deflection, b coefficient in boundary layer momentum equation
c	Density ratio ρ_e/ρ in boundary layer, chord length
d	Jet exit height in physical plane
f	wall and airfoil shape function, similarity factor for stream function
g	Jet displacement function
h	Metric coefficient
$\hat{i}$	Unit vector in Cartesian x direction
$\hat{j}$	Unit vector in Cartesian y direction
m	Ratio of kinetic energy per unit mass to freestream stagnation enthalpy
m_i	i = integer, coefficients in boundary layer momentum equation
p	Perturbation pressure, Fourier transform variable
$\hat{q}$	Velocity vector
q	Speed, dynamic pressure
r	Polar radius
s_1	Arc length along airfoil or wall
u	Velocity component in x direction
u′	Velocity perturbation about freestream
v	Velocity component in y direction
w	Complex velocity
x	Cartesian or curvilinear coordinate in freestream direction or along parallel to wall
x^*	Cartesian coordinate in freestream direction
y	Cartesian or curvilinear coordinate normal to freestream or to wall
y^*	Cartesian coordinate normal to freestream direction
z	Complex variable

A	Peak velocity parameter, constant in empirical fit for external pressure in wake region, constant in nose shape
B	Constant in empirical fit of external pressure in wake region, constant in nose shape
C_j	Blowing coefficient
C	Chapman constant
C_{FF}	Far field constant
C_L	Lift coefficient
C_P	Pressure coefficient
D	Reduced exit height
E	Normalized stagnation enthalpy ratio
F	Wall slope function, complex potential
G	Green's function, reduced jet velocity function, pressure gradient parameter, E'
H	Heaviside function, stagnation enthalpy
J	Jet momentum efflux
K	Transonic small disturbance parameter
L	Wall length
M	Mach number, moment of momentum
M_∞	Freestream Mach number
N	Number of supersonic points
P	Pressure
R	Radius of curvature, reflection coefficients
Re	Reynolds number
S	Slip line implicit function for shape
T	Karman Guderley operator
U	Freestream velocity
W	Typical flow quantity
α	Angle of attack, reflection coefficient
β	$\sqrt{M_\infty^2-1}$, Prandtl Glauert factor, angle between dividing streamline and tangent to lower surface
γ	Specific heat ratio

δ	Characteristic flow deflection
δ^*	Displacement thickness
ε	Eddy viscosity
ζ	Boundary layer similarity coordinate
η	Dummy coordinate in y direction, intermediate variable, curvilinear coordinate normal to wall
θ	Momentum thickness, polar angle
λ	Mach number ratio appearing in reflection coefficient
μ	Viscosity
μ_i	i = 1,2,3 quantities appearing in energy equation
ν	Trailing edge angle
ξ	Dummy coordinate in x direction, curvilinear coordinate along parallels to wall
ρ	Density
τ	Characteristic slope of jet free boundaries
ϕ	Perturbation velocity potential in external flow
Ψ	Stream function
ω	Coflowing jet overpressure parameter, angle between dividing streamline and upper surface, vorticity
Δ	Laplacian
Γ	Circulation
Φ	Reduced velocity potential

Subscripts

e	Refers to edge of boundary layer
u	Upper
ℓ	Lower
j	Jet
FF	Far field
SL	Slot
∞	Freestream
ξ	Component in ξ direction

$_n$	Component in $_n$ direction
0	Zeroth order quantity
1	First order quantity

Superscripts

+	Above dividing streamline
-	Below dividing streamline

Special Symbols

$\langle\ \rangle$	Average
[ ]	Jump
$\bar{\ }$	Overbar, refers to average of quantity under it.

1.0 INTRODUCTION

Tangential blowing to avoid the effects of separation on airfoils and to produce supercirculation lift enhancement has received extensive consideration at low speeds. A natural application of these capabilities to current tactical requirements associated with runway denial and ship dispersal is of great military interest. These scenarios strongly suggest the value of V/STOL capability. Predictive models for the aerodynamic characteristics of jet-flapped and upper surface blown wings associated with this application have been primarily addressed through linearized surface singularity and conformal mapping methods.[1-4] Systematic and mathematically consistent procedures integrating viscous effects in such a calculation have received only limited attention, and appear not to have addressed the question of the necessary blowing requirements to avoid separation.

At transonic speeds, tangential blowing has been proposed as a means of mitigating the adverse aerodynamic consequences of shock boundary layer interaction. In particular, the quest for high maneuverability in this Mach number range suggests enhanced buffet-free lift through supercirculation and jet momentum effects. Quantification of these gains as well as others associated with such non-aeronautical applications as circulation controlled rotors, diffusers, convective film cooling, and chemical laser aerodynamic windows requires further knowledge of the structure of the associated wall jets and the nonlinear interaction with the surrounding flow.

Toward obtaining theoretical models which could describe these phenomena, ONR has had a research program, "Transonic Wall Jets and Upper Surface Blown Wings," underway since January 1976. During the course of this investigation, analytical and computational procedures have been utilized to gain further insight into tangentially blown airfoil flows. The work has encompassed detailed investigations of the wall jets and their relationship to the aerodynamic augmentation of the blown airfoils. By contrast to the surface singularity procedures utilized in the other early studies of blown wings, the

effort to be described has utilized computational methods which are capable of handling nonlinear phenomena and viscous interactions that occur in the transonic regime in a mathematically consistent manner.

This report summarizes these studies and provides recommendations for future research. It is based on a number of papers which have been disseminated[5-7] in connection with the contract and other results which will be published in the open literature in the future. The first portion of this report summarizes the early work of the contract dealing with transonic wall jets. In subsequent sections, a study of inviscid phenomena over incompressible and transonic blown wings is provided. Later portions describe recent work in viscous effects dealing with delay of separation and the structure of wakes downstream of propulsive wings.

2.0 A STUDY OF INVISCID SUBMERGED TRANSONIC WALL JETS

An essential element of the flow field over propulsive wings such as those employing upper surface blowing is transonic wall jets. In such phenomena, a transonic primary flow or wall jet entrains an ambient or coflowing stream through turbulent mixing processes.

Existing models for such wall jets stress the incompressible treatment of these phenomena using eddy viscosity and energy methods. Correspondingly, there is a need for simulations that include the effects of nonlinearities, mixed flow, and wave interactions on the development of the wall pressure distributions and overall augmentation forces.

Previous investigations of related phenomena are limited to the treatment of inviscid shockless free jets, and include the work of Chaplygin,[8] Frankl,[9] and Guderley[10], all of which employ hodograph methods. To study shock development and mixed flow phenomena, we have applied modern relaxation methods to treat arbitrary jet exit velocity distributions and assess the influence of an adjacent wall boundary.

In this section, the computational model will be discussed from analytical and numerical viewpoints regarding nonlinear inviscid phenomena. In analogy to unbounded cases such as airfoil flows, the far field is employed to condition the numerical problem and provide useful information about the decay of disturbances. Both free and wall jets are discussed for several examples illustrating various features of this class of flows.

2.1 Formulation

Referring to the physical configuration depicted in Fig. 1, a jet is shown exhausting from the exit OC bounded by the wall OQ and a mixing layer which has been idealized as the slip line CB. This approximation neglects turbulent diffusion processes in the study of wave interactions with the shear layer, but these phenomena can be incorporated in later refinements. Furthermore, it will be assumed that wall and jet turning angles are small. In

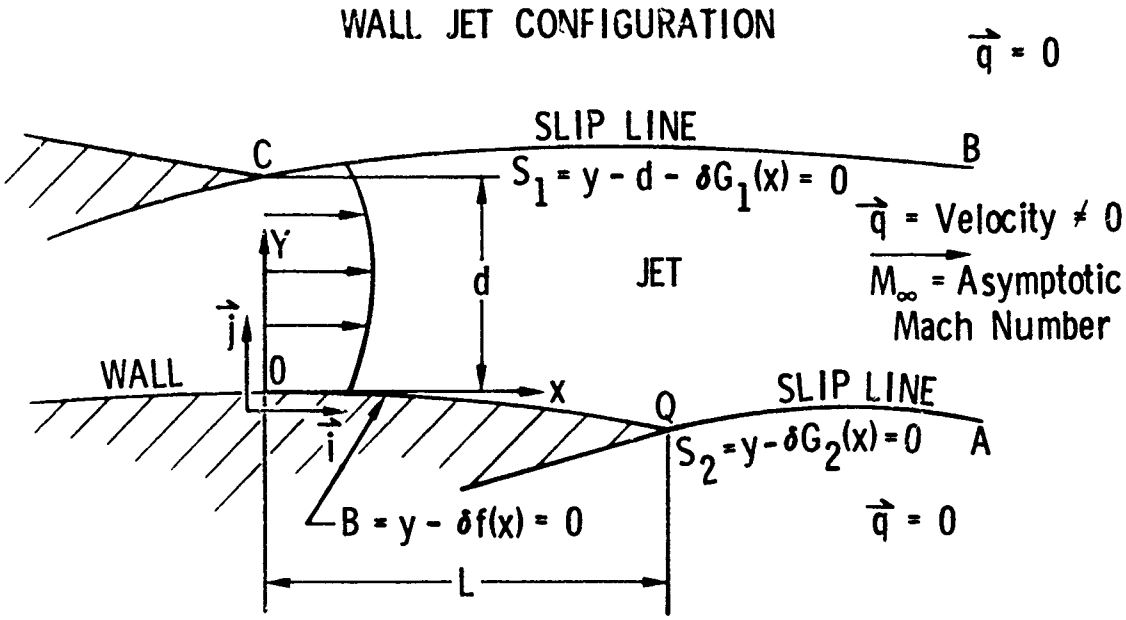

Fig. 1 Wall jet configuration.

contrast to the usual jet formulations, in which an upstream cowl shape is specified, or stagnation conditions are assumed,[8-12] this analysis will treat a specified exit Mach number distribution. Additional assumptions are irrotationality and subsonic conditions infinitely far downstream. The methods applied here can be generalized to cases where these restrictions are not present. Finite length walls OQ are considered in keeping with relevance to upper surface blown wings and other propulsive lift devices.

Returning to Fig. 1, the equations of slip lines $S_1(x,y)$, $S_2(x,y)$, and the wall boundary $B(x,y)$ are assumed as

$$\text{CB:}\quad S_1 = y - d - \delta G_1(x) = 0$$

$$\text{QA:}\quad S_2 = y - \delta G_2(x) = 0$$

$$\text{OQ:}\quad B = y - \delta f(x) = 0$$

where δ is a characteristic flow deflection parameter. In a small disturbance limit, in which the scaled jet exit height $D \equiv d\delta^{1/3}$, the wall length L, and the transonic similarity parameter $K = (1 - M_\infty^2)/\delta^{2/3}$ are held fixed, $\delta \to 0$, the asymptotic expansions of the velocity, pressure P, and density ρ are*

$$\frac{\vec{q}}{U}(x,y;M_\infty,\delta,d,L) = [1 + \delta^{2/3}\Phi_x(x,Y;K,D,L) + \ldots]\vec{i} + [\delta\Phi_y + \ldots]\vec{j} \qquad (1.1a)$$

$$P/P_\infty \doteq 1 - \gamma\delta^{2/3}\Phi_x + \ldots \qquad (1.1b)$$

$$\rho/\rho_\infty \doteq 1 + \delta^{2/3}\sigma + \ldots \qquad (1.1c)$$

where the subscript ∞ signifies conditions at $x = \infty$, Φ is the perturbation potential, P_∞ is the ambient pressure, $U = a_\infty M_\infty$, $a_\infty^2 = \gamma P_\infty/\rho_\infty$, ρ_∞ is the density, a_∞ is the speed of sound, $\vec{q}$ is the flow velocity, and the scaled coordinate $Y = \delta^{1/3}y$ is also fixed in the limit. If a further transformation is introduced in which $\tilde{y} = \sqrt{K}\,Y$, a boundary value problem can be formulated for the case of an elliptic far field. The region can be considered as the rectangular

*Equations are numbered consecutively from the beginning of each section. References to equations in other sections provide the section number of the referenced equation.

domain shown in Fig. 2, corresponding to transfers of the boundary conditions to the appropriate undisturbed streamlines allowed by the small disturbance limit. Dropping the tildes, the following small disturbance equation holds inside OQABCO

$$\Delta\phi \equiv (\partial^2/\partial x^2 + \partial^2/\partial y^2)\phi = (\gamma+1)(\partial u^2/\partial x)/2K \quad , \quad (u \equiv \phi_x) \tag{1.2}$$

where we define function $\bar{u}$ and ϕ such that

$$u(x,y) = \bar{u},(x,y)$$
$$\phi(x,y) = \phi(x,Y) \quad .$$

Invoking continuity of pressure and flow tangency along the slip lines, we have with $a \equiv D\sqrt{K}$

$$\phi(x,a) = 0 \tag{1.3a}$$

$$\phi_y(x,a) = G_1'(x) \quad , \quad 0 < x < \infty \tag{1.3b}$$

$$\phi(x,0) = C_1 \quad , \quad L < x < \infty \tag{1.3c}$$

$$\phi_y(x,0) = G_2'(x) \quad , \quad L < x < \infty \tag{1.3d}$$

where the constant C_1 is to be computed by iteration. In this approximation, the slip lines are therefore not truly free, the unknown functions G_i' being computed from the solution by a simple differentiation. The remaining boundary conditions are

$$\phi_y(x,0) = f'(x) \equiv F(x) \quad , \; 0 < x < L \tag{1.3e}$$

$$\phi_x(0,y) = h(y) = H(Y) \; . \tag{1.3f}$$

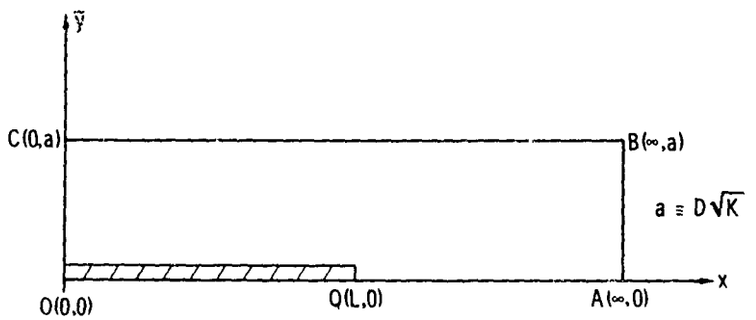

Fig. 2 Transformed wall jet domain.

Equation (1.3f) is representative of the initial exit velocity profile which conceivably is determined by the upstream duct contour and stagnation pressure.

2.2 Far Field

To complete the formulation of the problem for subsonic conditions far downstream, the asymptotic behavior is derived in this section. On introducing a Green's function G, satisfying homogeneous Dirichlet conditions on OA and CB and homogeneous Neumann conditions on OC and AB in Fig. 2 with

$$\Delta G = \delta(P,Q) \equiv \delta(x-\xi)\delta(y-\eta)$$

where $Q(\xi,\eta)$ is the source point and P is the field point, Green's theorem applied to the region OQABCO gives the following integrodifferential equation for ϕ

$$\phi = \sum_{i=1}^{4} I_i \ ,$$

where

$$I_1 = \frac{\gamma+1}{2K} \int_0^\infty d\xi \int_0^a G(x,y;\xi,\eta)(\partial u^2/\partial\xi)d\eta$$

$$I_2 = -\int_0^L \phi(\xi,0)\, \frac{\partial G}{\partial \eta}\,(x,y;\xi,\eta)d\xi$$

$$I_3 = -C_1 \int_L^\infty \frac{\partial G}{\partial \eta}\,(x,y;\xi,0)d\xi$$

$$I_4 = \int_0^a h(\eta)G(x,y;0,\eta)d\eta \ .$$

The quantity G may be obtained from the cosine transform where

$$\bar{G} = \int_0^\infty G \cos px \, dx$$

$$G = \frac{2}{\pi} \int_0^\infty \bar{G} \cos px \, dp \ .$$

The subsidiary equations for $\bar{G}$ are

$$\frac{d^2\bar{G}}{dy^2} - p^2\bar{G} = \delta(y-\eta)\cos p\xi \Rightarrow \left[\frac{d\bar{G}}{dy}\right]_{y=\eta} \equiv \left(\frac{d\bar{G}}{dy}\right)_{y=\eta+} - \left(\frac{d\bar{G}}{dy}\right)_{y=\eta-}$$

$$= \cos p\xi\,[\bar{G}]_{y=\eta} \equiv (G)_{y-\eta+} - (G)_{y=\eta-} = 0$$

$$\bar{G}(p,0;\xi,\eta) = \bar{G}(p,a;\xi,\eta) = 0 \ ,$$

implying that

$$\bar{G} = \frac{\sinh p(\eta-a)\,\sinh py\,\cos p\xi}{p\,\sinh pa} \ , \ y < \eta \qquad (1.4a)$$

$$= \frac{\sinh p\eta\,\sinh p(y-a)\,\cos p\xi}{p\,\sinh pa} \ , \ y > \eta \ . \qquad (1.4b)$$

Equations (1.4) can be inverted by a treatment of appropriate contour versions for the inversion integrals, initially, without the $\cos p\xi$ factor and, subsequently including it, using the shift theorem. To obtain convergence and exponential decay of the integrand, the appropriate closure for the contour is a large semicircle $|p| = R$, $R \to \infty$, with $\mathrm{Im}\ p \gtrless 0$ for $x \gtrless 0$. Summing the residues at the poles $p = n\pi i$, $n = (\mathrm{sgn}x)(1,2,3,\ldots)$, gives the following final expression for G:

$$-\pi G = \sum_{1}^{\infty} n^{-1} \sin n\alpha y \, \sin n\alpha\eta \, \{e^{-n\alpha(x+\xi)} + e^{-n\alpha|x-\xi|}\} \qquad (1.5)$$

$$\alpha \equiv \pi/a \ .$$

Equation (1.5) is valid for $y \gtrless \eta$, $x \gtrless \xi$, and can be summed as the integral of a geometric series giving

$$-2\pi G = S(\alpha(x+\xi),\alpha(\eta+y)) + S(\alpha(x+\xi),\alpha(\eta-y))$$

$$- S(\alpha|x-\xi|,\alpha(\eta+y)) - S(\alpha|x-\xi|,\alpha(\eta-y))$$

$$\Rightarrow G = \frac{1}{4\pi} \ell n \left\{ \left[\frac{1-\cos\alpha(\eta-y)\,\mathrm{sech}\alpha(x+\xi)}{1-\cos\alpha(\eta+y)\,\mathrm{sech}\alpha(x+\xi)} \right] \times \left[\frac{1-\cos\alpha(\eta-y)\,\mathrm{sech}\alpha(x-\xi)}{1-\cos\alpha(\eta+y)\,\mathrm{sech}\alpha(x-\xi)} \right] \right\} \qquad (1.5')$$

where

$$S(A,B) \equiv \sum_{1}^{\infty} n^{-1} e^{-nA} \cos nB = -\ell n|1-e^{-z}|$$

$$= -\frac{1}{2} \ell n(1-2e^{-A}\cos B + e^{-2A})$$

$$z \equiv A + iB \ .$$

An inspection of these formulas reveals that G is exponentially small as $x \to \infty$, and is logarithmically singular at the source point, as anticipated.

Based on (1.5), the dominant term of the asymptotic expansion of I_1 as $x \to \infty$ is given by the formula

$$I_1 \sim \frac{\gamma+1}{aK} e^{-\alpha x} \sin\alpha y \int_0^a \sin\alpha\eta\, d\eta \int_0^x u^2 \sinh\alpha\xi\, d\xi \qquad (1.6)$$

where in the evaluation,* the contribution of the simple pole of G_ξ vanishes, and integrals of the form

$$\int_0^a d\eta \int_0^\infty e^{-\alpha|x-\xi|} f(\xi,\eta)\, d\xi$$

and

$$\int_0^a d\eta \int_0^\infty e^{-\alpha(x+\xi)} f(\xi,\eta)\, d\xi \qquad (1.7)$$

*The upper limit of the inner integral can be interpreted as ∞ to within terms of higher order involving $e^{-\alpha x}$ as $x \to \infty$. This interpretation is made in Eq. (1.8).

arise. The multiplication by u^2 of the asymptotic expansion represented by (1.5) as $x \to \infty$ and its subsequent integration with respect to ξ formally gives a development dominated by these integrals. Writing the inner integral of the first of (1.7) as

$$\int_0^\infty e^{-\alpha|x-\xi|} f(\xi,\eta)d\xi = e^{-\alpha x}\int_0^x e^{\alpha\xi} f(\xi,\eta)d\xi + e^{\alpha x}\int_x^\infty e^{-\alpha\xi} f(\xi,\eta)d\xi \quad ,$$

and if the $e^{-\alpha x}$ factor of the first integral on the left-hand side is indicative of the behavior of ϕ as $x \to \infty$, then u^2 and f are $\mathcal{O}(e^{-2\alpha\xi})$ in this limit. If u^2 and f are bounded on the range of integration, the first integral converges and the second is $\mathcal{O}(e^{-2\alpha x})$ as $x \to \infty$. The second integral in (1.7) requires no such decomposition and is also convergent; hence, (1.6) follows. Evaluating the remaining integrals and using (1.5) and (1.5'), the final expression for the far-field is

$$\phi \triangleq \phi_{FF} = C_1(1-Y^*) + C_{FF}e^{-x^*}\sin\pi Y^* + \mathcal{O}(e^{-2x^*}) \text{ as } x \to \infty \qquad (1.8a)$$

where

$$C_{FF} \equiv \frac{\gamma+1}{DK}\int_0^D \sin\pi Y^* dY \int_0^\infty \phi_x^2(\xi,Y)\sinh\xi^* d\xi$$

$$- \frac{2\sqrt{K}}{\pi}\int_0^D H(Y)\sin\pi Y^* dY + \frac{2}{D\sqrt{K}}\int_0^L \Phi(\xi,0)\cosh\xi^* d\xi - 2C_1\sinh L^* \qquad (1.8b)$$

$$x^* \equiv \pi x/D\sqrt{K} \quad , \quad \xi^* \equiv \pi\xi/D\sqrt{K} \quad , \quad L^* \equiv \pi L/D\sqrt{K} \quad , \quad Y^* \equiv Y/D \quad .$$

2.3 Numerical Analysis

The numerical procedure is similar to one first developed by Murman[13] and extended by Jameson[14] and Bailey and Ballhaus.[15] Briefly, the transonic potential equation in divergence form is discretized by using central

differences when the equation is elliptic, and backward differences when it is hyperbolic. Thus, we may write

$$(K\Phi_x - \tfrac{\gamma+1}{2}\Phi_x^2) + (\Phi_Y)_Y$$

$$\approx (1-\mu_i)(K(\Phi_{xi+1/2}-\Phi_{xi-1/2}) - \tfrac{\gamma+1}{2}(\Phi^2_{xi+1/2}-\Phi^2_{xi-1/2}))/p_i$$

$$+ \mu_{i-1}(K(\Phi_{xi-1/2}-\Phi_{xi-3/2}) - \tfrac{\gamma+1}{2}(\Phi^2_{xi-1/2}-\Phi^2_{xi-3/2}))/p_i$$

$$+ (\Phi_{Yj+1/2} - \Phi_{Yj-1/2})/q_j \qquad (2.1)$$

$$\approx (1-\mu_i)\left[K - \frac{\gamma+1}{2}\left(\frac{\Phi_{i+1}-\Phi_i}{p_{i+1/2}} + \frac{\Phi_i-\Phi_{i-1}}{p_{i-1/2}}\right)\right]$$

$$\times\left[\frac{\Phi_{i+1}-\Phi_i^+}{p_{i+1/2}p_i} - \frac{\Phi_i^+-\Phi_{i-1}^+}{p_i p_{i-1/2}}\right]$$

$$+ \mu_{i-1}\left[K - \frac{\gamma+1}{2}\left(\frac{\Phi_i-\Phi_{i-1}}{p_{i-1/2}} + \frac{\Phi_{i-1}-\Phi_{i-2}}{p_{i-3/2}}\right)\right]$$

$$\times\left[\frac{\Phi_i^*-\Phi_{i-1}^+}{p_{i-1/2}p_i} - \frac{\Phi_{i-1}^+-\Phi_{i-2}}{p_i p_{i-3/2}}\right] + \frac{\Phi_{j+1}^+-\Phi_j^+}{q_j q_{j+1/2}} - \frac{\Phi_j^+-\Phi_{j-1}^+}{q_j q_{j-1/2}} \qquad (2.2)$$

where the missing subscript is j when only i's are present and i when only j's are present. For example, $\Phi_{i-1} \equiv \Phi_{i-1,j}$ and $\Phi_{j+1} \equiv \Phi_{i,j+1}$. Also,

$$p_i = (x_{i+1} - x_{i-1})/2 \qquad q_j = (Y_{j+1} - Y_{j-1})/2$$

$$p_{i-3/2} = x_{i-1} - x_{i-2} \qquad q_{j-1/2} = Y_j - Y_{j-1}$$

$$p_{i-1/2} = x_i - x_{i-1} \qquad q_{j+1/2} = Y_{i+1} - Y_j$$

$$p_{i+1/2} = x_{i+1} - x_i$$

and

$$\mu_i = \begin{cases} 0 & \text{if the point } (x_i, Y_j) \text{ is elliptic} \\ 1 & \text{if the point } (x_i, Y_j) \text{ is hyperbolic} \end{cases} .$$

If one defines

$$VC_i \equiv K - \frac{\gamma+1}{2}\left(\frac{\Phi_{i+1} - \Phi_i}{p_{i+1/2}} + \frac{\Phi_i - \Phi_{i-1}}{p_{i-1/2}}\right) ,$$

then

$$\mu_i = \begin{cases} 0 & \text{if } VC_i > 0 \\ 1 & \text{if } VC_i < 0 \end{cases} .$$

Here, the iterations are viewed as steps in pseudotime with Φ^+ (NEW) and Φ (OLD) values. In addition,

$$\frac{\Phi_i^*}{p_{i-1/2}p_i} \equiv \Phi_i^+\left(\frac{1}{p_i p_{i-1/2}} + \frac{1}{p_i p_{i-3/2}}\right) - \Phi_i\left(\frac{1}{p_i p_{i-3/2}}\right)$$

These definitions guarantee that the linearized difference algorithm satisfies the von Neumann stability criterion. (See Jameson[14] for the proof.)

Overrelaxation is employed in the elliptic region ($\mu_{i,j} = \mu_{i-1,j} = 0$) only. First, define

$$e_1 \equiv 1/p_i p_{i-1/2} \quad , \quad e_3 \equiv 1/p_i p_{i+1/2} \quad ,$$

and

$$e_2 \equiv e_1 + e_3 \quad .$$

Then, the elliptic difference expression in Eq. (2.2) given by

$$\left[\frac{\Phi_{i+1}-\Phi_i^+}{p_{i+1/2}p_i} - \frac{\Phi_i^+-\Phi_{i-1}^+}{p_i p_{i-1/2}}\right] = e_1\Phi_{i-1}^+ - e_2\Phi_i^+ + e_3\Phi_{i+1}$$

is replaced by

$$e_1\Phi_{i-1}^+ - \Phi_i^+ e_2/\omega - \Phi_i e_2(1-1/\omega) + e_3\Phi_{i+1}$$

where ω is the overrelaxation parameter, i.e., $1 < \omega < 2$. Note that if $\omega = 1$, there is no change between the two expressions.

To improve stability near the sonic points, especially if a discontinuous wall ooundary condition is being considered, it was found necessary, as in Bailey and Ballhaus,[15] to add to Eq. (2.1) the term

$$\frac{\varepsilon\Delta t}{x_i - x_{i-1}}\Phi_{xt} = \varepsilon\frac{(\Phi_i^+ - \Phi_i) - (\Phi_{i-1}^+ - \Phi_{i-1})}{(x_i - x_{i-1})^2}$$

where ε is chosen to be in the range $0 < \varepsilon < .5$.

Boundary Conditions

The boundary conditions $\Phi(x,D) = 0$ and $\Phi_Y(x,0) = f'(x)$ may be incorporated into the numerical scheme by using the same techniques described in Murman and Cole.[16] Discussed first will be the boundary condition at the jet exit $x = 0$, which may be one of two types: (A) subsonic at the jet exit, or (B) partially or completely supersonic at the jet exit. The far field boundary condition will be treated later.

(A) Subsonic at the Jet Exit

Here the boundary condition is

$$\Phi_X(0,Y) = H(Y) \qquad 0 < Y < D$$

where

$$K - (\gamma+1)H(Y) > 0 \quad \text{for} \quad 0 < Y < D \quad .$$

In this case, let $x_{1/2} = 0$, $x_1 - x_{1/2} = \Delta x/2$, $\mu_0 = 0$, and $\mu_1 = 0$; it is also required that $x_2 - x_1 = \Delta x$. Then, the derivatives in Eqs. (2.1) and (2.2) become

$$\left[K(\Phi_{x3/2} - \Phi_{x1/2}) - \frac{\gamma+1}{2}(\Phi^2_{x3/2} - \Phi^2_{x1/2})\right]\Big/\Delta x$$

$$= \left[K - \frac{\gamma+1}{2}(\Phi_{x3/2} + \Phi_{x1/2})\right]\left[\Phi_{x3/2} - \Phi_{x1/2}\right]\Big/\Delta x$$

$$= \left[K - \frac{\gamma+1}{2}\left(\frac{\Phi_2-\Phi_1}{\Delta x} + H(Y)\right)\right]\left[\frac{\Phi_2-\Phi_1}{\Delta x} - H(Y)\right]\Big/\Delta x \quad .$$

(B) Partially or Completely Supersonic at the Jet Exit

For this case, two boundary conditions are required at x = 0; namely,

$$\Phi_x(0,Y) = H(Y) \qquad 0 < Y < D$$

and

$$\Phi(0,Y) = g(Y) \quad \text{for} \quad Y \in [0,D]$$

where

$$K - (\gamma+1)H(Y) < 0 \quad .$$

For all points $Y \in [0,D]$ in which $K - (\gamma+1)H(Y) > 0$, $g(Y)$ need not exist.

If a point (x_1,Y_j) is elliptic, the discretization given in case (A) is used. On the other hand, if (x_1,Y_j) is hyperbolic, it is assumed that the grid may be extended to the left by $\Delta x/2$, and that $x_0 = 0$, $x_{-1} = -\Delta x/2$, and $\Phi_{0j} = \Phi(0,Y_j) = g(Y_j)$.

Using Taylor's tneorem,

$$\Phi_{-1,j} = \Phi_{0j} - \Delta x \Phi_x(0,Y_j)/2 = g(Y_j) - \Delta x H(Y_j)/2 \quad .$$

These values for Φ_{0j} and $\Phi_{-1,j}$ may now be substituted into Eq. (2.2) in the normal way, and line relaxation may be applied to the first column of unknowns along $x = x_1$.

The far field boundary conditions given by Eq. (1.8) contain two unknown constants, C_1 and C_{FF}, which must be determined in an iterative fashion. The basic technique holds C_{FF} fixed while C_1 changes until the solution converges. Then, C_{FF} is updated by evaluating the integrals in Eq. (1.8b), and the procedure is repeated until C_{FF} also converges. In order to

determine C_1, the mesh network is swept from left to right by using line relaxation. After the potential is computed on the line x = L, extrapolation of the interior points yields $\Phi(L,0) \equiv \Phi_L$. If it is assumed only that Φ is continuous at x = L, then $C_1 = \Phi(L,0) = \Phi(x,0)$ for x > L, which guarantees that $\Phi_x(x,0) = 0$ for x > L.

Singular Behavior Near Wall Trailing Edge

It is physically plausible that a Kutta condition given by

$$\phi_x(L-,0) = \phi_x(L+,0) = 0 \tag{3}$$

is satisfied by the solution for trailing edge neighborhoods in unmixed flow. Because of (3), the nonlinear term in (1.2) can be assumed negligible, and ϕ is locally harmonic in the scaled variables. Let

$$z = x^* + iy \quad , \quad x^* = x - L$$

$$\theta \equiv \arg z \quad , \quad r \equiv \mod z$$

$$w(z) = u(x^*,y) - iv(x^*,y) = \text{complex velocity}$$

where

$$u = \phi_{x^*} \quad , \quad v = \phi_y \quad .$$

If the boundary conditions are locally linearized near the point z = 0, then

$$v(x^*,0) \to F(L) \equiv \omega \quad , \quad x^* \to 0 \tag{4a}$$

$$u(x^*,0) = 0 \quad , \quad x^* > 0 \quad . \tag{4b}$$

To dominant order, a sufficient condition to satisfy (3) and (4) near the origin is that w has the following branch point behavior

$$w = i(\omega + B\sqrt{z}) \quad \text{as} \quad z \to 0 \quad , \quad (0 \leq \theta \leq \pi) \tag{5}$$

where B is a real constant to be determined by matching with the outer nonlinear solutions. Equation (5) implies that

$$\phi - \phi_L \triangleq -\omega y - \frac{2}{3} B r^{3/2} \sin 3\theta/2 \ . \tag{6}$$

Several examples to be discussed indicate that the approach described previously, in which ϕ is maintained continuous at the wall trailing edge, gives numerical solutions that satisfy the Kutta condition (3). However, a rigorous proof that this is an implication of the algorithm has not been attempted. A similar procedure has been used by Krupp[17] to satisfy the Kutta condition in the solution of the transonic small disturbance lifting airfoil problem.

2.4 Results and Discussion

In addition to the assumptions given in the Introduction, the analysis previously described is not directly applicable to choked flows where upstream and downstream conditions are decoupled. Sonic zones comprising the entire vertical dimension of the flow field are thereby excluded. However, the foregoing methods can be extended to handle such cases.

A number of examples will now be considered. For these cases, the associated wall displacement functions and exit velocity distributions H(Y) are given in Table 1. For most of these cases, K is unity and D will take on this value for the remainder of this paper.

Wall pressure distributions for the convex ramp comprising Case 1 are shown in Fig. 3 for K = 1 and K = 1.46. By interpreting these results as distributions for different final M_∞'s downstream but with the same δ, the decrease in M_∞ leads to upstream motion of the terminating shock but a preservation of the shock strength.

Table 1. Wall Jet Cases

Case	f = Wall Shape Function	H(Y)	Remarks
1	$f = f_1 = 0$, $0 < x < 1$ $= -(1-x)^2$, $1 < x < 2$ $= 3-2x$, $2 < x < L$	.075 $0 < Y < 1$	L = 3.8 for this and all other cases
2	$f = f_2 = -f_1$		
3	$f = f_3 = 0$, $0 < x < 1$ $= [x^2-1+2(L+1)(1-x)]/2L$, $1 < x < L$		Has discontinuous slope at x = 1
4	$f = f_4 = 0$, $0 < x < 1$ $= \frac{10(L-1)}{L\pi} \cos \frac{\pi(x-1)}{L-1} - 1$, $1 < x < L$		Has reflex curvature on curved ramp portion
5	$f = f_5 = -x^2$, $0 < x < 1$ $= 1-2x$, $1 < x < 2$ $= -3$, $2 < x < L$	H = 1 $0 < Y < 1/2$ = 0 , $1/2 < Y < 1$	$\phi = 0.2$ on $0 < Y < 1/2$

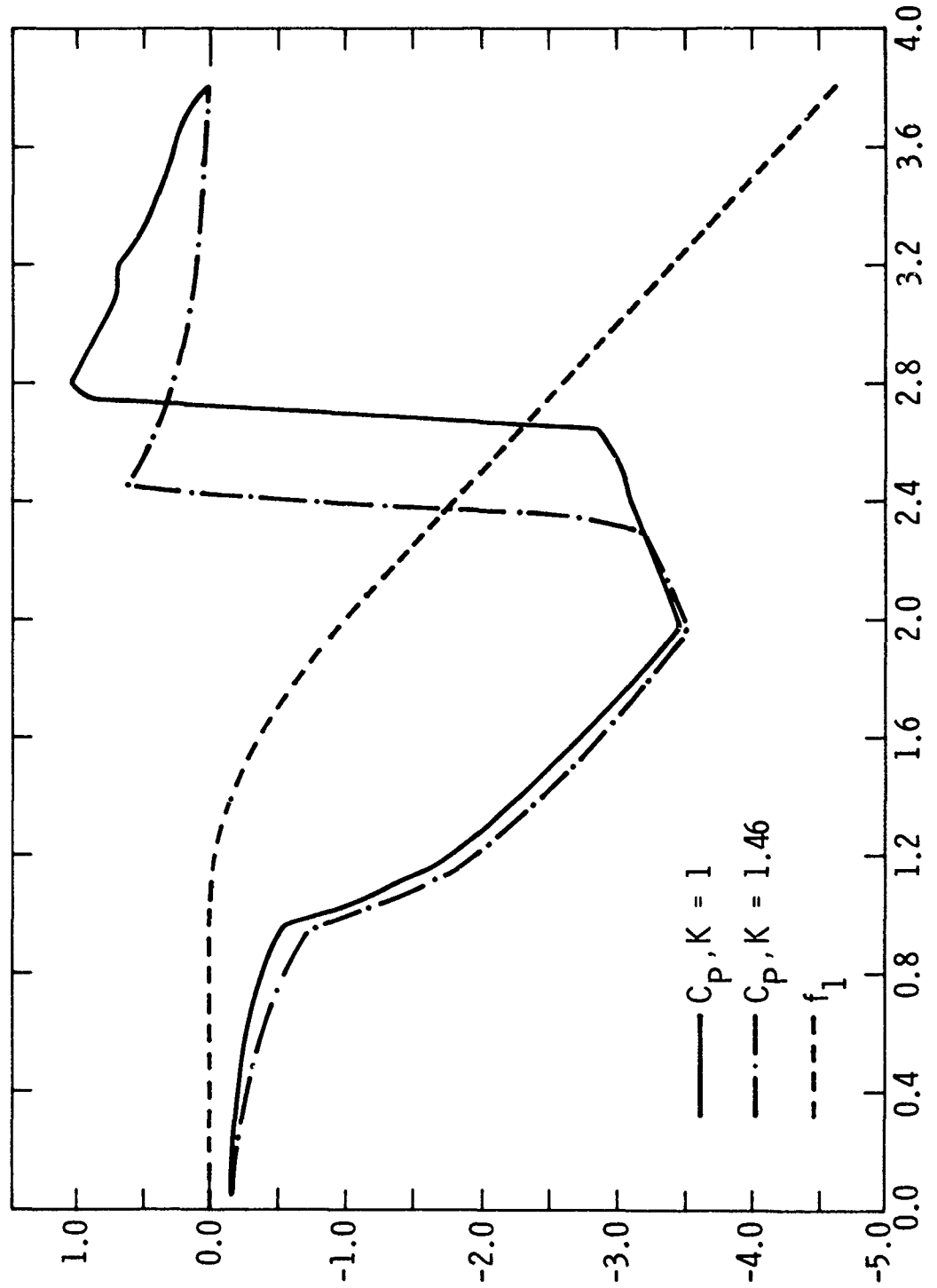

Fig. 3 Pressures along wall for K = 1 and K = 1.46. f_1 = normalized wall ordinate.

There is a smooth acceleration to critical conditions with the location of the sonic line established at the curvature discontinuity, $x = 1$. These calculations, which are typical of the other cases, cost approximately \$60 on the Berkeley 7600 and ran 15-30 CP seconds. Figure 4 shows a close-up of the pressures near the trailing edge. The dashed line has a slope proportional to $\sqrt{x^*}$, appropriate to the singular behavior given by Eqs. (5) and (6) and the Kutta condition (3). Isobars shown in Fig. 5 are consistent with these remarks and demonstrate the satisfaction of homogeneous pressure boundary conditions on the slip lines. Because of the weakness of the singularity, e.g., $\phi_{xx} \sim r^{-1/2}$ as $r \to 0$, special numerical treatments such as those of Woods[18] were not used.

In Figs. 6 and 7, rapid decay of the disturbances is indicated. The relaxation length for this decay from (1.8b) with $D = K = 1$, is π. This exponential decay is typical of flows confined by jet boundaries and is much more potent than for bodies in unbounded fields. Qualitatively similar effects have been discussed by Murman,[19] and Pinzola and Lo[20] in connection with tunnel wall interference on transonic airfoils. The distinction between confined and unconfined flows can be appreciated by an interpretation of the exponential series due to (1.5) arising in the far field developments dominated by (1.8). Because of linearity of the far field, this series is directly related to expansions occurring in analogous incompressible flow problems, in which a singularity is reflected between free pressure boundaries. This yields an image development in which the strengths alternate in sign to satisfy the slip line condition.* Thus, the relaxation to uniform conditions downstream, which must be consistent with homogeneous conditions on the slip lines, produces a more rapid decay than found in unconfined flows.

*Such a series can be summed by recognizing that it is a partial fraction expansion of a hyperbolic function which is exponentially small as $x \to \infty$, consistent with developments such as (1.8a).

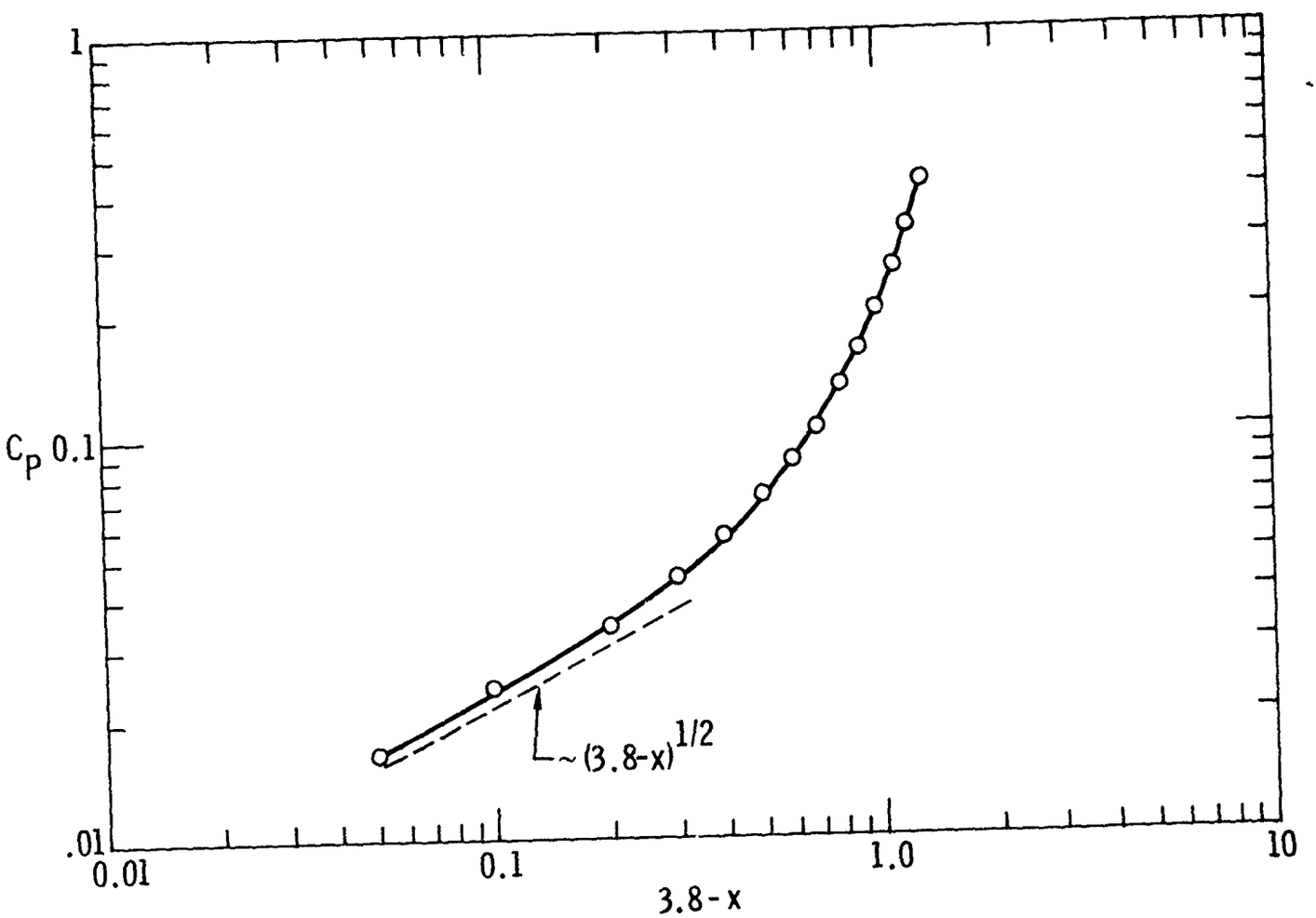

Fig. 4 Local solution near trailing edge, Case 1.

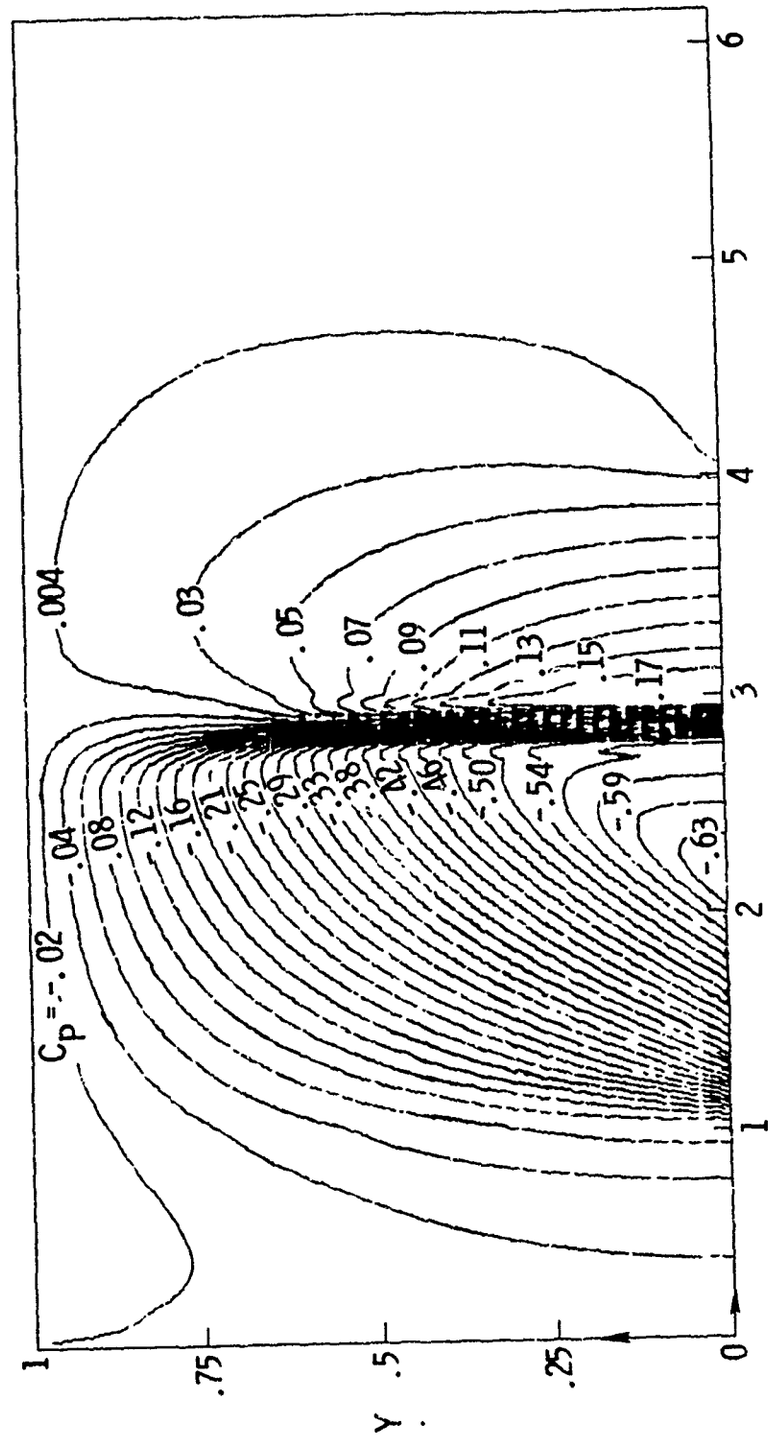

Fig. 5 Isobars for Case 1.

SC5055.21FR

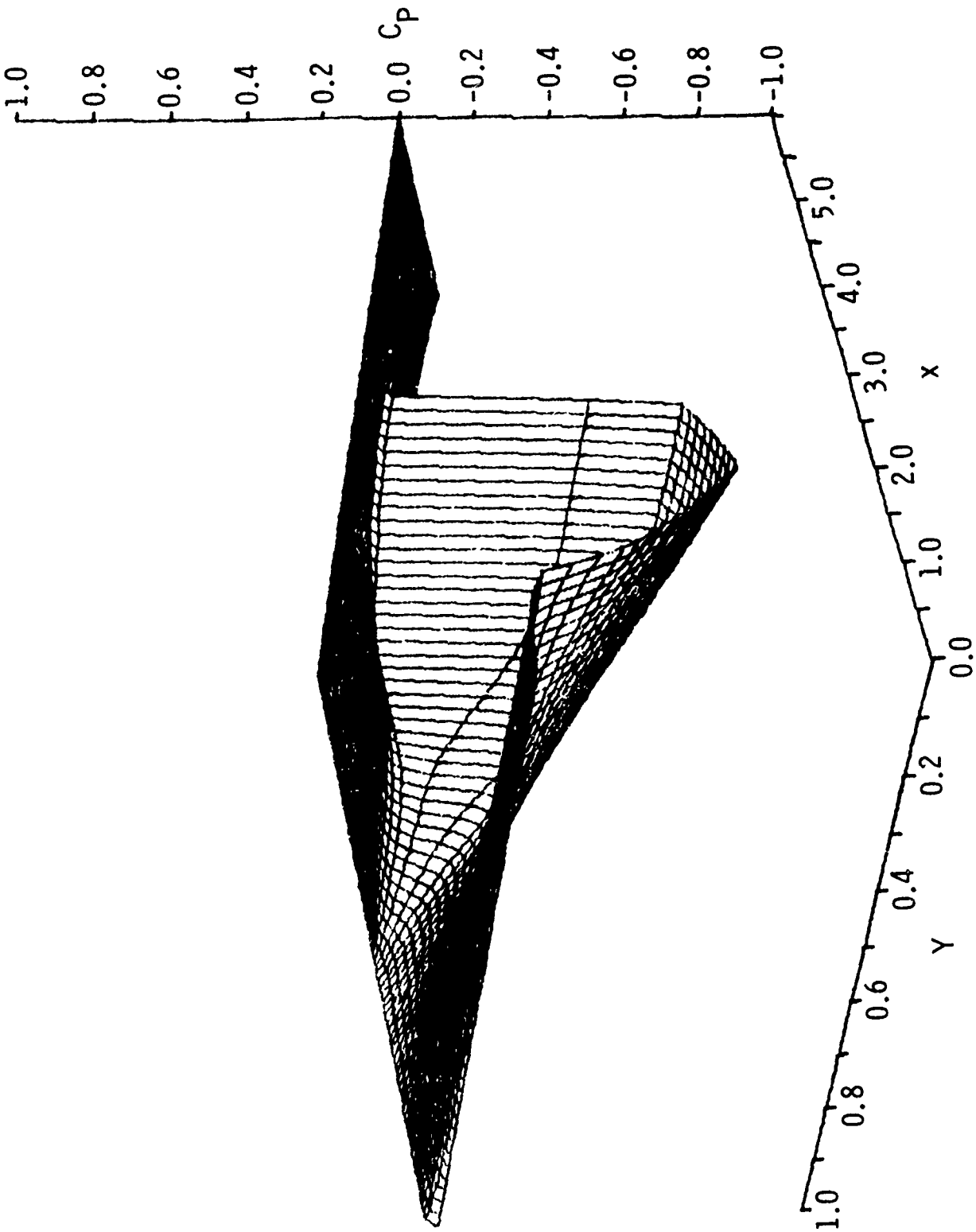

Fig. 6 C_p surface for Case 1.

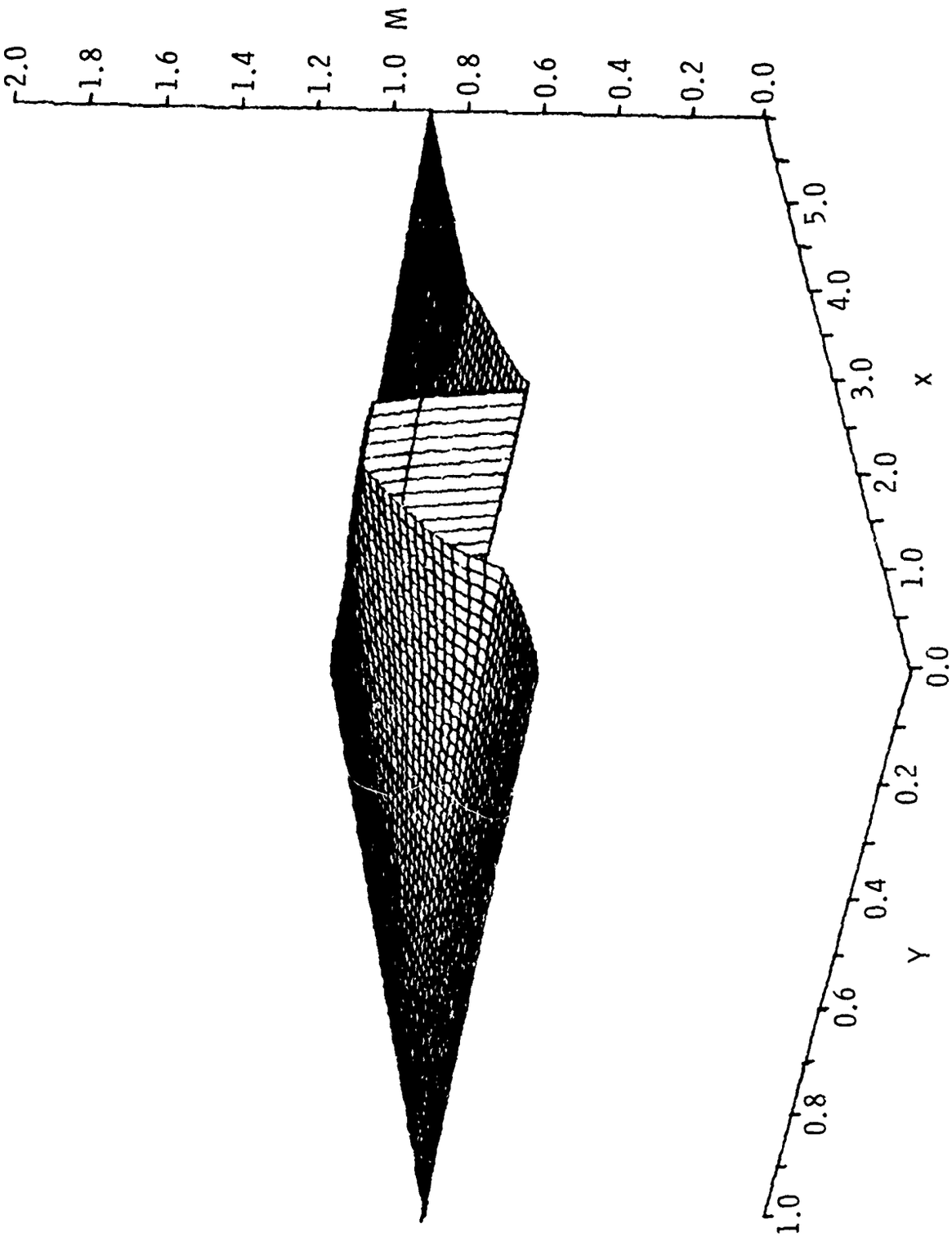

Fig. 7 Mach surface for Case 1.

In Figs. 8a and 8b, the upper and lower slip lines obtained from integration of (1.3b) and (1.3d) are given for Case 1. It is evident from Fig. 8a that the curved surface in this approximation turns the flow so that the streams are parallel for $x \to \infty$. It is evident from Fig. 8b that in the near field, this is not quite the case. Asymptotic parallelism can be established for subsonic conditions far downstream by integration of the small disturbance continuity equation. Thus

$$G_1'(x) - G_2'(x) = \frac{d}{dx} \int_0^1 \left(Ku(x,Y) - \frac{\gamma+1}{2} u^2\right) dY \tag{7}$$

and, since $u = \mathcal{O}(e^{-x^*})$, this expression shows that $G_1'(x) \to G_2'(x)$ as $x \to \infty$. Equation (7) can also be obtained by differentiating (1.8a) with respect to Y and using (1.3b) and (1.3d). For the case of a free jet with a symmetrical exit Mach number profile function H, i.e., $H(Y-1/2) = H(1/2-Y)$, $G_1 = -G_2$ and the divergence theorem or integration of (7) between $x = 0$ and ∞ gives the displacement of the jet infinitely downstream as

$$G_1(\infty) = \frac{1}{2} \int_0^1 \left(KH(Y) - \frac{\gamma+1}{2} H^2\right) dY \tag{8}$$

where $G_1(0) = 0$ has been used.

Insight into the mechanisms causing acceleration to supercriticality can be obtained from the flow direction field for Case 1 shown in Fig. 9. For clarity, all isocline slopes have been magnified by a factor of 100, and only the entrance section $0 < x < 1$ is depicted. The expansion around the curved ramp on the interval $1 < x < 2$ leads to upstream influence in the subsonic region which turns most of the flow downward upstream of $x = 1$, producing throats and acceleration due to the stream tube contraction required by the zero slope boundary condition in that region. Also indicated is the "ballooning" due to the singularity occurring at (0,1), the top point of the jet exit station. In contradistinction to the trailing edge where $u \to 0$, local linearization cannot be used to characterize the flow behavior in this region, and some local similarity solution must be sought, presumably of the form $\phi = x^{\alpha} f(y/x^{\beta})$ where α and β are exponents to be determined.

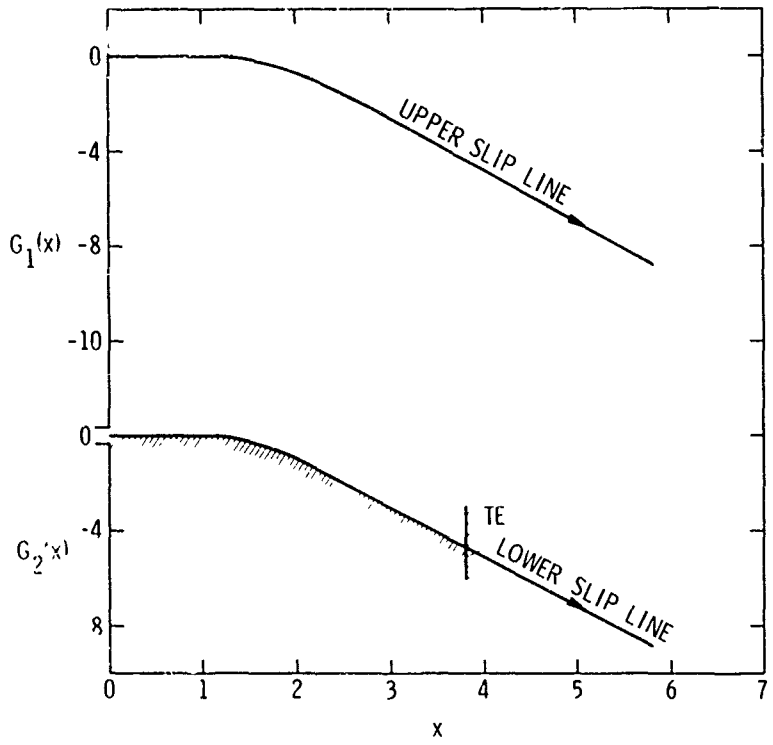

Fig. 8a Slip line shapes for Case 1.

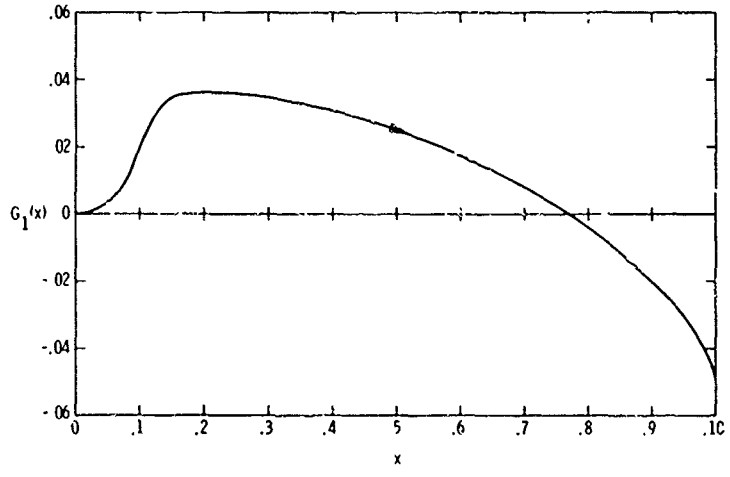

Fig. 8b. Close-up of slip lines near jet exit for Case 1.

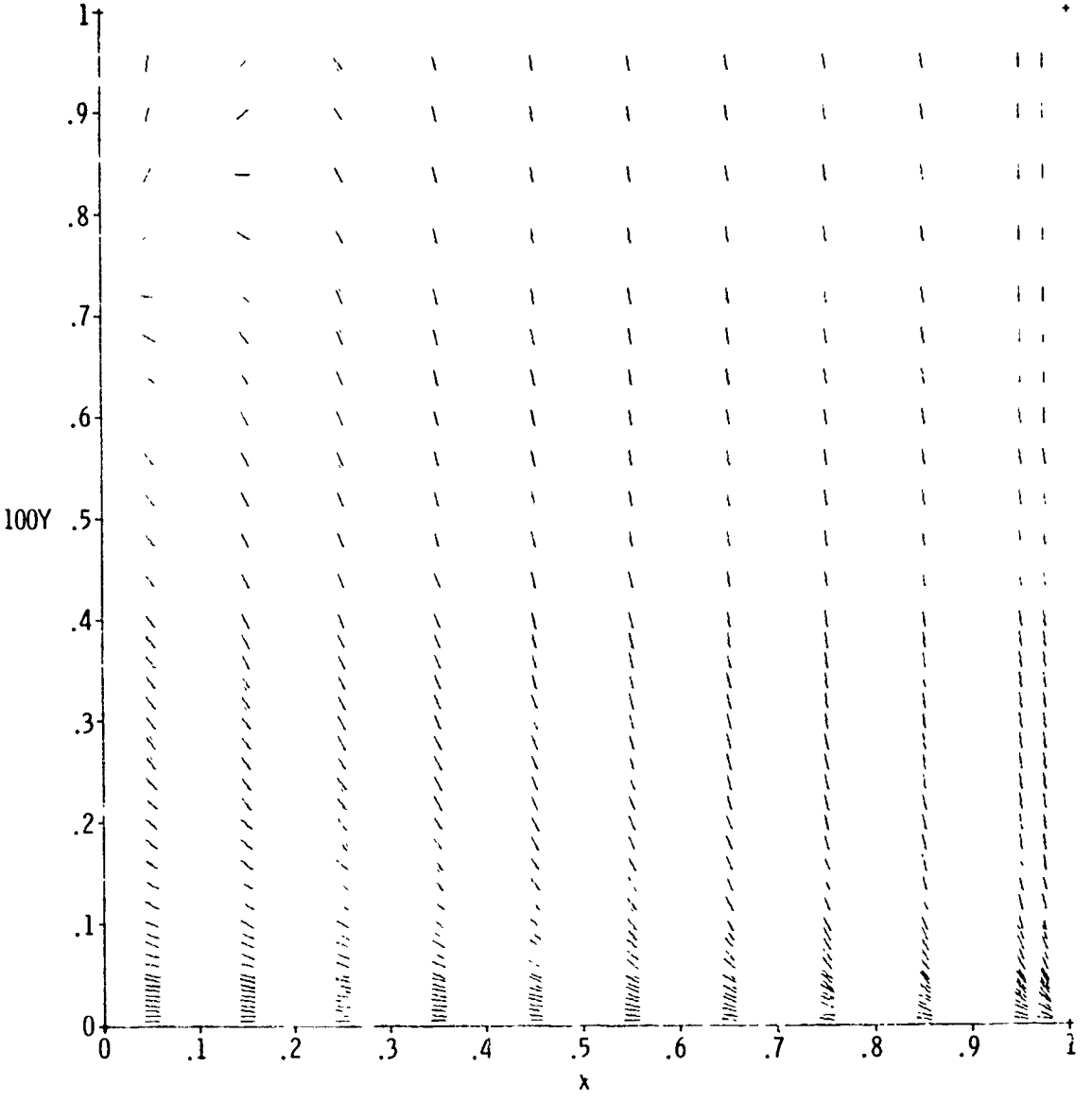

Fig. 9 Streamline direction field for Case 1, (closeup near jet exit).

By contrast, the concave shape shown in Fig. 10 produces the anticipated compressive deceleration, which is also depicted in Fig. 11.

The effect of a slope discontinuity is indicated in Fig. 12. It is evident that the numerical method accurately locates the initiation of the sonic line at the point (1,0) where the flow is "tripped" to criticality by the acceleration singularity at this location. In most other respects, the pressure distribution is similar to that for Case 1.

In Fig. 13, the effect of a reflex curvature in accelerating the recompression process is shown. As related to comparable turning and wall deflection treated in Case 1, the strength of the terminating shock is considerably increased, as is the magnitude of the pressures near the trailing edge.

The effect of mixed flow conditions at the exit is shown in Figs. 14-16. Here, the function H as well as $\phi(0,Y)$ comprise the Cauchy data needed to properly pose the hyperbolic portion of the initial manifold. Since the vertical velocity $\phi_Y(0,Y)$ can be derived as a tangential differentiation, the Cauchy data connotes specification of the additional velocity component for supersonic portions of the jet exit station. Figure 16 indicates that in addition to the usual terminating shock, the transition from hyperbolic to elliptic flow occurs across a weak shock emanating from the specified u discontinuity at (0,1/2).

In Fig. 17, the behavior of centerline pressures for various free jet cases is shown. The monotone subcritical behavior exhibited by these nonlinear cases has not yet been corroborated by rigorous proof based on the boundary value problem with subsonic exit and downstream conditions. For linearized subsonic flow, this property is obvious from the maximum modulus theorem. It should be noted that in the free jet problem discussed here, specified mass flow, pressure ratio, and final Mach number M_∞ uniquely determine δ, the scale parameter for the jet displacement.

For a validation, a comparison of numerical and Prandtl-Glauert free jet solutions for $u(x,1/2)$ for $H = 0.35$ and $K = 10$ is shown in Fig. 18, where the analytical solution obtained either from summed eigenfunction expansions or transforms is:

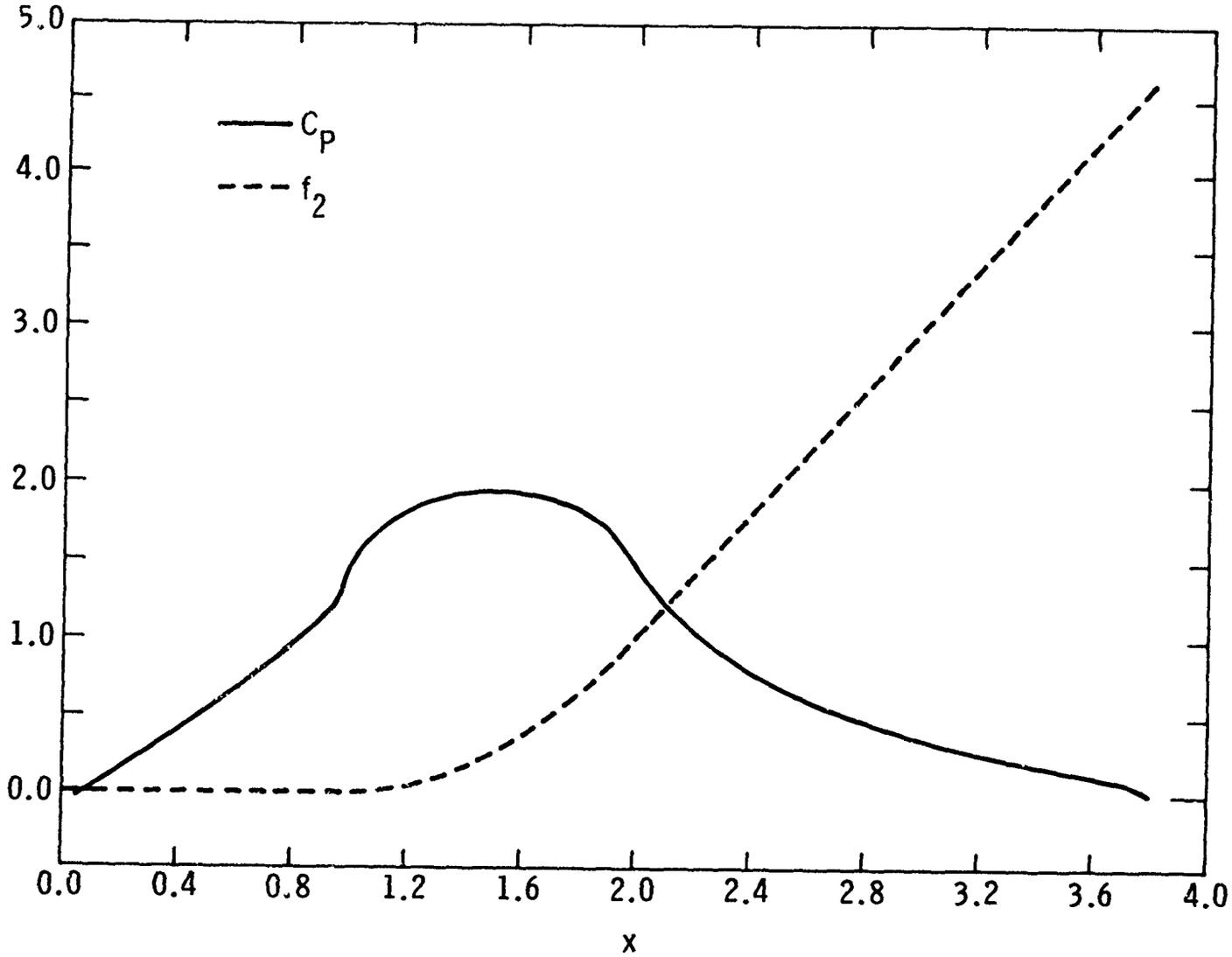

SC5055.21FR

Fig. 10 Pressures along wall for Case 2, f_2 = normalized wall ordinate.

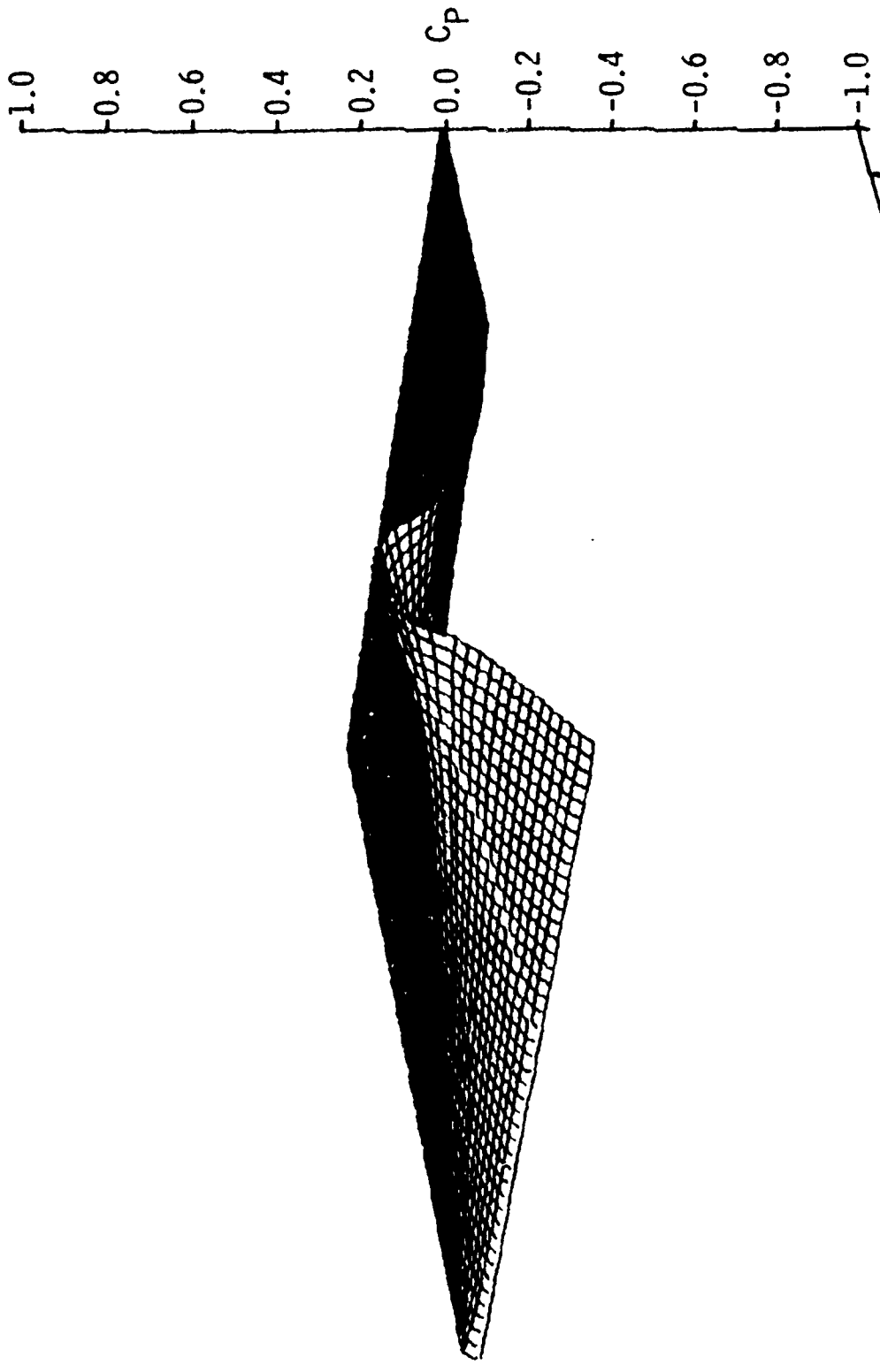

Fig. 11 Pressure surface for Case 2.

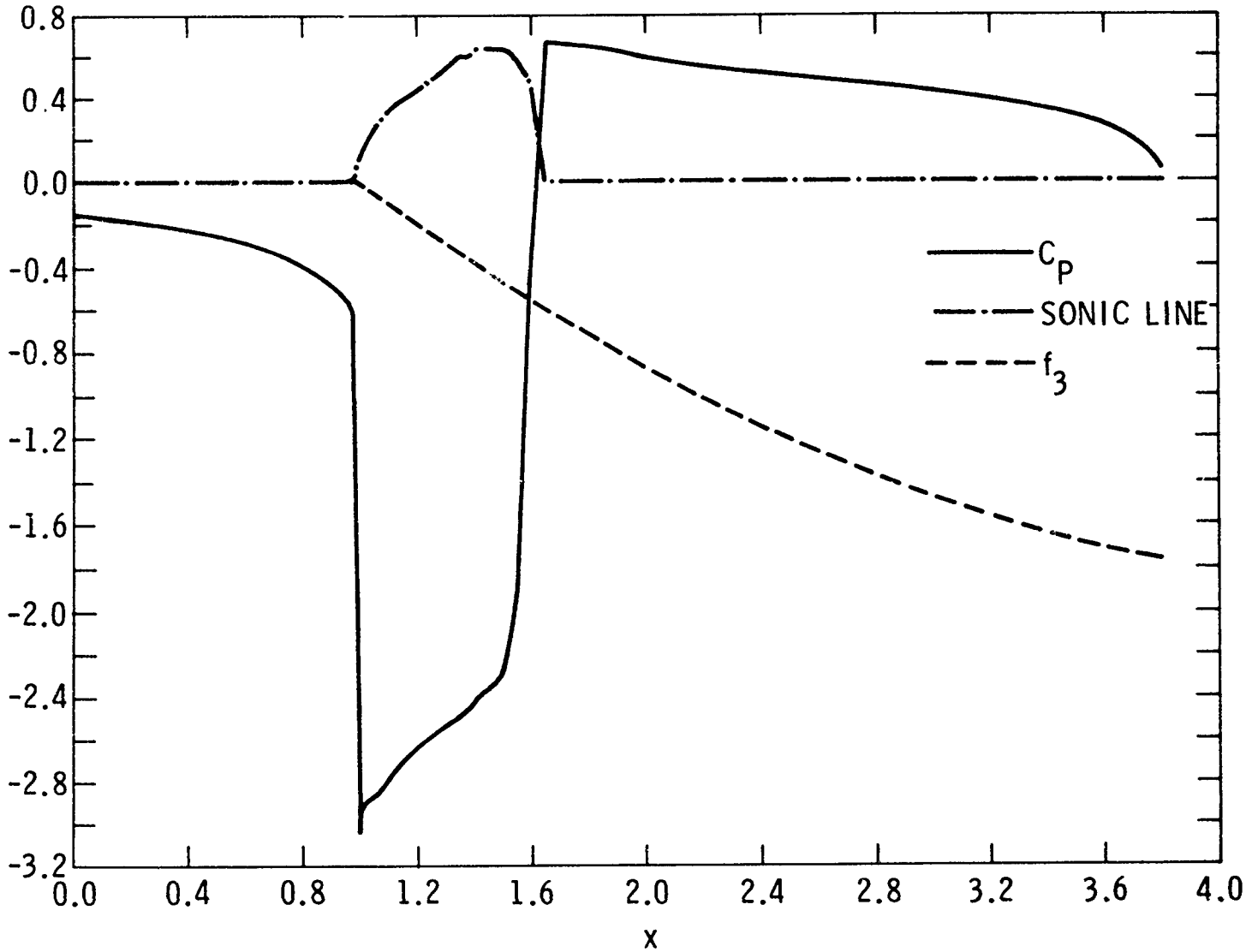

Fig. 12 Pressures along wall for Case 3, f_2 = normalized wall ordinate.

SC5055.21FR

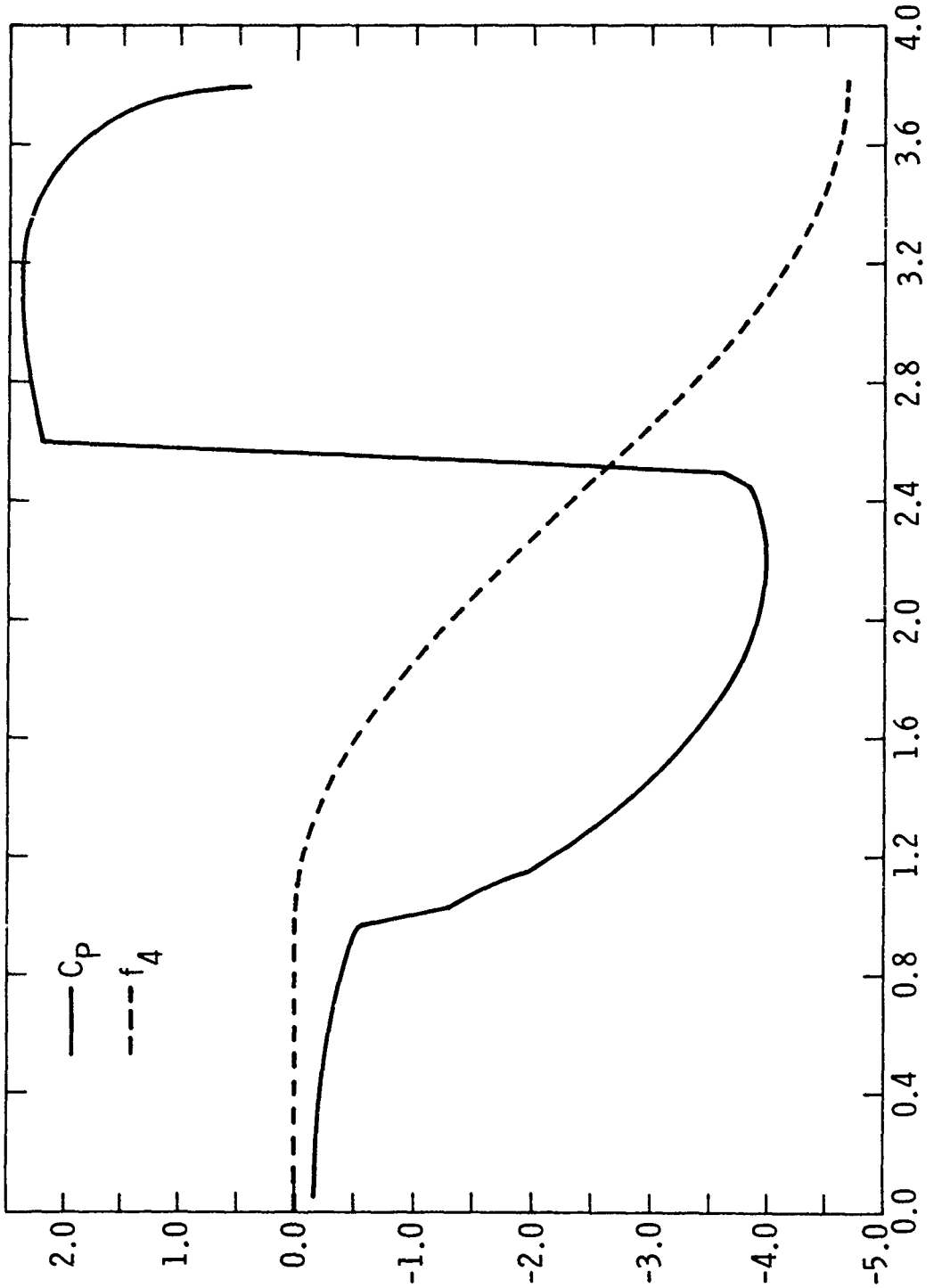

Fig. 13 Pressures along wall for Case 4, f_4 = normalized wall ordinate.

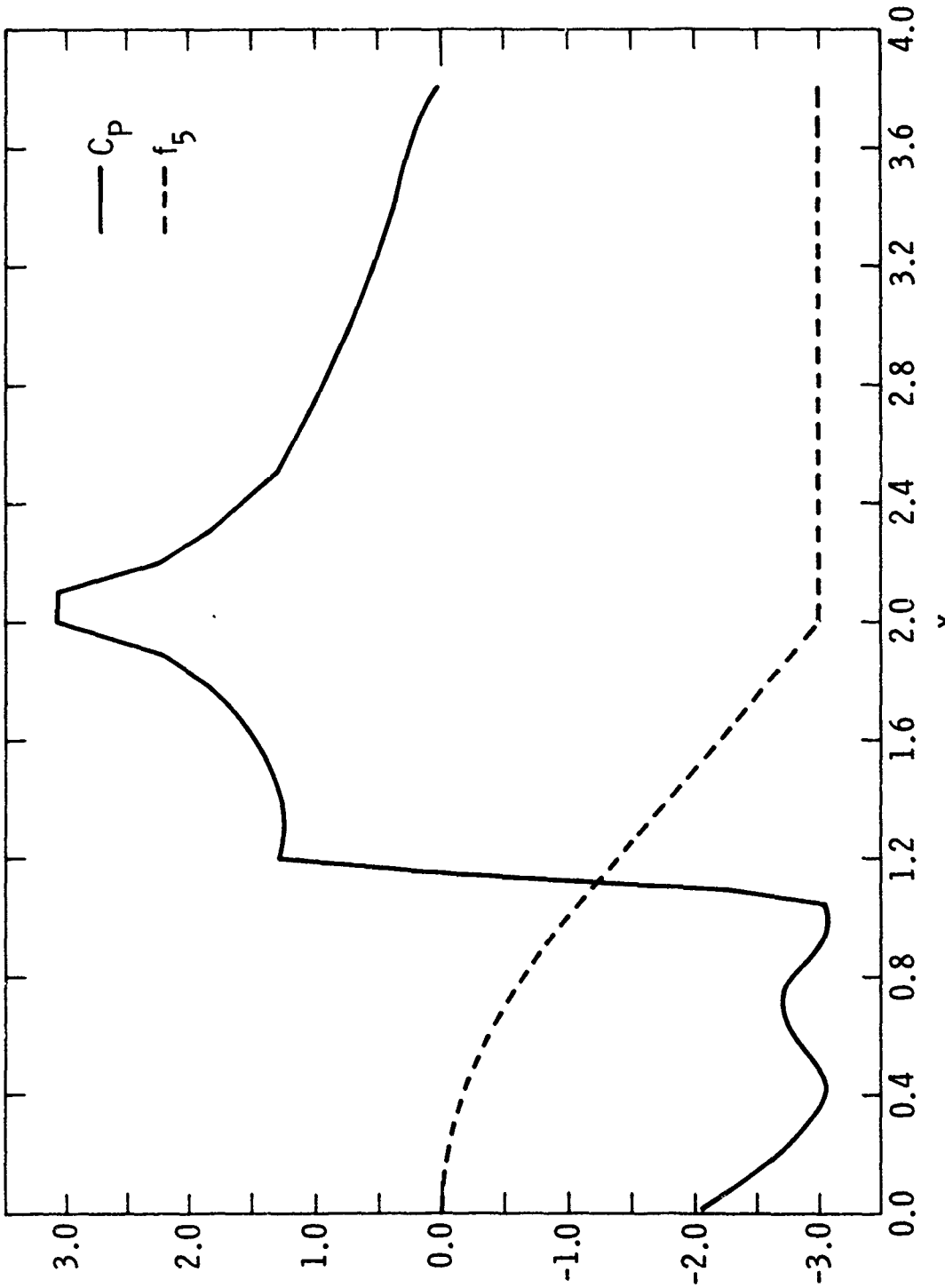

Fig. 14 Pressures along wall for Case 5 (partially supersonic jet exit), f_5 = normalized wall ordinate.

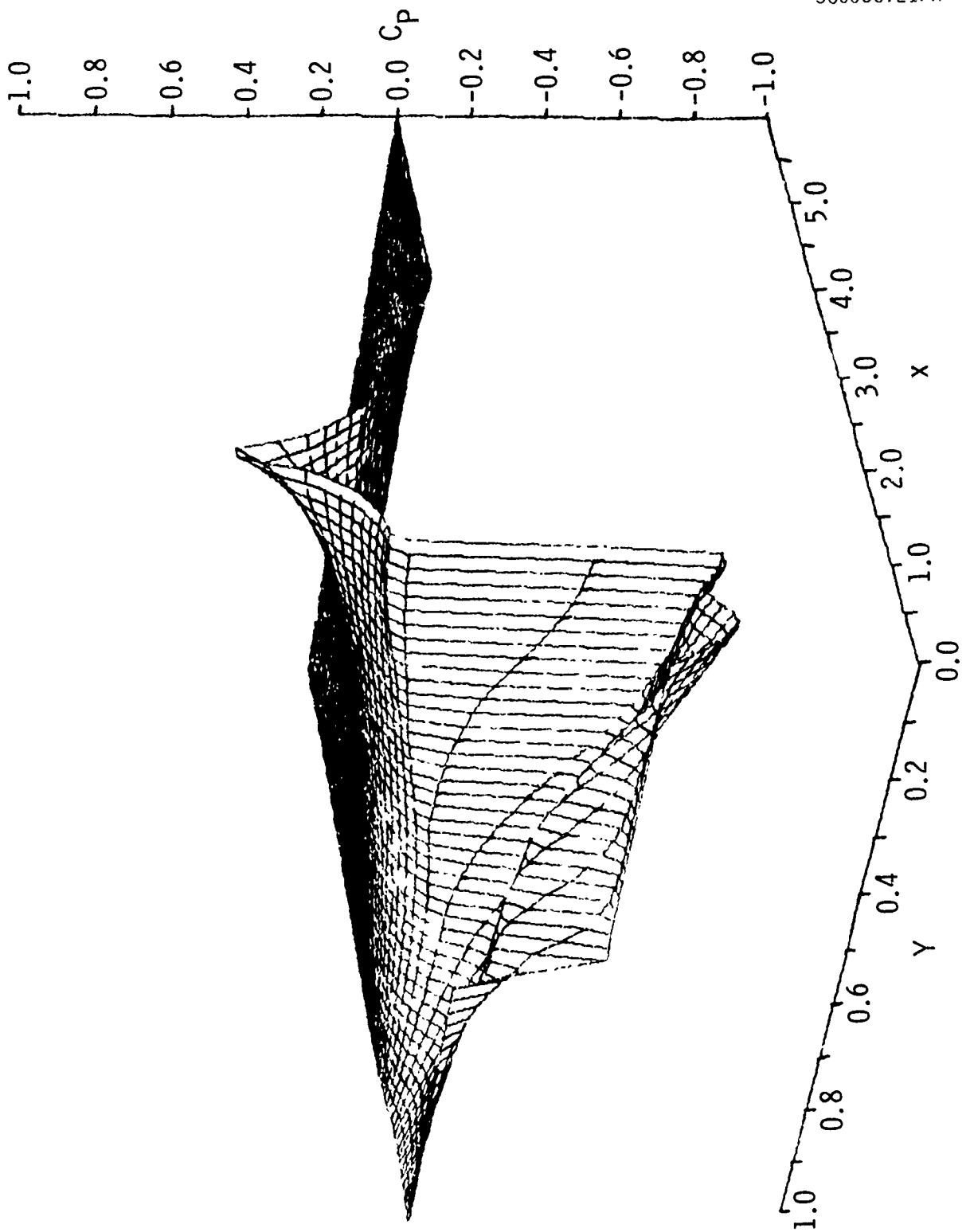

Fig. 15 Pressure surface for Case 5.

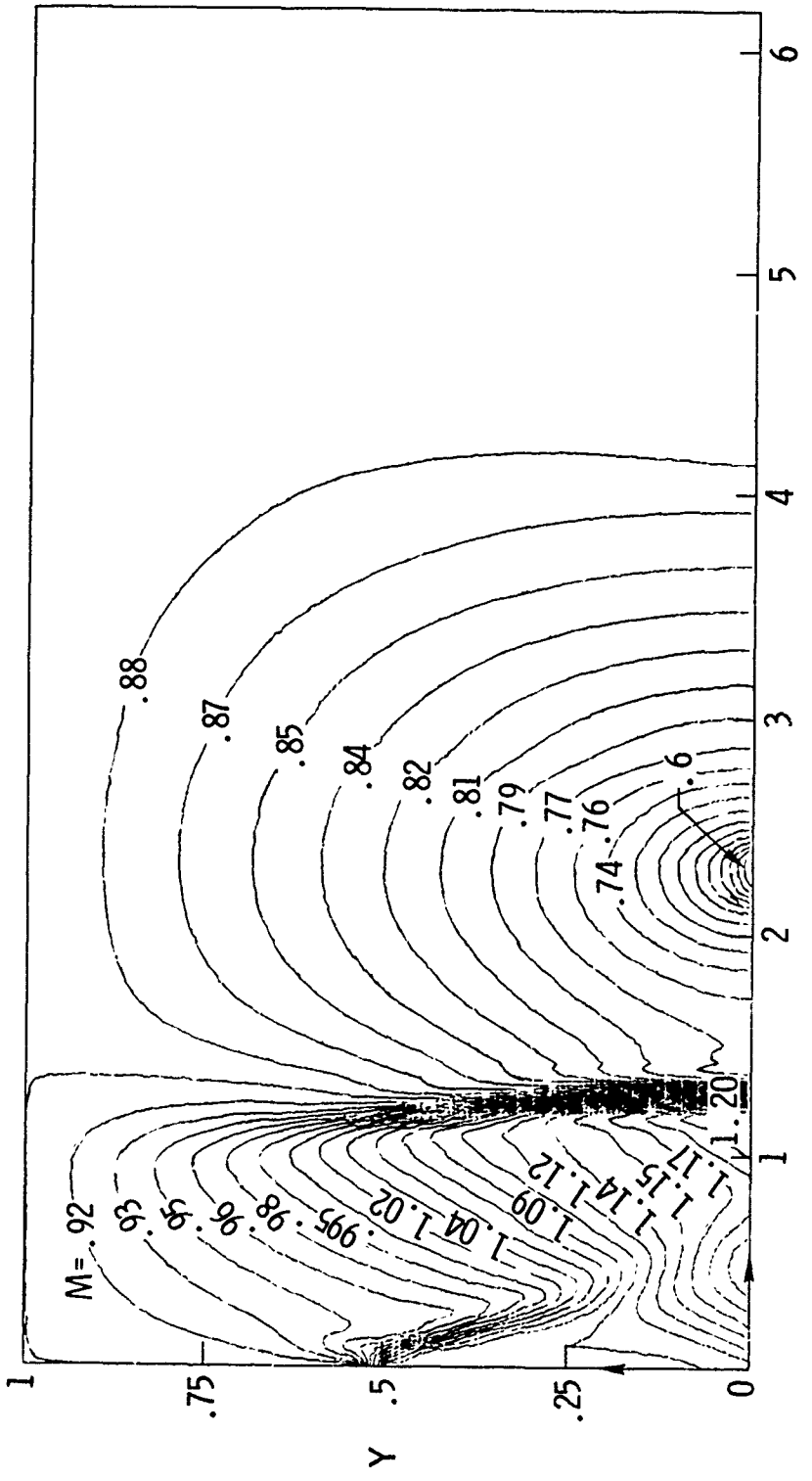

Fig. 16 Mach contours for Case 5.

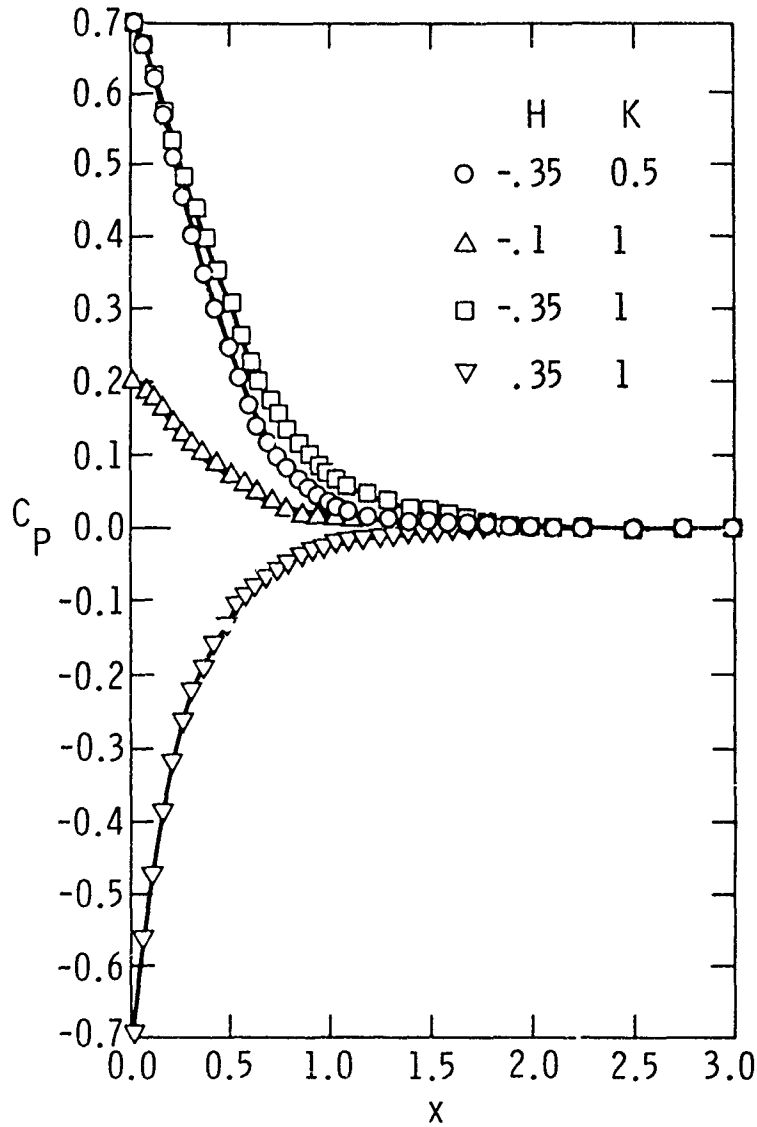

Fig. 17 Centerline pressures for a transonic free jet for various pressure ratios and similarity parameters, K.

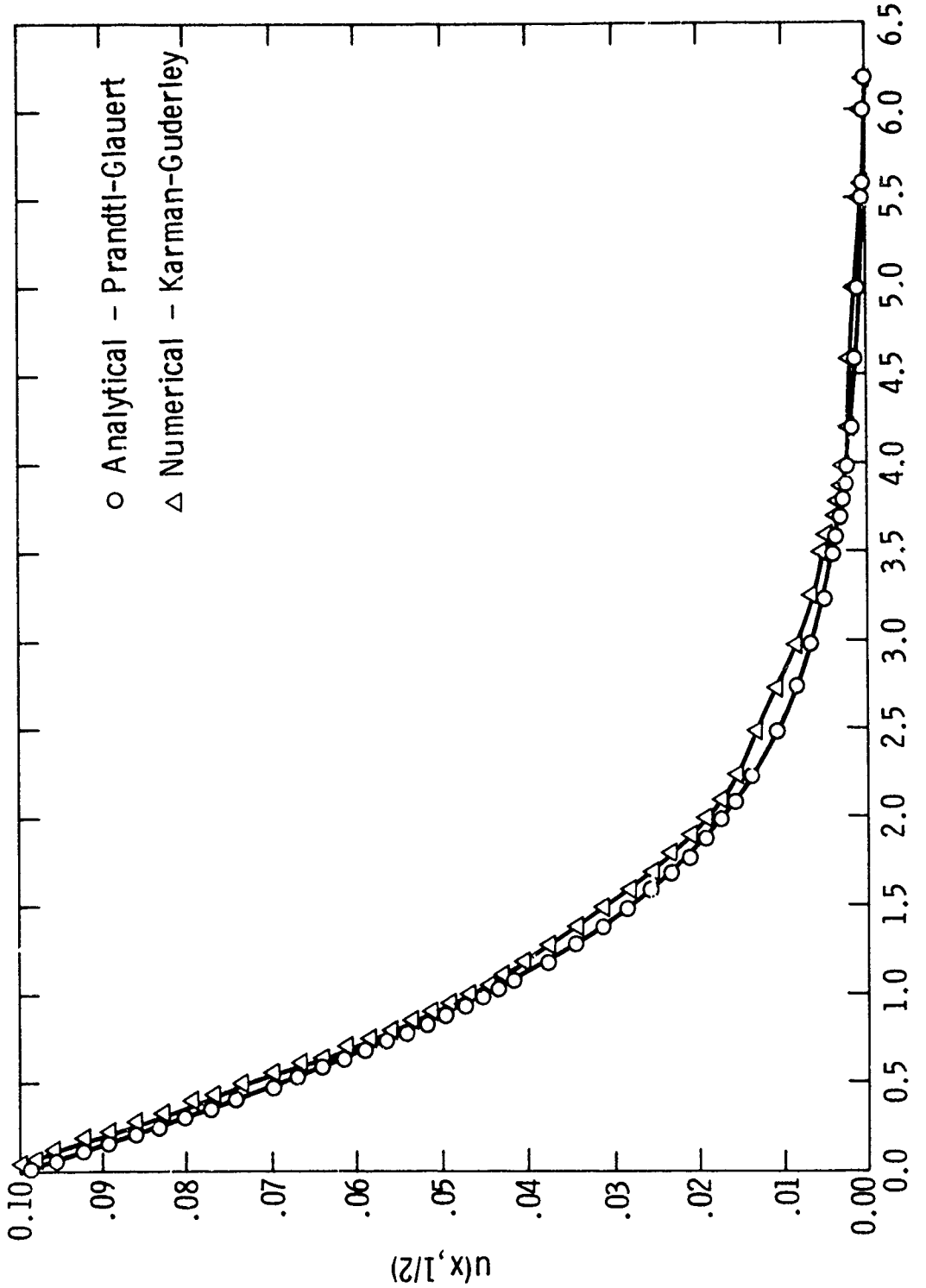

Fig. 18 Comparison of free jet analytical and numerical solutions.

$$u = \frac{2H}{\pi} \tan^{-1} \frac{\sin y^\dagger}{\sinh x^\dagger} \tag{9a}$$

$$v = -\frac{H\sqrt{K}}{\pi} \ell n \frac{\cosh x^\dagger + \cos y^\dagger}{\cosh x^\dagger - \cos y^\dagger} \tag{9b}$$

and

$$x^\dagger \equiv \pi x/\sqrt{K} \quad , \quad y^\dagger \equiv \pi Y \quad .$$

The slight discrepancies shown in Fig. 18 presumably derive from the small nonlinear effect associated with the finite K value and from truncation errors of the discretizations which are only approximately second order for a non-uniform elliptic mesh. The associated universal slip line curve is obtained from the following integral of (9b)

$$\frac{G_1(x)}{HK} = \frac{1}{2} - \frac{4}{\pi^2} \sum_0^\infty \frac{[1 + x(2n+1)]e^{-(2n+1)x}}{(2n+1)^2} - \frac{x}{2} \operatorname{ctnh}^{-1}(\cosh x) \tag{10}$$

where the daggers have been dropped. Equation (10) has the following limiting behavior

$$\frac{G_1(x)}{HK} = \frac{2}{\pi^2} \left\{ -x\ell nx + \left(\frac{1}{2} \ell n 4 + 1 \right) x + \mathcal{O}(x^2) \right\} \quad \text{as } x \to 0$$

$$\frac{G_1(x)}{HK} = \frac{1}{2} - \frac{4}{\pi^2} e^{-x} + \mathcal{O}(xe^{-2x}) \quad \text{as } x \to \infty$$

and is plotted in Fig. 19. The asymptotic half width thus checks that given by (8) when the nonlinear second term in the integral is omitted.

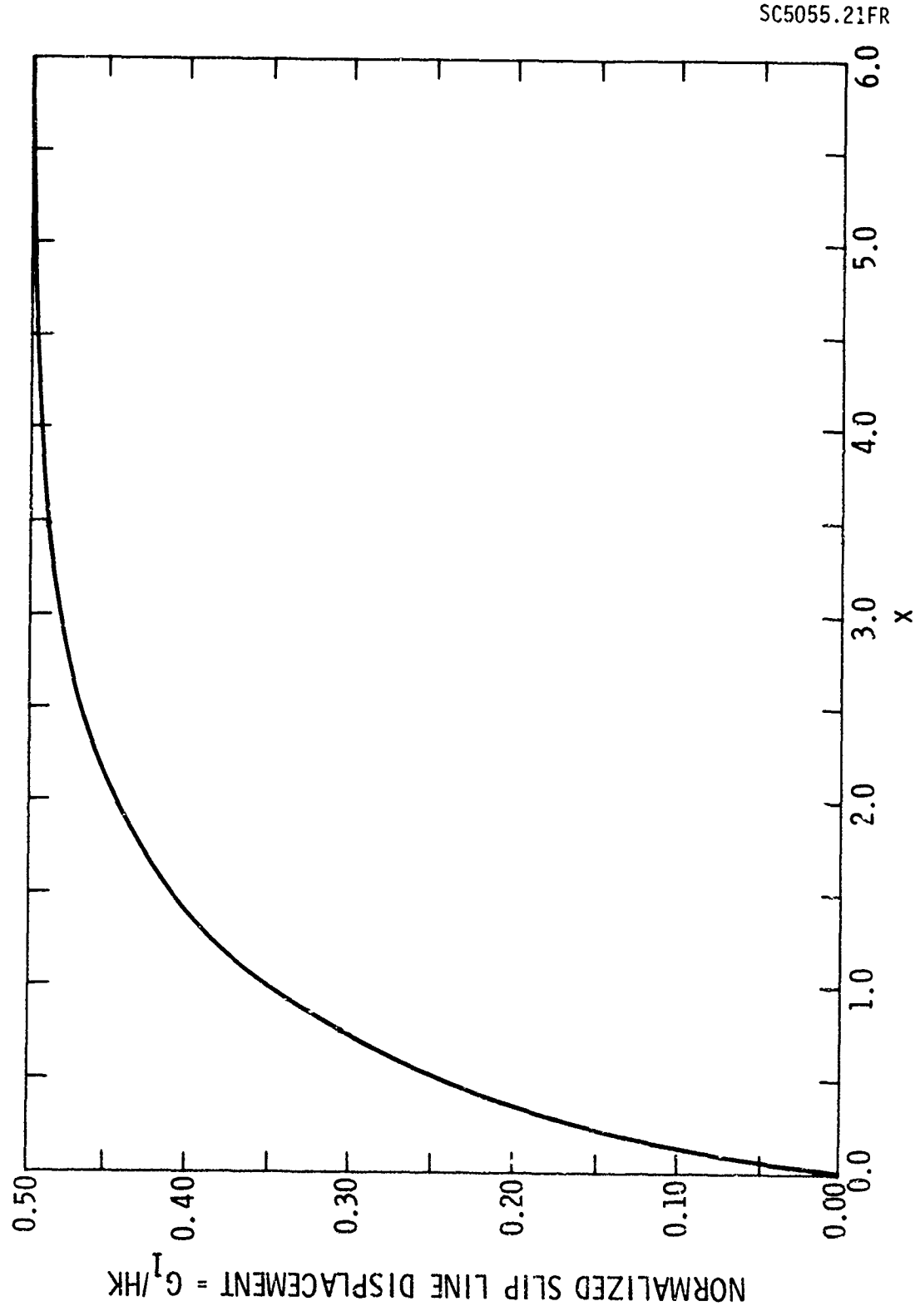

Fig. 19 Free jet boundary for Prandtl-Glauert flow.

3.0 INVISCID MODEL FOR UPPER SURFACE BLOWING

In the previous section, a submerged jet problem related to tangential blowing was studied. Actually, the jet structure investigated in this connection can be realized only approximately for large values of the jet momentum flux. For more moderate values, it is necessary to account for interaction with the external stream. This implies that a coflowing rather than submerged jet must be considered adjacent to the wall and that the associated perturbations of flow external to the jet be treated.

In Fig. 20a, a schematic of an upper surface blown airfoil is shown embedded in a transonic flow, with a supersonic wall jet tangentially injected along its upper surface. The inviscid problem for this configuration is formulated in Fig. 20b, based on a heuristic generalization of the jet flap model of Ref. 21. Conditions across the jet and jet-wake are not indicated. Relevant to this formulation, we will discuss certain aspects of the coflowing jet flow which are pertinent to establishing the appropriate boundary conditions for the external flow. We will also treat other properties that have significance for non-aeronautical applications in addition to the present one.

Considering the coflowing wall jet, we divide its consideration into regions such as R_e, R_{TE}, and domains outside of these neighborhoods on and off the airfoil. The latter domains are inviscid boundary layers with a structure consistent with a balance solely between pressure and centrifugal forces. A systematic asymptotic theory for the fine structure of these layers is given in Section 3.2.1. In other sections and Refs. 5-7, properties of R_e and R_{TE} are discussed. For these regions, the effects of streamwise acceleration and wave interaction phenomena controlled by a length scale of the order of the jet thickness significantly alter this balance. To shed light on the transition of these axial boundary layers to the other zones, Section 3.1 treats an "inner" problem associated with the coflowing wall jet relevant to the matching of the regions R_e and R_{TE} to the jet, wake, and external flow. Section 3.1.1 also discusses selection rules to define the nature of the mixed flow structures that can arise in the wall jet. Numerical studies illustrating these structures

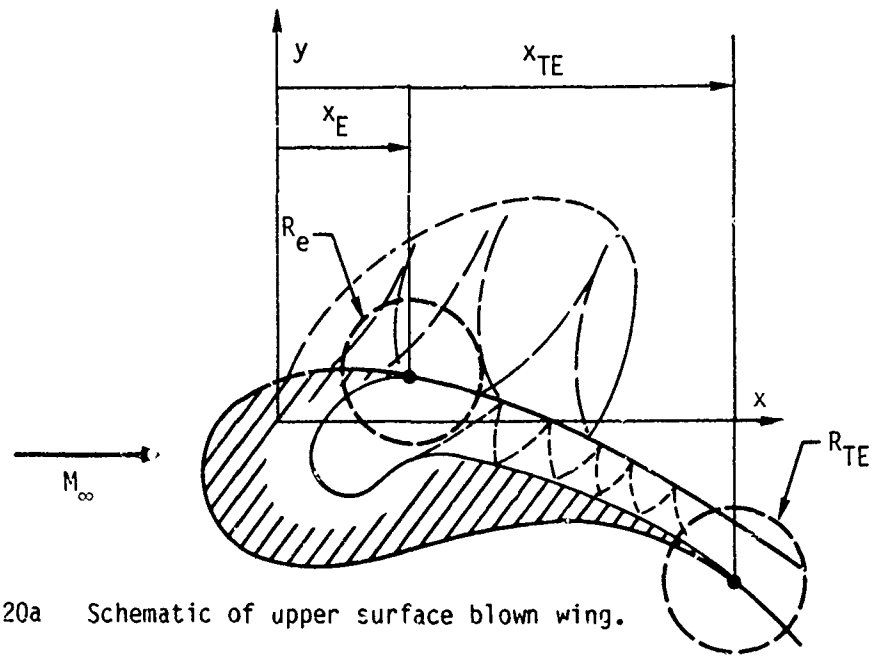

Fig. 20a Schematic of upper surface blown wing.

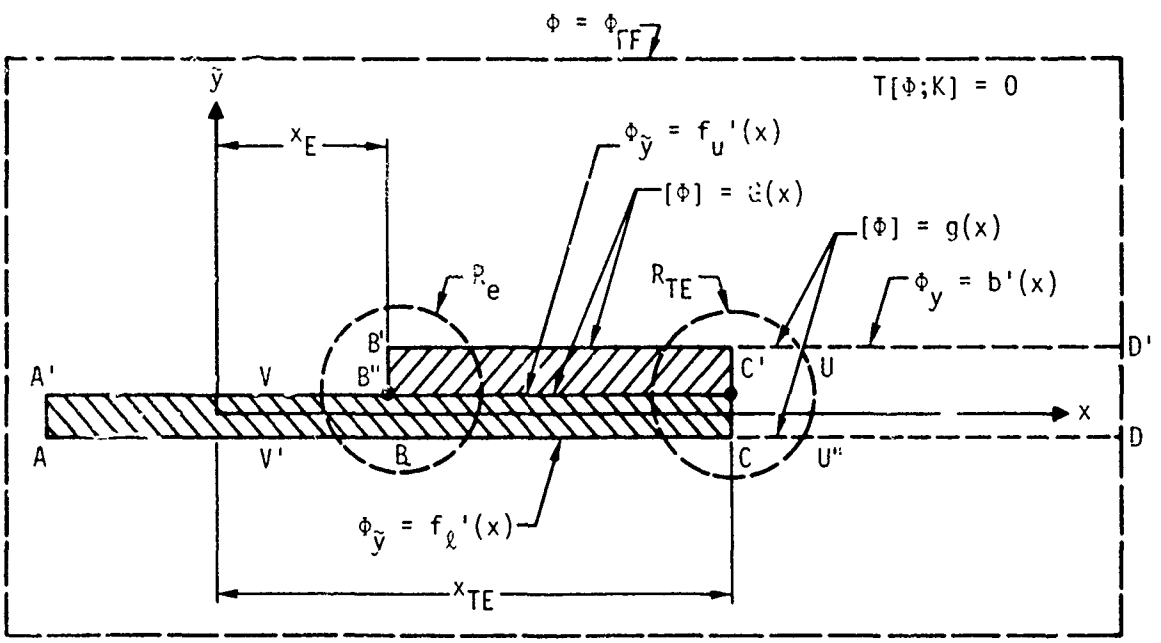

Fig. 20b USB global small disturbance formulation, $T[\phi;K] = [K - (\gamma+1)\Phi_x]\Phi_{xx} + \Phi_{\tilde{y}\tilde{y}}$.

which produce significant spikes observed in blown transonic airfoil pressure distributions are provided subsequently in Section 3.1.3. In Section 3.2.2, other aspects are discussed relevant to R_{TE} and the formulation for the global description for the blown airfoil problem. Results are given for typical cases in later portions of this report.

3.1 Coflowing Transonic Wall Jets - An "Inner" Problem

In Fig. 21a, the appropriate formulation of a problem in which the regions R_e and R_{TE} are merged in the tangentially blown jet region of Fig. 20a is shown. As indicated previously, we are concerned with the transition of these regions in which streamwise gradients are important to other regions which are dominated by gradients normal to the jet. For the former, we note that for supersonic and transonic portions near the jet exit, the characteristic longitudinal scale is of the order of the wavelength of the reflected wave pattern from the slip lines. To treat the longitudinal scales properly, a KG limit, which in the notation of Fig. 20 has $(x_{TE} - x_e)/\delta^{4/3}$, $x/\delta^{4/3}$, $[y - \delta b_\ell(x)]/\delta$, $K_e = (1 - \bar{M}_e^2)/\delta^{2/3}$, $K = (1 - M_\infty^2)/\delta^{2/3}$ fixed as $\delta \to 0$, is utilized. Here, $\bar{M}_e^2$ is the average of the square of the exit Mach number distribution, and M_∞ is the freestream value of the Mach number. In this formulation, a new excess pressure ratio parameter arises naturally, which is given by

$$\omega = \frac{\frac{P_e}{P_\infty} - 1}{\delta^{2/3}} \quad \text{, fixed in the KG limit}$$

where P_∞ is the freestream ambient static pressure and P_e is the corresponding static value at the jet exit. Essentially, the approximation of slightly different velocities between the jet and external flow is used to study important flow features. In practical applications at transonic speeds, this could be realized with nearly choked blowing nozzles.

The formulation shown in Fig. 21a can be derived in the usual way by substituting the appropriate asymptotic expansions for the velocity potential

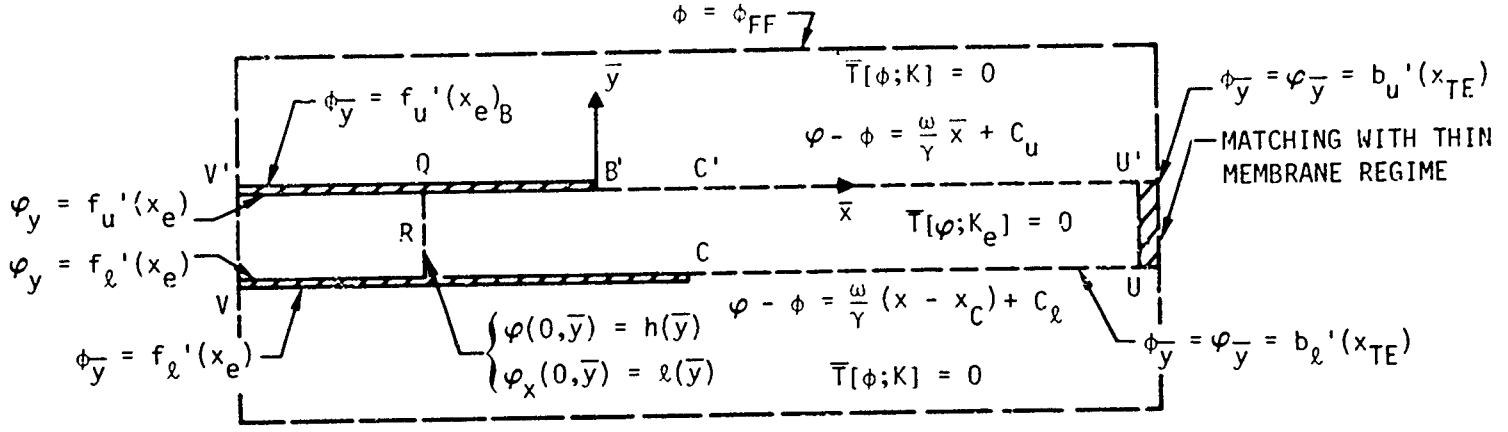

Fig. 21a Jet exit trailing edge region formulation.
$\bar{T}[\Phi;K] = [K - (\gamma+1)\phi_{\bar{x}}]\phi_{\tilde{x}\tilde{x}} + \phi_{\tilde{y}\tilde{y}}$, $(x_{TE} - x_e)/\delta^{4/3}$ fixed as $\delta \to 0$.

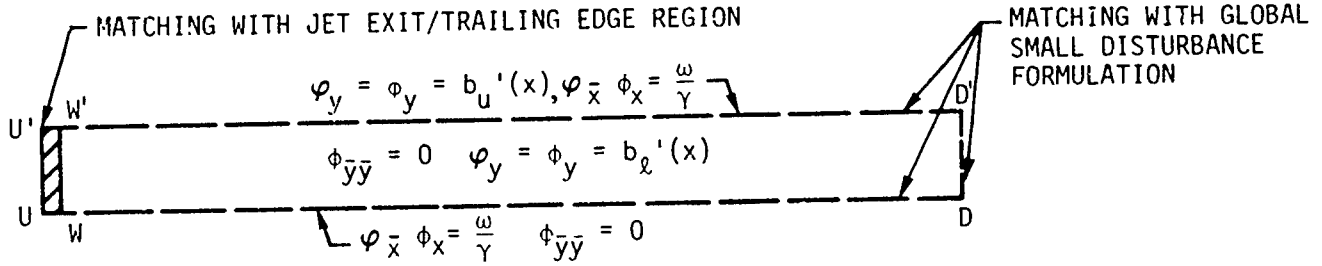

Fig. 21b Jet region - thin membrane theory.

into the full potential, and energy equations and the boundary conditions. On the boundaries of the cowl B'V' and CV, the latter involve tangency of the flow. On the slip lines C'U' and CU, they involve continuity of pressure and vertical velocity. At the jet exit, Dirichlet or Neumann conditions are specified if the exit is subsonic. If the exit is supersonic, Cauchy data are required. This model provides a means for studying the coupling of the external and internal flows and for understanding the role of this interaction on the development of the flow on the rear portion of the airfoil. Extension to axially symmetric cases also appears feasible. Intrinsic in the formulation is the representation of the internal and external flows by separate perturbation potentials ϕ and Φ, respectively. The appropriate asymptotic expansions for each are:

JET

$$\frac{\Phi_j}{U_e} = x + \delta^2\phi(\bar{x},\bar{y}) + \cdots \tag{1}$$

Φ_j = exact jet potential

$$\bar{x} = x/\delta^{4/3},\ \bar{y} = (y - \delta b_\ell(x))/\delta,\ K_e = (1 - M_e^2)/\delta^{2/3},\ \omega = \left(\frac{P_e}{P_\infty} - 1\right)/\delta^{2/3} \tag{2}$$

fixed as $\delta \to 0$

U_e = average velocity at jet exit

BLENDING LAYERS (IMMEDIATELY ABOVE AND BELOW JET)

$$\frac{\Phi_B}{U} = x + \delta^2\phi(\bar{x},\bar{y}) + \cdots \tag{3}$$

$\bar{x}$, $\bar{y}$, $K = (1 - M_\infty^2)/\delta^{2/3}$, ω fixed as $\delta \to 0$

U = freestream velocity in external flow

EXTERNAL FLOW

$$\frac{\Phi_{EXT}}{U} = x + \delta^{2/3}\Phi(x,\tilde{y}) + \cdots \tag{4}$$

$$x,\tilde{y} = \delta^{1/3}y,\ K,\ \omega \text{ fixed as } \delta \to 0 \ .$$

If Φ represents the velocity potential in any of the three regions delineated above, the velocity $\vec{q}$ is given by $\nabla\Phi$. On the cowl surfaces and the slip lines denoted generically as $S(\bar{x},\bar{y}) = 0$, we have

$$\vec{q} \cdot \nabla S = 0$$

as the tangency boundary condition. In connection with the slip lines, note that $\delta b_{\underset{\sim}{U}}(x) = \delta^{4/3}\bar{b}_{\underset{\sim}{U}}(\bar{x})$. Moreover, the perturbation pressures for the jet and blending layer are, respectively:

JET

$$\frac{P_j}{P_e} = 1 - \gamma\delta^{2/3}P_j(\bar{x},\bar{y}) + \cdots \tag{5a}$$

where P_e is the mean pressure at the jet exit.

BLENDING LAYER

$$\frac{P_B}{P_\infty} = 1 - \gamma\delta^{2/3}p_B(\bar{x},\bar{y}) + \cdots \tag{5b}$$

where P_∞ is the ambient pressure in the freestream.

EXTERNAL FLOW

$$\frac{P_{EXT}}{P_\infty} = 1 - \gamma\delta^{2/3}p(x,\tilde{y}) + \cdots \ . \tag{5c}$$

By virtue of pressure compatibility on the slip lines, the relation

$$\varphi_{\bar{x}} - \phi_{\bar{x}} = \frac{\omega}{\gamma} \tag{6}$$

holds along the slip lines B'U' and CU in Fig. 21a, which upon tangential integration yields the relations indicated. The constants C_u and C_ℓ are similar to circulations and are obtained from the difference of the potentials at the trailing edges B' and C. The trailing edge behavior and jet turning angle are obtained from (6) and the compatibility relations $\varphi_{\bar{y}} = \phi_{\bar{y}}$ on the slip lines. Local nonuniformities occur at the trailing edges which are anticipated as weak singularities. "Inner inner" expansions for these would require the solution of the full potential equations in these neighborhoods.

To complete the specification of the problem, a far field ϕ_{FF} is necessary. This function should have the property that it asymptotically matches with the outer flow on the boundary of the region R_e. A procedure which provides the necessary nonlinear feedbacks with the near field of the problem in Fig. 21a involves the asymptotic solution of a relevant integrodifferential equation. A heuristic far field derivation in anticipation of this more satisfying approach is described in the next section.

MATCHING OF EXIT/TRAILING EDGE REGION WITH EXTERNAL FLOW

Because of the anticipated jump in the vertical velocity at the trailing edge associated with a jet flap or USB, we assert that the inner limit of the external flow solution which is assumed to be locally harmonic in strained variables in that neighborhood has a logarithmic singularity in the complex perturbation velocity. To simplify the discussion, we consider matching in the context of a jet flap ($x_e = x_{TE}$) for the present. Generalization to more complicated USB cases should present no major new difficulties. As a consequence of the logarithmic singularity assertion, the complex potential behaves like $z \log z$, as $z \to 0$, where $z = x + i\sqrt{K}\,\tilde{y}$ in the vicinity of the trailing edges as

they appear in the external formulation.* Accordingly, in the notation of (6), we assume that

$$\Phi = A\{x \log \tilde{r} - \sqrt{K}\, \tilde{y}\tilde{\theta}\} + \cdots \tag{7}$$

where A is a constant, $\tilde{r}^2 = x^2 + K\tilde{y}^2$, and $\tilde{\theta} = \tan^{-1} \frac{\sqrt{K}\, \tilde{y}}{x}$. In a corresponding manner, we assert that the outer limit of the blending layer solution for Φ associated with the expansion (3) is given by

$$\phi \doteq a\{\bar{x} \log \bar{r} - \sqrt{K}\, \bar{y}\, \bar{\theta}\} + \cdots \tag{8}$$

where a is another constant.

For matching, we introduce intermediate variables x_ξ and y_η given by:

$$x_\xi = \frac{x}{\xi(\delta)} \quad , \quad y_\eta = \frac{y}{\eta(\delta)} \quad \text{fixed as } \delta \to 0 \tag{9}$$

with

$$\delta^{4/3} << \xi << 1$$

$$\delta << \eta << \delta^{-1/3}$$

where the << sign signifies "order of."

In the intermediate limit (9) which implies that

$$x = \xi x_\xi \to 0$$

$$\tilde{y} = \delta^{1/3}\eta y_\eta \to 0$$

*For near critical trailing edges this assumption is invalid.

$$\bar{x} = \frac{\xi}{\delta^{4/3}} x_\xi \to \infty$$

$$\bar{y} = \frac{y_\eta \eta}{\delta} \to \infty \quad ,$$

the variables and various terms appearing in (7) and (8) have the following appearance

$$\bar{\theta} = \tan^{-1} \frac{\sqrt{K}\, \bar{y}}{\bar{x}} \to \tan^{-1} \frac{\sqrt{K}\, \eta y_\eta \delta^{1/3}}{\xi x_\xi} \tag{10a}$$

$$\tilde{\theta} = \tan^{-1} \frac{\sqrt{K}\, \tilde{y}}{x} \to \tan^{-1} \frac{\sqrt{K}\, \eta y_\eta \delta^{1/3}}{\xi x_\xi} \tag{10b}$$

$$\log \bar{r} - \log \sqrt{\frac{\xi^2 x_\xi^2}{\delta^{8/3}} + \frac{\eta^2 y_\eta^2}{\delta^2}} \tag{10c}$$

$$\log \tilde{r} = \log \sqrt{\xi^2 x_\xi^2 + K\delta^{2/3} \eta^2 y_\eta^2} \quad . \tag{10d}$$

On the basis of a comparison of the various elements in Eqs. (10), we find by virtue of (7) and (8) that the perturbation potentials in both regions compare roughly as follows, where the <=> indicates asymptotic correspondence:

$$\delta^{2/3} \Phi \iff \delta^2 \phi + \frac{4}{3}\delta \, (\log \delta) \, \bar{x} \tag{11}$$

providing the limit is taken as $\frac{\eta \delta^{1/3}}{\xi}$ --- fixed = constant = λ as $\delta \to 0$. More precisely, if the external and inner flow solutions are written in terms of intermediate variables, we obtain the following correspondence:

$$A\delta^{2/3}\{\xi x_\xi \log \sqrt{\xi^2 x_\xi^2 + K\lambda^2\xi^2 y_\eta^2} - \sqrt{K}\,\lambda\xi y_\eta \tilde{\theta}\}$$

$$\Leftrightarrow \delta^2 a \frac{\xi x_\xi}{\delta^{4/3}}\left[\log \sqrt{\xi^2 x_\xi^2 + K\lambda^2\xi^2 y_\eta^2} - \frac{4}{3}\log\delta\right] - \sqrt{K}\,\frac{\lambda\xi}{\delta^{4/3}}\, y_\eta \tilde{\theta}$$

$$+ \frac{4}{3}(\delta^2 \log\delta)\frac{\xi x_\xi}{\delta^{4/3}} \quad . \tag{12}$$

The last term is a compensation term added to achieve matching. Presumably, an intermediate solution could be developed to eliminate this rather foreign looking entity whose physical significance is not well understood at this time. Aside from this rather minor difficulty, the result contained in (12) demonstrates that a numerical solution of the problem in Fig. 21a will match with the solution of a global jet flap problem near the trailing edge providing A = a and the far field for the former is given in accord with (12).

"THIN DOMAIN" SPENCE REGION

Another matching is required downstream of the trailing edge, involving the confluence of the wavelike region and the "Spence" zone where pressure and centrifugal forces equilibrate. This regime is reached in the limit of $x,\bar{y}$ fixed as $\phi \to 0$ and leads to the "thin domain" problem shown in Fig. 21b. Here, the streamwise derivatives are negligible in the dominant approximation. Matching with the external flow takes place by "patching" across the slip line with the boundary conditions of compatible normal velocity and pressure as shown in the figure. The inner limit of the thin layer solution represents the jet far field of the problem associated with Fig. 21a.

3.1.1 A Basic Transonic Coflow Problem

Many of the fundamental ideas associated with the problem depicted in Fig. 21b are contained in the unit problem shown in Fig. 22. Here, a jet of velocity U_e exhausts into a coflowing stream with a freestream velocity U. A

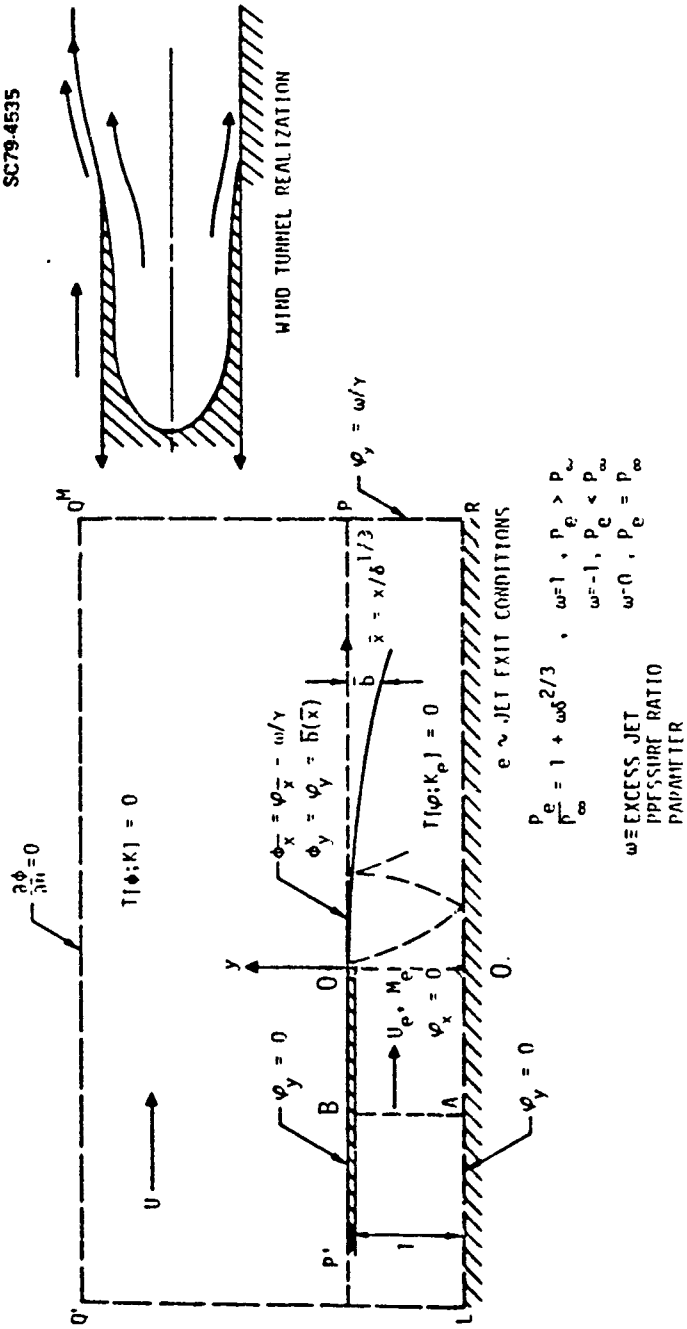

Fig. 22 Transonic coflowing jet problem.

major simplification over the problem given in Fig. 21a is now that the cowl PBO is a flat plate internally and externally as well as the bottom wall surface LSR. Moreover, the lower cowl boundary VC in Fig. 21a is replaced by an infinite wall $y = -1$ in Fig. 22 for this idealization. We assume that conditions are known at some exit station AB, which could be at $x = -\infty$ in the coordinate system indicated, and could correspond to a settling chamber location. Note in this connection that a far field analysis indicates that as station AB tends to $x = -\infty$, the assumed Neumann condition is asymptotically equivalent to a homogeneous Dirichlet one. In particular, with the problem for ϕ based on Fig. 22, a far field representation, obtained from an iterative solution procedure regarding the nonlinear term of the Karman Guderley equation as a weak forcing term, is

$$\varphi(\bar{x},y) = A_1 e^{\pi\bar{x}/\sqrt{K_e}} \cos \pi y + \frac{A_1^2}{8K_e}(\gamma+1)\bar{x}\, e^{2\pi\bar{x}/\sqrt{K_e}} \cos 2\pi y$$

$$+ A_1^2 \frac{(\gamma+1)\pi^2}{8\,K_e^{3/2}} e^{2\pi\bar{x}/\sqrt{K_e}} + A_2 e^{2\pi\bar{x}/\sqrt{K_e}} \cos 2\pi y + \ldots$$

$$\text{as } x \to -\infty \ .$$

Defining the average of a flow quantity g at the station $x = x_0$ as

$$\langle g(x_0,y)\rangle = \text{average of g at } x = x_0 \equiv \int_{-1}^{0} \varphi(x_0,y)\, dy$$

we have in particular, using the foregoing asymptotic solution specialized to $x_0 = 1$,

$$\langle \varphi(-1,y)\rangle = A_1^2 \frac{(\gamma+1)\,\pi^2}{8\,K_e^{3/2}} e^{-2\pi/\sqrt{K_e}} \ .$$

Moreover, we find that

$$\langle \varphi_x(-1,y)\rangle = \frac{2\pi}{\sqrt{K_e}} \langle \varphi(-1,y)\rangle \ .$$

An interpretation of the constant A appearing in the foregoing expressions is obtained by using Green's theorem to derive a nonlinear integro-differential equation for φ. From the formulation of Fig. 22, it is possible to evaluate the boundary terms on the boundaries of the rectangular domain AB and PR. The appropriate integral theorem is

$$\phi = \frac{\gamma+1}{2K} \int_{-1}^{0} [\phi_\xi^2 G]\Big|_0^\infty - \int_{-\infty}^{\infty} G_\xi \phi_\xi^2 d\xi d\eta$$

$$- \frac{1}{\pi} \int_0^\infty b'(\xi) \ln \sinh \frac{\pi(x - \xi)}{2} d\xi + \frac{c}{2} x \ ,$$

where

$$c = \omega/\gamma .$$

Approximation of this expression for $x \to \pm \infty$, with interrelationships between $b(\infty)$ and c to be derived subsequently, is consistent with the asymptotic expansion of φ for $x \to -\infty$ previously given and the result

$$\phi = \frac{c}{2} x \quad \text{as} \quad x \to \infty$$

where the partial integration boundary term in the first integral of the Green's theorem expression dominates the double integral and is approximately $\pm cx^2/2$ as $x \to \infty$, and the contribution of the lower limit vanishes. This change in signs is of decisive importance in obtaining the desired upstream and downstream boundary conditions. Furthermore, the Green's theorem expression shows that

$$A_1 = \frac{1}{2\pi} \int_0^\infty b'(\xi) \, e^{-\pi\xi} \, d\xi \ ,$$

i.e., A_1 is a moment of the source distribution associated with the deflected slip line.

Returning to the configuration at hand, we note that in some sense, this system is a simple idealization of an inviscid ejector. A sketch of a wind tunnel realization is also shown in Fig. 22. An analytical/computational solution has been developed to study this problem, with the objective of addressing the following issues associated with the problem of Fig. 21b:

1. Under what circumstances is the jet far field supersonic if the initial conditions are subsonic?

2. What is the degree of downstream penetration of an initially supersonic jet, i.e., how long is the supersonic region?

3. For (2), how do the parameters K, K_e, ω and γ affect the penetration length and the relaxation and decay of the complex nonlinear wave interaction process to uniform conditions?

4. Under what circumstances does a throat arise in the jet?

5. Are any of the ideas associated with the one dimensional flow theory of under- and over-expanded plumes applicable to delineate the various flow regimes in this two-dimensional context?

6. If the streamwise scale of the reflections is $O(\delta^{1/3})$, then the external flow sees a wavy wall boundary condition if the jet remains supercritical. In this case, the basic slip line shape is modulated by corrugations induced by wave reflections, and the relaxation length of the interaction process may not be of $O(\delta^{1/3})$. Are Poincare limit process expansions of the type given in Eqs. (1) - (5) adequate to treat the problem, or is "two-timing" required?

During this phase of the research, a partial answer to some of these questions has been obtained in connection with an integral mass conservation form of the KG equation for the flow in the jet, which is

$$\int_{-1}^{0} dy \int_{0}^{\infty} d\bar{x} \left\{ \left(K_e \varphi_{\bar{x}} - \frac{\gamma+1}{2} \varphi^2_{\bar{x}} \right)_{\bar{x}} + \varphi_{yy} \right\} = 0 \quad . \tag{13}$$

If the jet slip line is given by $y - \delta^{4/3} B(\bar{x})$, where $\bar{x} = \delta^{-1/3} x$, then the tangency condition is

$$\phi_y(\bar{x},0) = B'(\bar{x}) \quad . \tag{14}$$

Noting that $B(0) = 0$, (13) and (14) lead to the relation

$$B(\infty) = - \int_{-1}^{0} \left(K_e \varphi_{\bar{x}} - \frac{\gamma+1}{2} \varphi^2_{\bar{x}} \right) \Big|_{\bar{x}\to\infty} dy \quad . \tag{15}$$

Furthermore, if we assert that ϕ_y and $\varphi_y \to 0$ as $\bar{x} \to \infty$, then the slip line pressure condition

$$\phi_{\bar{x}}(x,0) = \varphi_{\bar{x}}(x,0) - \omega/\gamma \tag{16}$$

implies if further, ambient pressure is achieved in the freestream, i.e., $\phi_{\bar{x}}(x,0) \to 0$ as $x \to \infty$, that

$$\varphi_{\bar{x}} \to \omega/\gamma \text{ as } \bar{x} \to \infty \tag{17}$$

at least on the jet boundary $y = 0$. If we continue this in the interval $-1 < y < 0$, we note that it is a particular solution of the K.G. equation satisfying the wall boundary condition $\varphi_y(x,0) = 0$. Such a solution represents an asymptotic velocity distribution infinitely far downstream which is uniform across the jet and is intuitively reasonable on physical grounds. By contrast to the limit $x \to -\infty$, the second order exponentially small corrections for $x \to \infty$ must be determined from the full K.G. equation rather than a Prandtl Glauert approximation. For critical conditions at this location

$$\phi_{\bar{x}} = \frac{K_e}{\gamma+1} \quad , \tag{18}$$

which is achieved by virtue of (17) when

$$K_e > \frac{\gamma+1}{\gamma} \tag{19}$$

if $\omega = 1$. Equation (17) with (15) implies that

$$\bar{b}(\infty) = \frac{\omega}{\gamma}\left\{\frac{\gamma+1}{2\gamma}\,\omega - K_e\right\} \quad . \tag{20}$$

Tables 2 and 3 as well as Figs. 23 and 24, summarize cases that can occur by virtue of the previous formulas for $K > 0$. These cases are significant for USB application. Here, x_t denotes the streamwise position of the throat or minimum area section of the jet. Only one configuration (Case V) exists for $\omega = 0$. For $\omega = 1$ and $\omega = -1$, however, many configurations exist, and a diagram delineating the various flow regimes is given in Fig. 23. Sketches of the corresponding jet shapes are given in Figs. 25 and 26. Note that Case V represents a uniform flow for the jet which shears the external freestream, i.e., both flows are uniform in this case. Also, the indicated expansion and contraction of the jet is consistent with one-dimensional reasoning for the various cases. Note, however, that the question of smooth, shockless decelerations and the realizability of these inviscid cases must be resolved through experiments and other analyses which could assess the role of viscous entrainment along the shear layer. Computational studies could illuminate the question regarding the existence of shocks in the jets.

In related IR&D work, the case of K_e, $K \to -\infty$ has been analyzed, involving decay processes associated with radiation of the jet pressure field to the external coflow through transmitted waves. If M_e and M_∞ denote jet exit and freestream Mach numbers, respectively, then relaxation to uniform state takes place through a wave train produced by multiple wave reflections from the wall and slip line. For the N^{th} downstream Mach diamond, the analytical solution of this problem indicates that the wall pressure C_p behaves like

TABLE 2 - OCCURRENCE OF CRITICAL CONDITIONS AND THROATS IN JET
($K > 0$)
($\omega = 1,0$)

Case No.	ω	Jet Exit Supersonic?	Range of K_e	$-b(\infty)$	Streamwise Position of Throat (x_t)	Mach No. at ∞	Monotone Slipline Admissible?	Remarks
I	1	No	$0 < K_e < \frac{\gamma+1}{2\gamma}$	>0	$<\infty$	>1	No	$\varphi_x(\infty) = \gamma^{-1}$ $P_e > P_\infty$
Ia	1	No	$K_e = \frac{\gamma+1}{2\gamma}$	0	$<\infty$	>1	No	
II	1	No	$\frac{\gamma+1}{2\gamma} < K_e < \frac{\gamma+1}{\gamma}$	<0	$<\infty$	>1	No	
IIa	1	No	$K_e = \frac{\gamma+1}{\gamma}$	<0	∞	$=1$	Yes	
III	1	No	$\frac{\gamma+1}{\gamma} < K_e < \infty$	<0	∞	<1	Yes	
IV	1	Yes	$-\infty < K_e < 0$	>0	0	>1	Yes	
V	0	Yes and No	$-\infty < K_e < \infty$	0	-	$\gtrless 1$	Yes	$\varphi_x(\infty) = -\gamma^{-1}$ $P_e = P_\infty$ $\varphi = \phi = 0$ Pure slip flow (No Perturbations)

TABLE 3 - OCCURENCE OF CRITICAL CONDITIONS AND THROATS IN JET

$(K > 0)$

$(\omega = -1)$

Case No.	ω	Jet Exit Supersonic?	Range of K_e	$\delta(\infty)$	Streamwise Position of Throat (x_t)	Mach No. at ∞	Monotone Slipline Admissible?	Remarks
VI	-1	Yes	$-\infty < K_e < \frac{\gamma+1}{\gamma}$	<0	∞	>1	Yes	$\varphi_x(\infty) = -\gamma^{-1}$ $p_e < p_\infty$
VIa		Yes	$K_e = -\frac{\gamma+1}{\gamma}$	<0	∞	1	Yes	
VII		Yes	$-\frac{\gamma+1}{\gamma} < K_e < -\frac{\gamma+1}{2\gamma}$	<0	$<\infty$	<1	No	
VIIa		Yes	$K_e = -\frac{\gamma+1}{2\gamma}$	$=0$	$<\infty$	<1	No	
VIII		Yes	$-\frac{\gamma+1}{2\gamma} < K_e < 0$	>0	$<\infty$	<1	No	
VIIIa		Sonic	$K_e > 0$	>0	0	<1	Yes	
IX		No	$K_e > 0$	>0	0	<1	Yes	

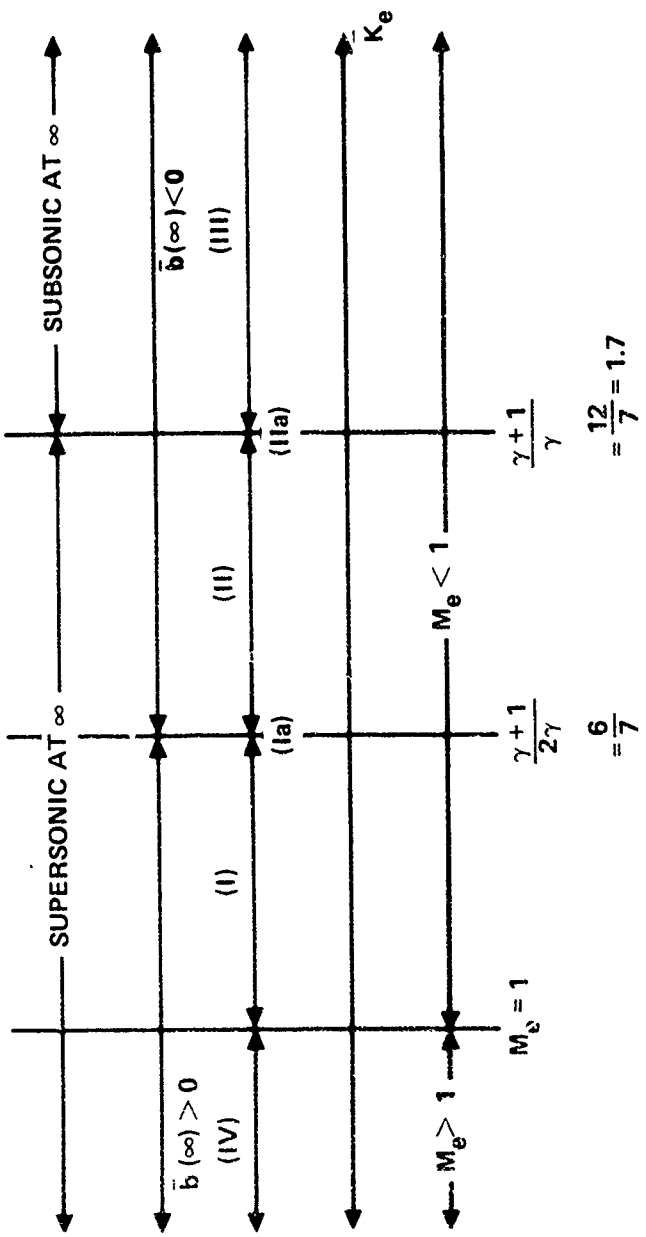

Fig. 23 Selection diagram for jet downstream criticality and throat formation, $\omega = 1$.

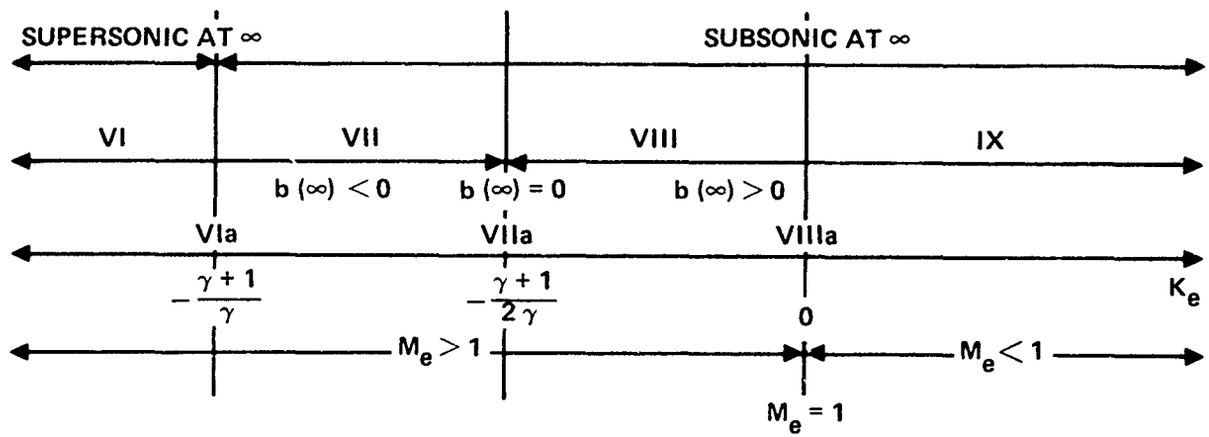

Fig. 24 Selection diagram for jet downstream criticality and throat formation, $\omega = -1$.

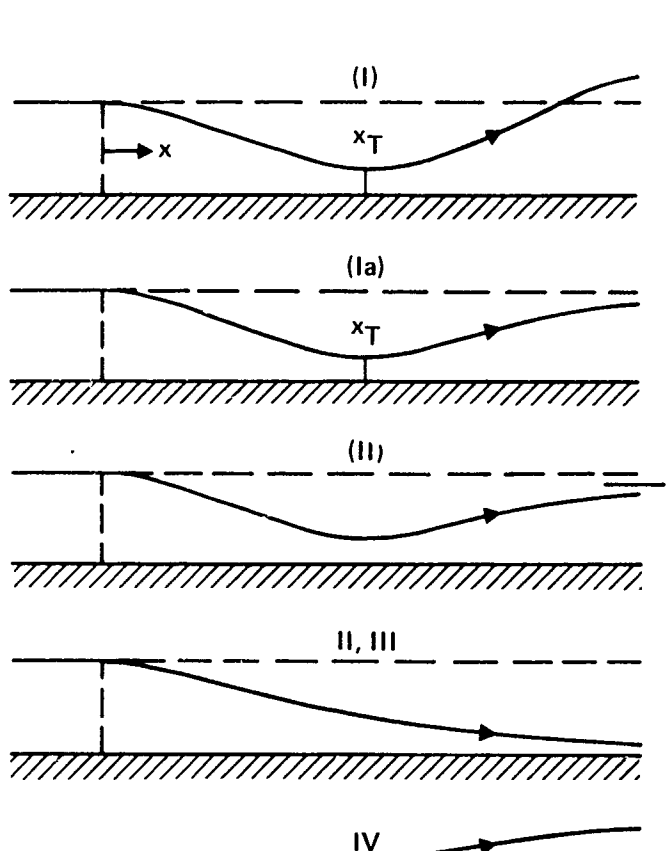

Fig. 25 Slip line shapes for various cases in Table 2, $\omega = 1, 0$.

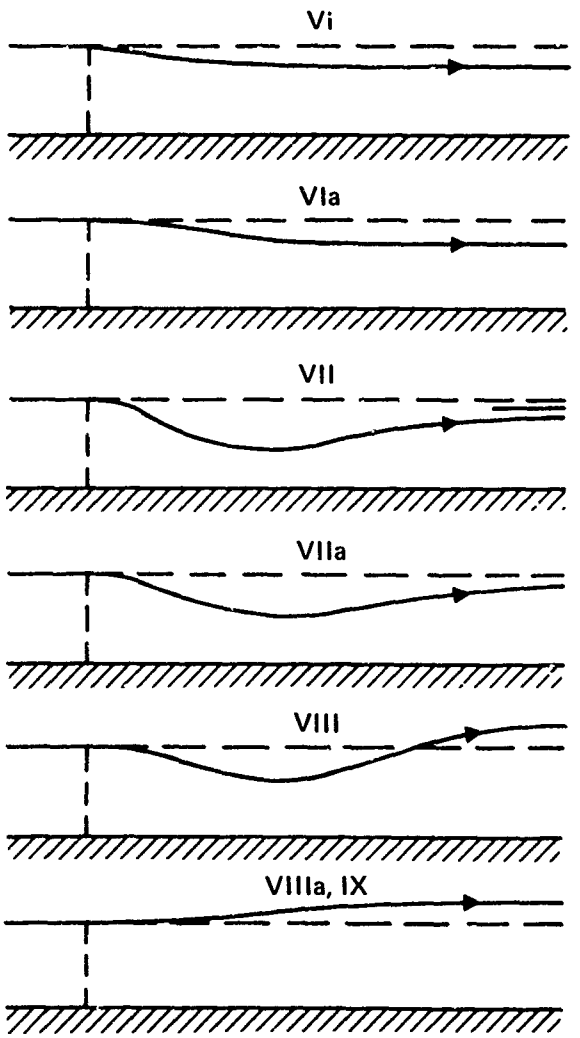

Fig. 26 Slip line shapes for various cases in Table 3, $\omega = -1$.

$$C_p \triangleq -\frac{4\kappa}{1+\alpha}\left\{1 - (-1)^N \exp\left(-N \log \alpha\right)\right\} \text{ as } N\to\infty \qquad (21)$$

where

$$\alpha \equiv \frac{\frac{M_e^2}{M_\infty^2} - \frac{\beta_e}{\beta}}{\frac{M_e^2}{M_\infty^2} + \frac{\beta_e}{\beta}} = \text{REFLECTION COEFFICIENT} \quad , \quad \kappa = \frac{\omega}{\gamma M_\infty^2\left[\frac{M_e^2}{M_\infty^2} + \frac{\beta_e}{\beta}\right]} = \text{LUMPED PRESSURE RATIO PARAMETER}$$

$$\beta = \sqrt{M_\infty^2 - 1} \quad , \quad \beta_e = \sqrt{M_e^2 - 1} \ .$$

If φ^* is the perturbation potential in this process related to the exact potential by the asymptotic expansion

$$\frac{\Phi_j}{U_e} \triangleq x + \delta\varphi^*(\bar{x}^*, \bar{y}) + O(\delta^2)$$

for $\bar{x}^* = x/\delta$, $\bar{y} = (y - \delta b_\ell(x))/\delta$, M_e, M_∞ fixed as $\delta\to 0$, then φ^* satisfies an initial boundary value problem for the supersonic Prandtl Glauert equation giving the damped wave train solution

$$\frac{\varphi}{\kappa} = (x^* + \beta_e\bar{y}) \sum_{n=0}^{\infty}(-\alpha)^n H\left[x^* + \beta_e\bar{y} - (2n+1)\beta_e\right] + (x^* - \beta_e\bar{y}) \sum_{n=0}^{\infty}(-\alpha)^n H\left[x^* - \beta_e\bar{y} - (2n+1)\beta_e\right] \qquad (22)$$

where

$$H(x) = 1 \quad , \quad x > 0$$
$$= 0 \quad , \quad x < 0$$

and $0 < \alpha < 1$.

The problem of incompressible flow is also interesting. With a slight change in normalizations, we have for this case

$$\Delta\varphi = 0 \qquad \text{in} \begin{cases} -\infty < x < \infty \\ -1 < y < 0 \end{cases}$$

$$\Delta\phi = 0 \quad , \quad y > 0$$

with the boundary conditions

$$\varphi_x(-\infty,0) = 0$$
$$\varphi_y(x,0) = \phi_y(x,0) = 0, \quad x < 0$$
$$\varphi_y(x,0) = \phi_y(x,0) = b'(x), \; x > 0$$
$$\varphi_y(x,-1) = 0$$
$$\varphi_x(\infty,0) = c \equiv \frac{\omega P_\infty}{\rho U^2}$$
$$\varphi_x(x,0) - \phi_x(x,0) = c, \; x > 0 \; ,$$

where ρ is the density, and P_∞ and U are the ambient pressure and freestream velocity of the external flow. Cartesian coordinates similar to Fig. 22 are used. Also, the jet pressure P_j is assumed to be slightly different from that of the freestream measured by the parameter δ in a similar manner to that utilized in the previous developments, i.e.,

$$\frac{P_j}{P_\infty} = 1 + \omega\delta$$

with ω = -1, 0 or 1. Furthermore, the slip line is given as $y = \delta b(x)$, $x > 0$. Correspondingly, we assume that the jet velocity V_j is expressed as

$$\frac{U_j}{U} = 1 + \nu\delta \quad .$$

Finally, the external flow vector is represented as

$$\frac{\vec{q}}{U} = (1 + \delta\phi_x)\vec{i} + \delta\phi_y\vec{j} + \mathcal{O}(\delta^2)$$

and the jet is

$$\frac{\vec{q}}{U} = (1 + \delta\phi_x)\vec{i} + \delta\phi_y\vec{j} + \mathcal{O}(\delta^2)$$

where $\vec{i}$ and $\vec{j}$ are unit vectors in the x and y directions, respectively. As in the other speed regimes, two different potentials are needed because of the different Bernoulli constants in the jet and external flows. The homogeneous Neumann conditions at $x = -\infty$ establishes a pressure level for the jet. The corresponding inhomogeneous Neumann condition at $x = \infty$ is consistent with equilibration of the pressure to the ambient level of the external flow (P_∞).

The aforementioned boundary value problem leads to the following singular integral equation for $b'(x)$, when Green's function representations for ϕ and φ are used in their respective domains of validity and the boundary conditions are applied:

$$\int_0^\infty b'(\xi)\left\{\tanh(x-\xi) - \frac{1}{x-\xi}\right\}d\xi = c\left(\pi - \frac{1}{2}\right)$$

which can be solved by Weiner-Hopf,[22] conformal mapping - Green's function methods, or numerical procedures. This formulation can be used to check the well-posedness of the transonic problem and the appropriateness of the numerical procedures which we will now discuss.

3.1.2 Basic Ideas for the Computational Solution of the Problem of Fig. 22

Because of the nonlinearity of the flow problem represented in Fig. 22, numerical methods must be used. The approach that has been implemented employed a SLOR Murman-Cole type dependent difference scheme with Jameson damping, in which the QP slip line pressure boundary condition is tangentially integrated to give

$$\phi(\bar{x},0) = \varphi(\bar{x},0) - \frac{\omega}{\gamma}\bar{x} + C \quad , \quad x > 0 \qquad (23)$$

where $C = \phi(0,0) - \varphi(0,0)$ is updated in successive sweeps. Equation (23) and the relation

$$\phi_{\bar{y}}(\bar{x},0) = \varphi_{\bar{y}}(x,0) \quad , \quad x > 0 \ , \tag{24}$$

with the other boundary conditions indicated in the figure, define the numerical problem. In this connection, a far field in the external field given by

$$\nabla\phi = \mathcal{O}(r^{-1}) \doteq 0 \quad , \quad \text{as } r^2 = \bar{x}^2 + K\bar{y}^2 \to \infty \tag{25}$$

is prescribed on the finitely large computational boundaries P'Q', Q'Q and QP. Compatible with (25),

$$\varphi_{\bar{x}} \to \omega/\gamma \quad \text{as} \quad \bar{x} \to \infty$$

which also is satisfied on the finite computational boundary PR. For ease of calculation and programming logic, dummy matrix entries have been used in the region LABP' in Fig. 22.

Details of Numerical Procedure

In some respects, the numerical procedure is similar to that discussed in Ref. 5. Referring to the formulation in Fig. 22, for interior points, the transonic potential equation for the jet region and external region in divergence form is discretized by using central differences when the equation is elliptic and backward differences when it is hyperbolic. Parabolic and shock point operators are employed when required. Both the Neumann boundary conditions and the subsonic and/or supersonic jet conditions are discretized as described in Ref. 5. New to this problem are the interface conditions (24) and (25).

The former can be written as

$$\phi(x,0) - \varphi(x,0) = \nu(x - x_{ITF}) + c_{ITF} \quad . \tag{26}$$

Here, $\nu = \pm 1/\gamma$ and c_{ITF} is a constant to be determined. The quantity x_{ITF} is the x-coordinate of the cowl lip.

Since no mesh points are placed on the line y=1, c_{ITF} is determined by extrapolation of ϕ from above and ϕ from below the slip line along $x=x_{ITF}$. Thus, $c_{ITF} = \varphi(x_{ITF},1) - \varphi(x_{ITF},1)$.

Equation (26) is inserted into the discretization of the operator ϕ_{yy} at the first mesh point above the interface by replacing $\phi_{i,j-1}$ by

$$\phi_{i,j-1} - \nu(x_i - x_{ITF}) - c_{ITF} \quad .$$

Similarly, ϕ_{yy} below the interface uses $\phi_{i,j+1}$ replaced by $\phi_{i,j+1} + \nu(x_i - x_{ITF}) + c_{ITF}$. This type of differencing guarantees that Eq. (26) is automatically satisfied. The relaxation sweep is carried out as in Ref. 5 from upstream to downstream, where homogeneous Dirichlet conditions are utilized in Station AB in Fig. 22.

INITIAL PARAMETRIC WALL JET STUDIES

Prior to dealing with conditions (23) and (25), the implications of the initial conditions and pressure gradients in the problem of Fig. 22 were investigated in parametric studies that were conducted with an extended version of our original submerged wall jet code described in previous sections. The problem studied was in the previous notation:

$$\bar{T}[\varphi;K_e] = [K_e - (\gamma+1)\varphi_{\bar{x}}]\varphi_{\bar{x}\bar{x}} + \varphi_{\bar{y}\bar{y}} = 0$$

with

$$\varphi_{\bar{x}}(0,\bar{y}) \equiv \text{PHIXO} = g(\bar{y})$$

$$\varphi(0,\bar{y}) = h(\bar{y}) \quad , \quad \text{(specified for hyperbolic exits)}$$

$$\varphi(\bar{x},0) = G(\bar{x}) \quad , \quad x > 0$$

$$\varphi_{\bar{y}}(\bar{x},-1) = 0$$

with

$$\varphi(\bar{x},\bar{y}) \doteq \varphi_{FF}(\bar{y}) \quad \text{as} \quad \bar{x} \to \infty \quad .$$

Note that in contrast to the formulation including Eqs. (23) and (24), which involves the determination of the pressure on the slip line, the formulation here assumes this variation.

Table 4 provides a tabulation for some of the cases run for this problem where φ_{FF} was assumed to vanish for these studies. Comments on the qualitative features of these examples are provided in this table.

From these studies, Figs. 27 and 28 illustrate typical results for $K_e = 0.1$ for the effect of the initial velocity g(y) on penetration for a submerged jet with $\varphi_{\bar{x}}(\bar{x},0) = 0$. Here, $\bar{C}_p \equiv (C_p)/(\delta^{2/3})$, and $\bar{C}_p^*$ is the critical pressure. For h = -1, the jet remains subcritical. For the h > 0 cases, it is evident that the shock terminating the supersonic region moves progressively further downstream with supercritically increasing exit velocity.

Figures 29 and 30 depict the effects of assigning a coflow pressure gradient along the slip line $\varphi_{\bar{x}}(\bar{x},0) = 1$ as compared to the submerged jet case, $\varphi_{\bar{x}}(x,0) = 0$. The former is crudely analogous to (23). It is evident that the pressure gradient has a dramatic influence in accelerating the flow and prolonging the supersonic zone. This fact could affect the matching with the Spence region for the problem of Fig. 21a in the inherent assumption that the wave interaction zone there is $\mathcal{O}(\delta^{4/3})$.

TABLE 4 - PARAMETRIC SUMMARY OF RUNS

Case	$\phi_x(0,y)$	$\phi(0,y)$	$\phi_x(x,1)$	$\phi(x,1)$	K	$M_{SUP.}$	$\phi_y(x,0)$	Comments
1	1.0	0	0	0	0.1	686	0	Mostly elliptic. Exit hyperbolic, far field elliptic.
2	0.1	0	0	0	0.1	118	0	Completely elliptic except jet exit which is hyperbolic.
3	1.0	0	0	0	10^{-3}	764	0	Jet exit supersonic.
4	1.0	0	1.0	x	10^{-3}	2652	0	Mostly hyperbolic with elliptic far field.
5	1.0	0	1.0	x	-10^{-3}	2652	0	Mostly hyperbolic with elliptic far field.
6	1.0	0	0	0	10^{-5}	0	0	
7	-1.0	-	0	0	0.1	0	0	Completely elliptic.
8	1.0	0	0	0	0.1	1648	-2x,(0,1)	Larger supersonic region than -2,(1,2)without wall. 0,(2,∞)
9	2.0	0	0	0	0.1	1435	-2x,(0,1)	Supersonic region smaller than -2,(1.2)case with less blowing. 0,(2,∞)
10	2.0	0	0	0	0.1	1074	0	Smaller supersonic region than case with wall.
11	1.0	0	0	0	0.1	1648	-2x,(0,1) -2,(1,2) 0,(2,3.8)	$\phi(x,0) = C_1$ in (3.8,6.2). Field similar to Case 8 without slip line except for in (3.8,0).
12	0	0	1.0	x	-0.5	2838	0	Supersonic everywhere.
12a	0	0	1.0	x	-0.5	2838	C_1,(3.8,6.2)	Supersonic everywhere (with wall).
13	0	0	-1.0	-x	-0.5	85	0,(0,3.8) C_1,(3.8,6.2)	Subsonic jet exit. Very small supersonic far field.
14	0	0.25 y^2	1.0	x	-0.5	2810	0	Supersonic almost everywhere.
15	0	0.5 y^2	1.0	x	-0.5	2784	0	Supersonic almost everywhere.
16	0	0	1.0	x	0.5	0	0	Supersonic everywhere.
17	0	-	-1.0	-x	0.5	0	0	Subsonic everywhere.
18	0	0	0.5	0.5 x	-0.5	2838	0	Supersonic everywhere.
19	0	0	-0.5	-0.5 x	-0.5	0	0	Subsonic everywhere.

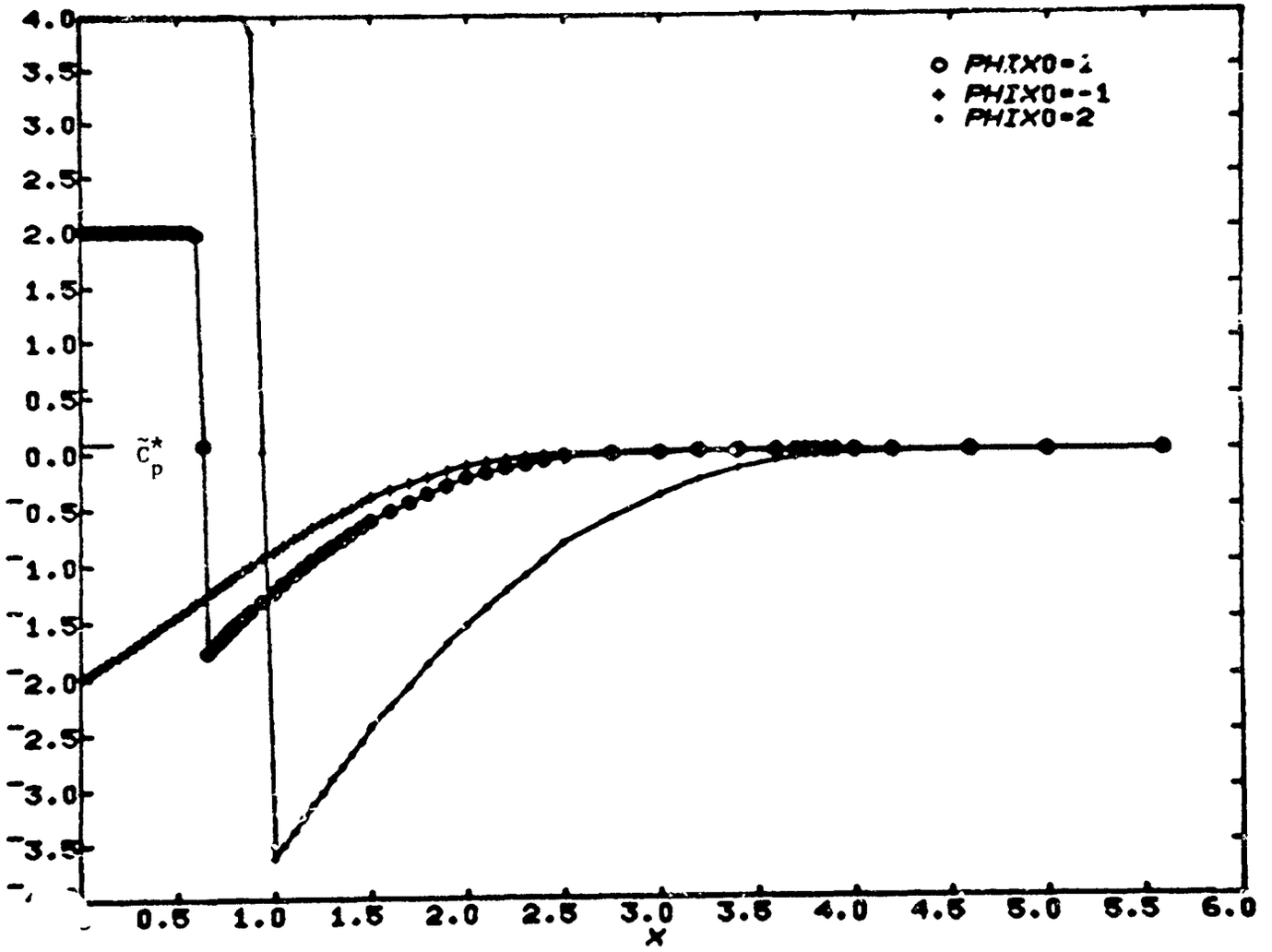

Fig. 27 Submerged wall jet studies - wall pressures - initial condition effect on extent of penetration of supersonic zone, K_e = 0.1, PHIX0 $\equiv \varphi_{\bar{x}}(0,y)$.

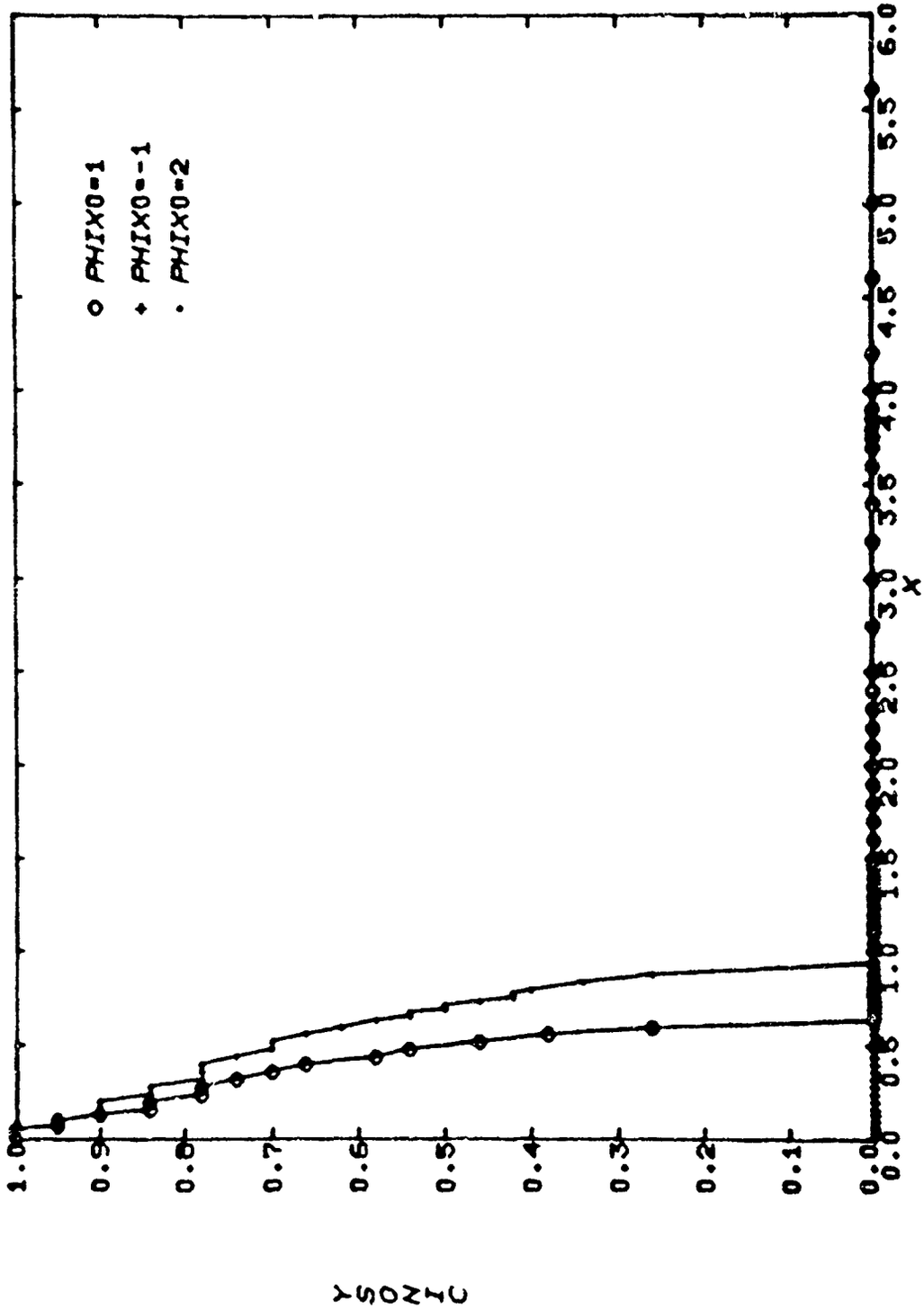

Fig. 28 Submerged wall jet studies (continued) - initial condition effect on extent of penetration of supersonic zone, K_e = 0.1, YSONIC = position of sonic line.

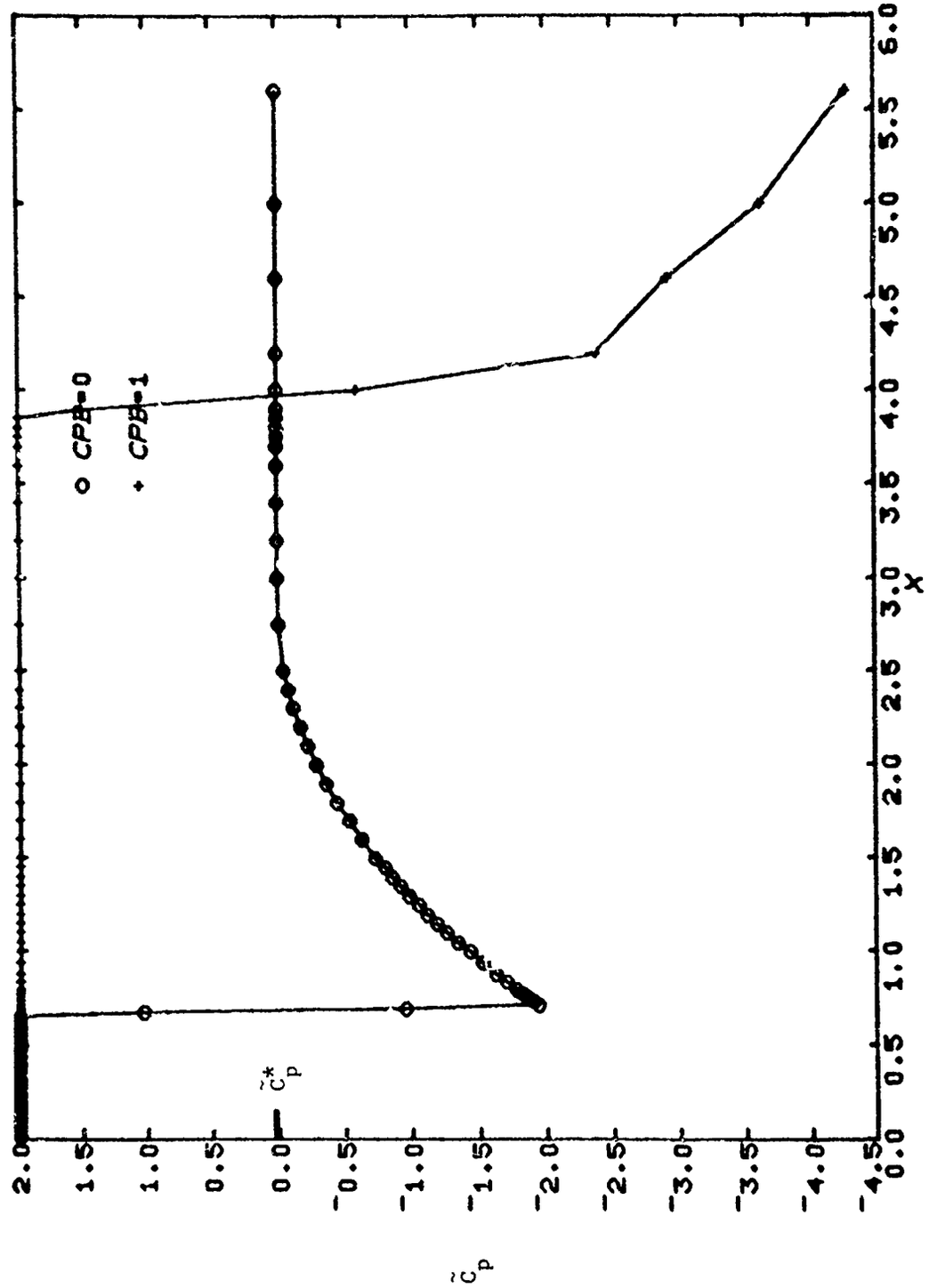

Fig. 29 Coflowing wall jet studies - effect of slip line pressure gradient on wall pressures, CPB=0=>$\varphi_x(x,0) = 0$, CPB=1=>$\varphi_x(x,0) = 1$, $K_e = 10^{-3}$.

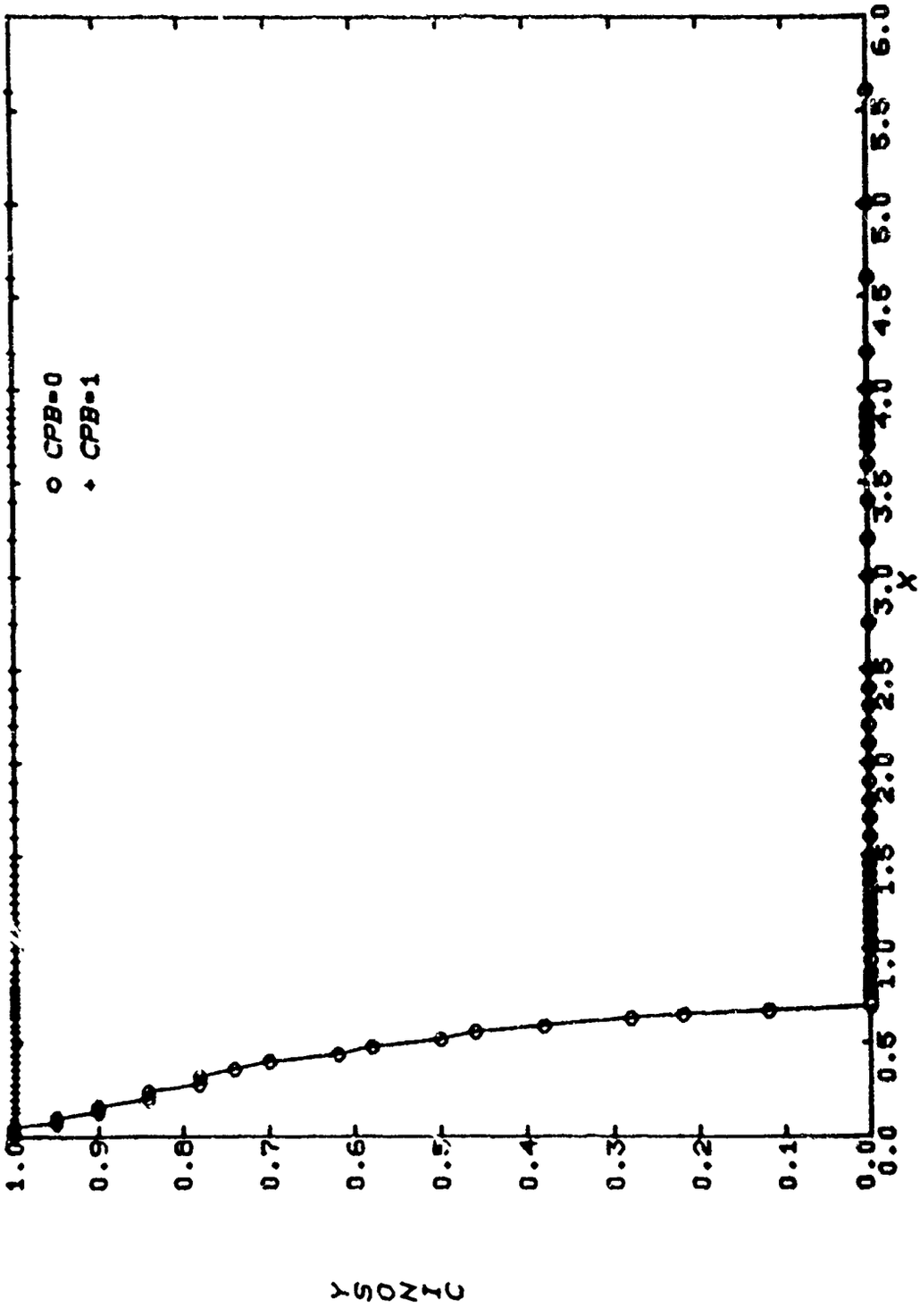

Fig. 30 Coflowing wall jet studies (continued) - effect of slip line pressure gradient on sonic line shape, $K_e = 10^{-3}$.

3.1.3 Results for Complete Problem

Applying the numerical procedure described previously to treat the problem involving Eqs. (23) and (24), results were obtained for illustrative cases. In this connection, a typical three-dimensional relief plot of Mach number as a function of spatial coordinates x and y related to the formulation in Fig. 22 is shown in Fig. 31, with y now measured from the bottom wall. In the legend, recall that the quantity ω is given by

$$\omega = \left(\frac{P_e}{P_\infty} - 1 \right) / \delta^{2/3}$$

where P_e is the jet static pressure, P_∞ is that of the freestream, and $\phi^{2/3}$ is a small parameter measuring the indicated excess pressure ratio. The quantity ω denotes a sign index which can be 1, -1, or zero. In addition, the parameters K_e and K_j are defined as

$$K_e = (1 - \bar{M}_j^2)/\delta^{2/3} \quad , \quad K_j = (1 - M_\infty^2)/\delta^{2/3} \quad .$$

For the case indicated in Fig. 31, $\omega = 1$, $K_e = 1$, and $K_j = \frac{\gamma+1}{\gamma}$. In the code, the jet exit potential $\varphi(-1,y)$ was assumed zero. In contrast to the homogeneous Neumann conditions assumed in the derivation of Table 1, this procedure has been justified in an earlier section of this report.

In spite of the finite location of the jet upstream boundary, the results obtained are roughly compatible with those predicted in Table I. Figure 31 shows a strong acceleration of the initially subsonic jet flow embedded in a subsonic stream jet flow due to choking associated with constriction of the jet slip line (not shown). A terminating shock (supersonic to subsonic) forms, giving sonic conditions infinitely far downstream.

Figure 32 depicts a flow pattern associated with an initally supersonic jet in a subsonic stream. The acceleration is smooth and isentropic. Both figures typify wave interaction regimes that can result in global modifications of the flow field, resulting from a change in the Kutta condition wake structure and interaction with the viscous wall jet on upper surface blown airfoils.

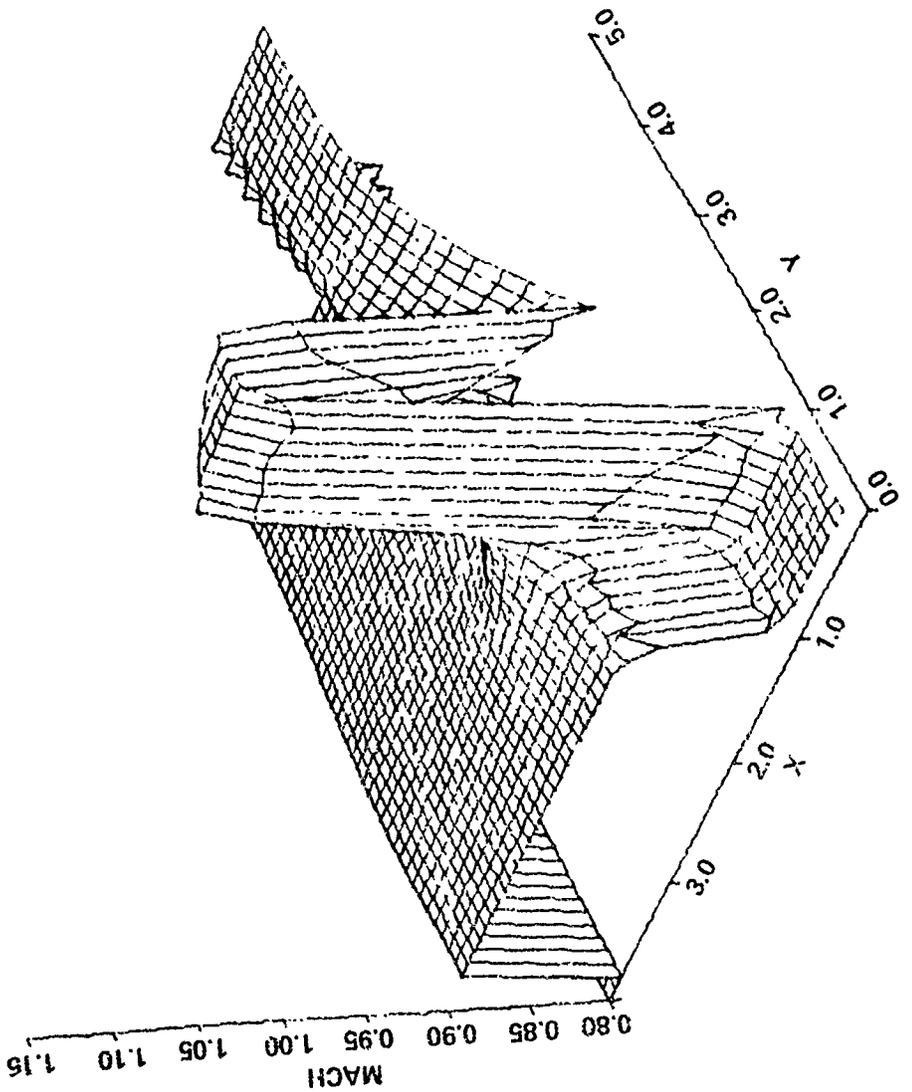

Fig. 31 Mach number distribution for coflowing wall jet, case 2a, $\omega = 1$, $K_e = 1$, $K_j = (\gamma + 1)/\gamma$.

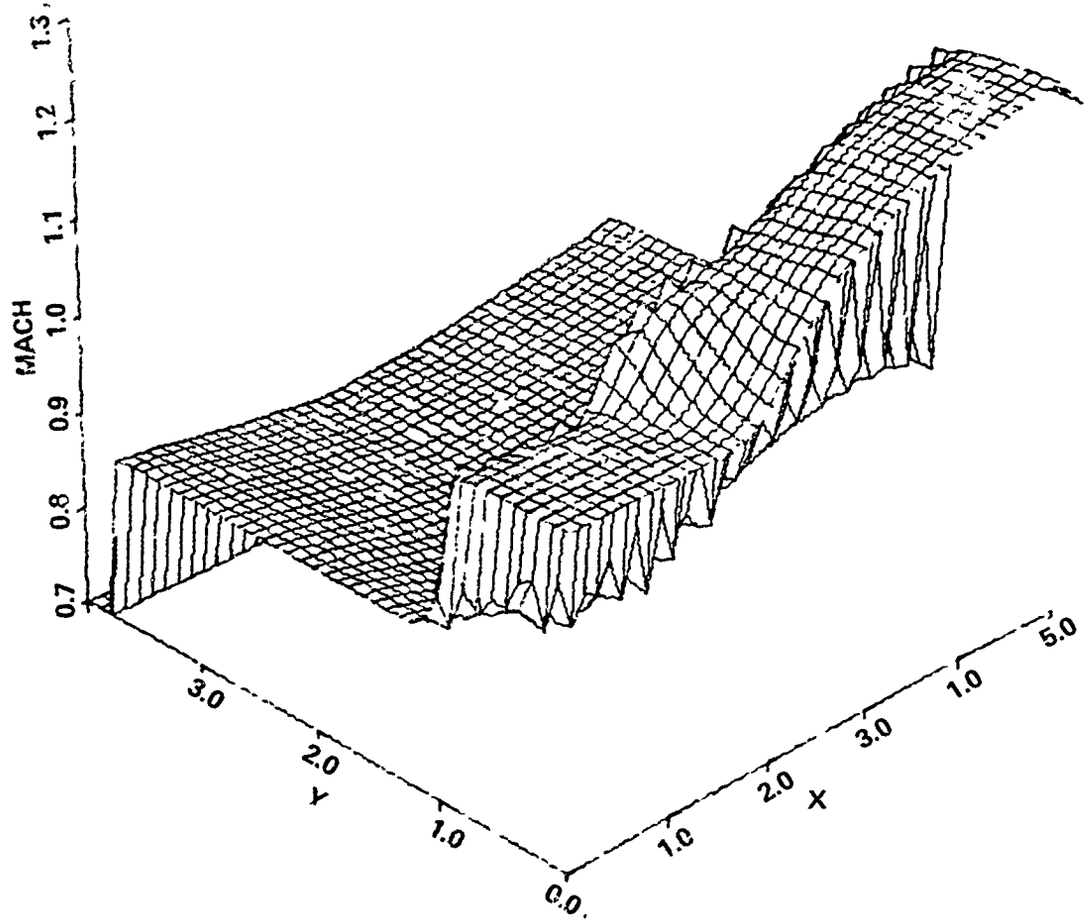

Fig. 32 Mach number distribution for coflowing wall jet, case 4b, $\omega = 1$, $K_e = 1$, $K_j = -0.4$.

3.2 Solution of Blown Airfoil Problem and Relevant Flow Structures

In this section, in contrast to the detailed jet studies previously given, we change focus and concentrate on various formulations and analyses which are intended as a critical assessment of different aspects of the jet flap formulation given in Ref. 1 and its extension to USB for incompressible and compressible flows. Whereas the previous discussions have concentrated on wall jet flows relevant to the upper surface blown problem, this discussion will treat other formulational issues. In particular, as a basis for the thin airfoil and small disturbance models, the thin jet approximation is described in Section 3.2.1 in terms of a systematic asymptotic expansion procedure for incompressible flows. This study is used as a basis for obtaining boundary conditions across the jet. The generalization of these developments to compressible flow is straightforward and therefore not provided. Section 3.2.2 provides a discussion of the trailing edge region from the viewpoint of a nonuniformity of the thin jet theory as well as the generalized Kutta condition for USB. Inherent in this aspect is the geometry of the dividing streamline at the trailing edge, which is a necessary condition for the determination of the jet sheet free boundary. Arguments are provided to substantiate tangency to the upper surface, providing the jet stagnation pressure is greater than that of the external flow. Also indicated is how the small disturbance jet flap formulation of Ref. 5 is modified with USB. Finally, Section 3.2.3 gives results from a computational solution based on the inviscid small disturbance formulation indicated in Fig. 20b. In this section, transonic USB airfoils are analyzed and comparisons are made with experiment. Factors associated with the discrepancies are considered and refinements are proposed to improve the realism of the model, leading to the discussion of the viscous model given in Section 4.

3.2.1 Thin Jet Theory

As an essential ingredient of a small disturbance formulation, the jet structure is developed in this section for purposes of specification of the boundary conditions. In particular, it will be shown how the Spence theory of Ref. 1 can be derived and refined from a systematic approximation procedure.

Referring to Fig. 33, a section of the jet is shown. A curvilinear coordinate system is embedded in the jet as indicated. The lines η = constant are parallel to a reference line (the ξ axis) which is the (flux) center line if the jet is symmetric, or the wall for a wall jet case. In this coordinate system, the lines ξ = constant are normal to ξ axis. In what follows, the incompressible case will be discussed. The generalizations to compressible flow are straightforward.

Within the indicated coordinate system, the exact equations of motion are

Continuity

$$\frac{\partial}{\partial \xi} q_\xi + \frac{\partial}{\partial \eta} h\, q_\eta = 0 \tag{27a}$$

ξ - Momentum

$$\frac{q_\xi}{h} \frac{\partial q_\xi}{\partial \xi} + q_\eta \frac{\partial q_\xi}{\partial \eta} + \frac{q_\xi q_\eta}{h} \frac{\partial h}{\partial \eta} = \frac{-1}{\rho h} \frac{\partial P}{\partial \xi} \tag{27b}$$

η - Momentum

$$\frac{q_\xi}{h} \frac{\partial q_\eta}{\partial \xi} + q_\eta \frac{\partial q_\eta}{\partial \eta} - \frac{q_\xi^2}{h} \frac{\partial h}{\partial \eta} = - \frac{1}{\rho} \frac{\partial P}{\partial \eta} \tag{27c}$$

where h, the metric coefficient when related to the differential arc length in Cartesian (x,y) coordinates is

$$\begin{aligned} dx^2 + dy^2 &= h^2(\xi,\eta) d\xi^2 + d\eta^2 \\ h(\xi,\eta) &= 1 - \eta/R(\xi) \end{aligned} \tag{28}$$

with $R(\xi)$ being the radius of curvature which is shown positive in Fig. 33.

To obtain an approximate incompressible set of equations prototypic of the compressible case, the thin jet limit is considered. The characteristic jet thickness is shown in Fig. 33, where the jet boundary is denoted as $\eta = \tau b(\xi)$. The quantity τ thus represents a characteristic slope of the jet free boundaries

SC79 7137

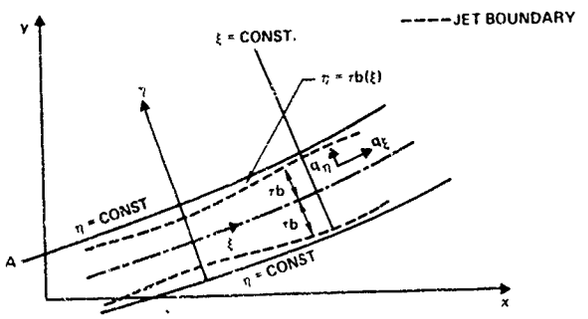

Fig. 33 Section of jet and curvilinear coordinate system.

which is of the same order as the jet thickness in units of its radius of curvature.

We now define a thin jet limit

$$t \to 0,\ \xi, \eta^* = \eta/\tau \text{ fixed} \tag{29}$$

where the boundary layer coordinate η^* is introducted to keep the jet slip lines in view in the limit process. In (29), the appropriate representations to yield a nontrivial structure are

$$\frac{q_\xi(\xi,\eta;\tau)}{U} = \frac{1}{\sqrt{\tau}} u_0(\xi,\eta^*) + \sqrt{\tau}\, u_1(\xi,\eta^*) + \cdots \tag{30a}$$

$$\frac{q_\eta}{U} = \sqrt{\tau}\, v_0 + \tau^{3/2} v_1 + \cdots \tag{30b}$$

$$\frac{p}{\rho U^2} = p_0 + \tau p_1 + \cdots \tag{30c}$$

where U is some typical freestream velocity. The orders were selected to give the "richest" possible set of equations and, consistent with this, produce forcing terms in the equations for the second order quantities. These orders are consistent with the massless momentum source mode of Spence[1].

Substitution of (30) in (27) and equating like orders gives the following equations for the approximate quantities:

$$\left.\begin{aligned} &\frac{\partial u_0}{\partial \xi} + \frac{\partial v_0}{\partial \eta^*} = 0 && \text{(31a)}\\ &u_0 \frac{\partial u_0}{\partial \xi} + v_0 \frac{\partial u_0}{\partial \eta^*} = 0 && \text{(31b)}\\ &\frac{u_0^2}{R(\xi)} = -\frac{\partial p_0}{\partial \eta^*} && \text{(31c)} \end{aligned}\right\}$$

$$\frac{\partial u_1}{\partial \xi} + \frac{\partial v_1}{\partial \eta^*} = \frac{1}{R}\frac{\partial}{\partial \eta^*}(\eta^* v_0) \qquad (32a)$$

$$u_0 \frac{\partial u_1}{\partial \xi} + v_0 \frac{\partial u_1}{\partial \eta^*} + \frac{\partial u_0}{\partial \xi} u_1 + \frac{\partial u_0}{\partial \eta^*} v_1 = \frac{u_0 v_0}{R} - \frac{\eta^*}{R} u_0 \frac{\partial u_0}{\partial \xi} - \frac{\partial p_0}{\partial \xi} \qquad (32b)$$

$$\frac{2u_0 u_1}{R} + \frac{\partial p_1}{\partial \eta^*} = - u_0 \frac{\partial v_0}{\partial \xi} - v_0 \frac{\partial v_0}{\partial \eta^*} - \frac{u_0^2 \eta^*}{R^2} \quad . \qquad (32c)$$

The appropriate boundary conditions involve statements regarding the fact that the jet boundaries are streamlines and that the static pressure is continuous across the slip lines. The upper and lower slip lines S_u and $S_\ell = 0$ are given by

$$S_u = \eta - \tau b_0(\xi) - \tau^2 b_1(\xi) = 0$$

$$S_\ell = \eta + \tau b_0(\xi) + \tau^2 b_1(\xi) = 0$$

where symmetry has been assumed to leading order.

Based on the foregoing discussion, the condition that jet boundaries S are streamlines is

$$\vec{q} \cdot \nabla S = 0$$

where $\vec{q} = (q_\xi, q_\eta)$. Substitution of the expansions (30) into this relation gives:

$$v_0(\xi, b_0) = b_0'(\xi)\, u_0(\xi, b_0) \qquad (33a)$$

$$v_0(\xi, -b_0) = -b_0'(\xi)\, u_0(\xi, -b_0) \qquad (33b)$$

$$v_1(\xi,b_0) = \frac{v_0(\xi,b_0)b_0}{R} + b_1 b_0' \frac{\partial u_0}{\partial \eta^*}(\xi,b_0)\ (\xi,b_0) + u_1(\xi,b_0)b_0'$$
$$- b_1 \frac{\partial v_0}{\partial \eta^*}(\xi,b_0) + b_1 u_0(\xi,b_0) \qquad (33c)$$

$$v_1(\xi,-b_0) = -\frac{v_0(\xi,-b_0)b_0}{R} + b_1 b_0' \frac{\partial u_0}{\partial \eta^*}(\xi,-b_0) - u_1(\xi,-b_0)b_0'$$
$$+ b_1 \frac{\partial v_0}{\partial \eta^*}(\xi,-b_0) - b_1 u_0(\xi,-b_0) \quad . \qquad (33d)$$

The other conditions involving continuity of pressure are:

$$p_0(\xi,b_0) = \frac{p_{ext}^{(u)}(\xi)}{\rho U^2} \equiv q_u(\xi) \qquad (34a)$$

$$p_1(\xi,b_0) = - b_1(\xi) \frac{\partial p_0}{\partial \eta^*}(\xi,b_0) \qquad (34b)$$

where we assume for the present argument that the external pressure field $p_{ext}^{(u)}$ is prescribed. Similar pressure conditions hold for the lower slip line boundary. If δ is a characteristic flow deflection angle of the order to the airfoil thickness or angle of attack, then $\tau << \delta$ has also been implicitly assumed.

Solutions

First Order Theory

We introduce the zeroth order stream function given by

$$\frac{\partial \psi}{\partial \xi} = - v_0 \quad , \quad \frac{\partial \psi}{\partial \eta^*} = u_0$$

and employ the following transformation for the independent variables

$$(\xi,\eta^*) \rightarrow (\xi,\psi) \quad . \qquad (35)$$

Under (35), the differential operators map as follows:

$$\frac{\partial}{\partial \xi} = \frac{\partial}{\partial \xi} - v_0 \frac{\partial}{\partial \psi}$$

$$\frac{\partial}{\partial \eta^*} = u_0 \frac{\partial}{\partial \psi}$$

and Eqs. (31) become

$$\frac{\partial u_0}{\partial \xi} - v_0 \frac{\partial u_0}{\partial \psi} + u_0 \frac{\partial v_0}{\partial \psi} = 0 \tag{36a}$$

$$\frac{\partial u_0}{\partial \xi} = 0 \tag{36b}$$

$$\frac{u_0}{R} = -\frac{\partial p}{\partial \psi} \quad . \tag{36c}$$

The general solution for Eqs. (36) is

$$u_0 = u_0(\psi) \tag{37a}$$

$$p_0 = k(\xi) - \frac{1}{R(\xi)} \int_0^{\psi} u_0(\psi')\, d\psi' \tag{37b}$$

$$v_0(\xi,\psi) = b'(\xi)\, u_0(\psi) \quad , \tag{37c}$$

$k(\xi)$ is the pressure on the centerline. The reference (centerline) condition ($v_0(\xi,0) = 0$) or the conditions at the edges of the jet (Eq. (33b)) show that $b_0' \equiv 0$ and $b_0 = 1$, if $b_0\,(0) = 1$. Thus, in terms of an arbitrary initial parallel flow profile $u_0 = f(\eta^*)$ at $\xi = 0$, we have

$$\psi = \int_0^{\eta^*} f(\tilde{\eta})\, d\tilde{\eta} \quad . \tag{38a}$$

Therefore, $u_0 = f(\eta^*(\psi))$, and (38b)

$$p_0(\xi,\psi) = k(\xi) - \frac{1}{R(\xi)} \int_0^{\psi} f\,(\eta^*(\psi))\, d\psi$$

$$= k(\xi) - \frac{1}{R} \int_0^{\eta^*} f^2 d\eta^* = q_u(\xi) + \frac{1}{R} \int_{\eta^*}^{1} f^2 d\eta^* \qquad (38c)$$

$$\left(k(\xi) = q_u + \frac{1}{R} \int_{\eta^*}^{1} f^2 d\eta^*\right) \quad .$$

Discussion

Equations (38) describe a parallel flow jet. The total jump in pressure across the jet from (38c) is

$$[p_0] = p_0(\xi,1) - p_0(\xi,-1) = -\frac{2}{R} \int_0^{1} f^2(\eta^*)\, d\eta^* \qquad (39)$$

which agrees with the Spence model. It should be noted that in contrast to the latter, no assumption regarding irrotationality is required to obtain (39), which is also in contrast to the results of previous workers. The radius of curvature of the jet is approximately R upstream of the trailing edge, which in turn is approximately given by that of the blown upper surface. Downstream of the trailing edge, R is determined from applying (39) to the determination of the flow outside of the jet. Upstream of the trailing edge, the wall pressure is determined by (39), since R is known and is given by

$$p(\xi,-1) = q_u(\xi) + \frac{2}{R} \int_0^{1} f^2(\eta^*)\, d\eta^* \quad . \qquad (40)$$

In Ref. 6, the appropriate second order theory corresponding to the expansions (30) are derived. Also indicated are various nonuniformities that can occur, such as those near the trailing edge. These reveal the need for other expansions in the neighborhood of the nonuniformities.

Also in Ref. 6, a small deflection specialization of the previous thin jet theory is considered. Therein, a systematic patching procedure is utilized, employing a "blending layer" at a vertical distance of the order of the slip line and airfoil deflection angle δ as $\delta \to 0$. The blending layer has been used

to validate the usual Taylor's series transfer of boundary conditions employed to define the outer flow. A treatment of similar blending layers is discussed in Cole[23] in connection with incompressible flows around unblown bodies of revolution.

3.2.2 Trailing Edge Behavior

Incompressible Flows

Defining the complex potential function as

$$F(z) = \phi(x,y) + i\psi(x,y)$$

where (x,y) is the local coordinate system shown in Fig. 34 and $z = x+iy$, the local "corner flow" solution to within a dimensional multiplicative constant in the lower external region A'OB where β and ν are the dividing streamline and trailing edge angles shown is given by

$$F = e^{-i\pi(\pi+\nu)/\beta}\, z^{\pi/\beta} \tag{41}$$

which implies that the square of the resultant velocity q is

$$|F'|^2 = q^2 \sim r^{2\left(\frac{\pi}{\beta} - 1\right)} \quad . \tag{41'}$$

The initial conditions for determination of the jet, which follow from the requirement that the pressure and flow angle be continuous across the dividing streamline near the trailing edge, were studied for incompressible flow. Referring to Fig. 34, with the dividing streamline denoted as OB, we signify the trailing edge angle as ν and the angle that OB makes with the upper surface AO as ω and that with the lower surface as β. The details of this discussion are given in Ref. 6 which shows that $\omega = \pi$ and $\beta < \pi$ is the only viable possibility if the stagnation pressure P_0^+ above AOB is greater than that below it, which is signified by P_0^-, where + and - superscripts signify conditions above and below the slip line AOB, respectively, and 0 refers to stagnation conditions. Denoting u as the flow speed along the slip line, Bernoulli implies

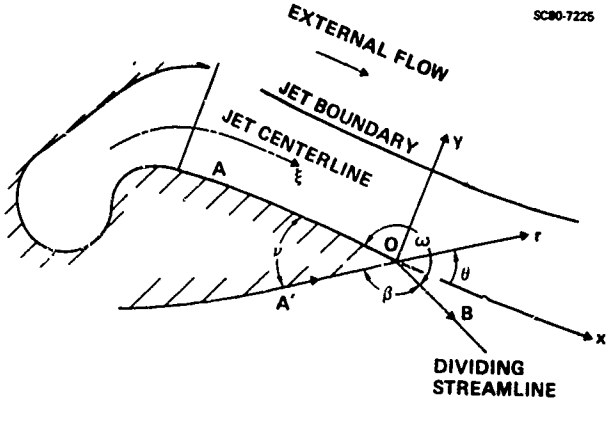

Fig. 34 Blown trailing edge formulation.

$$u^+ = \sqrt{\frac{2(P_0^+ - P_0^-)}{\rho}} \quad .$$

Here also, $u^- = 0$. These results quantify the slip.

If, on the other hand, $P_0^+ < P_0^-$, then $\omega < \pi$ and $\beta = \pi$ is the only possibility with

$$u^- = -\sqrt{\frac{2(P_0^- - P_0^+)}{\rho}} \quad ; \quad u^+ = 0 \quad .$$

For a hypothetical case in which $P_0^- \approx P_0^+$ in a real physical flow (fluctuating above and below equality), then a tri-stable configuration could evolve which would oscillate between configurations in which the dividing streamline is tangent to the upper and lower surface or bisects the trailing edge angle. Similar arguments have been applied to treat the conditions of the stream sheet at the trailing edge of unblown incompressible three-dimensional wings in Ref. 24.

Nonuniformities of Second Order Approximations

From (41), we find that another nonuniformity associated with second order solutions discussed in Ref. 6 is related to the following behavior

$$q_u' \sim r^{(2\pi/\beta)-3} \quad \text{as} \quad r \to 0$$

where, we distinguish the following possibilities as $\xi \to \xi_{TE}$:

(i) $q_u' \to \infty$, $\beta > \frac{2\pi}{3}$ or $\nu < \frac{\pi}{3}$

(ii) $q_u' \to 0$, $\beta < \frac{2\pi}{3}$ or $\nu > \frac{\pi}{3}$

(iii) q_u' finite $\neq 0$, $\beta = \frac{2\pi}{3}$ or $\nu = \frac{\pi}{3}$.

Case (i) is the most practical situation and will necessitate an inner solution for the transition layer to join the wall and free jet flows. This aspect is discussed in Ref. 6. For the jet structure considered here, we briefly investigate the vorticity which can be shown to be given by

$\omega = \tau^{-3/2}\omega_0 + \tau^{-1/2}\omega_1 + \cdots$, where as an illustration, if $u_0 = C$, then,

$$\omega_0 = \frac{\partial u_0}{\partial \eta^*} = 0$$

$$\omega_1 = \frac{\partial u_1}{\partial \eta^*} - \frac{u_0}{R} = -\frac{C}{R(0)} = \text{constant} \neq 0 \quad .$$

Because of the constant initial velocity profile, a non-zero vorticity is introduced by the body curvature. By contrast, a potential vortex over a circular cylindrical surface would have had a linear initial profile to produce an irrotational flow. Note for arbitrary initial profiles, $u_0(0,\eta^*) = f(\eta^*)$ and thus, $\omega_0 = f'(\eta^*) \neq 0$.

Compressible Trailing Edges

Consider again the configuration of Fig. 34. Here we analyze first the case where

$$P_0^+ > P_0^- \quad .$$

With the usual isentropic relation

$$\frac{P^+}{P_0^+} = \left[1 + \frac{\gamma-1}{2} M^2\right]^{\frac{-\gamma}{\gamma-1}} \quad , \quad (P^+ = \text{static pressure on upper side}) \quad ,$$

the local Mach number, M, can adjust in a continuous way, so that the flow recompresses smoothly from B to 0. At 0, M is single valued = M_1 and adjusts itself such that the static pressure P^+ equals P_0^-, in accord with the isentropic relation, assuming that the flow stagnates at 0 on the lower side. The only way this can be realized is with the $\omega > \pi$ and $\beta < \pi$ arrangement. In some respects the configuration resembles flow over a solid wall expansion corner. This gives rise to an expansion fan interacting with a sonic line from the corner. If the solid configuration were representative of this flow with the free boundary slip

line, compression waves would reflect off the sonic line and form a shock envelope which would be necessary to recompress the flow from an overexpanded value below the critical P_*^+ to the P_0^- level. Additional reflections can be produced from the upper slip line CD. This discontinuous transition leads to a multivalued pressure at O. The continuous and discontinuous processes are illustrated schematically in Figs. 35b and 35c, respectively. In Fig. 35b, the recompression takes place on the line BO. In Fig. 35c it occurs on OO'O"O"' signifying the confluence of multiple states at O. Here, the dashed line element O"O"' signifies a shock jump. Experimental data strongly suggests that as in the incompressible case, the configuration with $\omega = \pi$ and $\beta < \pi$ is the more probable situation. Presumably, a more rigorous argument to support this conjecture would rely on some sort of stability analysis. Specific criteria to determine whether the discontinuous or continuous configuration occurs in a given case is an open question that could benefit from further study.

For $P_0^+ = P_0^-$, the dividing streamline would again bisect the trailing edge, since the flow in the immediate vicinity would be incompressible and the reasoning in the previous section would apply. For the improbable case of $P_0^+ < P_0^-$, the configuration with $\omega < \pi$ and $\beta = \pi$ would be applicable as for the incompressible situation.

External Flow

For distances large compared to the jet width, the fine structure of the jet is important only insofar as it provides matching conditions to the irrotational "outer" flow field. In incompressible flow, this external outer flow can be determined by thin airfoil theory. At transonic speeds, small disturbance theory is appropriate for this region. Details of the asymptotic matching procedure have been discussed for incompressible flow in Ref. 6. Based on these developments and the earlier ones for thin jets in this paper, the boundary conditions for the outer flow in the incompressible and transonic cases for the jet flap and upper surface blowing are now indicated.

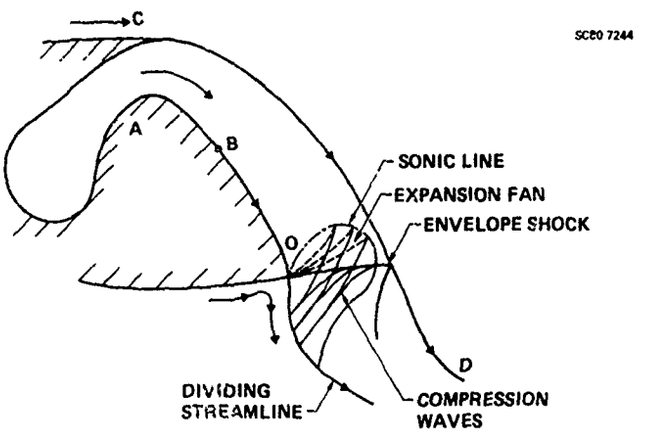

Fig. 35a Multivalued pressure at trailing edge. Configuration for dividing streamline.

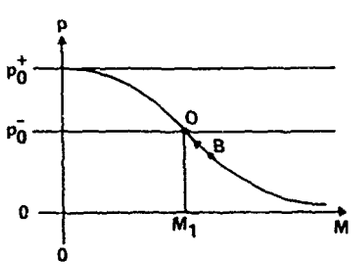

Fig. 35b Continuous isentropic compression.

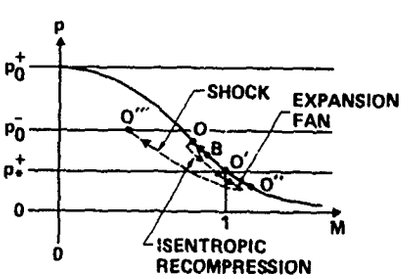

Fig. 35c Discontinuous configuration.

Jet Flap

Referring to Fig. 36, the equation of an airfoil can be given as

$$y = \delta f(x)$$

and the jet is

$$y = \delta g(x)$$

where δ is the thickness ratio of the airfoil, and f is the upper or lower surface and involves the angle of attack which is assumed to be of the same order of δ. Considering a small disturbance approximation, we obtain

$$R^{-1} = \frac{\frac{d^2y}{dx^2}}{\left[1 + \left(\frac{dy}{dx}\right)^2\right]^{3/2}} = \frac{\delta g''}{[1 + \delta^2 g'^2]^{3/2}} \triangleq \delta g''(x) \quad .$$

Letting the "outer" expansion pressure coefficient be represented as

$$\frac{P - P_\infty}{\rho U_\infty^2} = \delta p(x,y) + \cdots$$

then by virtue of a generalization of (39)

$$[p(x,0)] = - C_j g''(x) = - 2[\phi_x] \tag{42}$$

where

$$C_j \equiv \left(\rho \int_{-\tau}^{\tau} q_\xi^2 d\eta\right) / \rho U_\infty^2 = O(1) \tag{43a}$$

and ϕ is a perturbation potential.

Equation (42) is the relation used in conjunction with the jet tangency boundary condition

SC80 7187

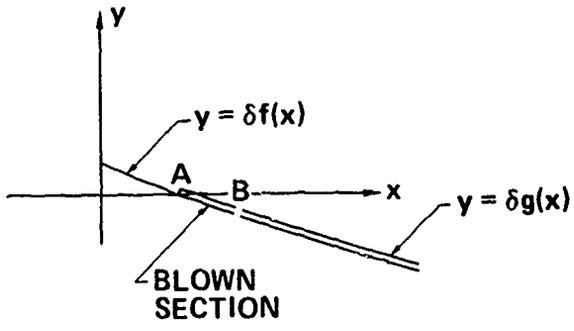

Fig. 36 Configuration for outer USB problem.

$$\phi_y(x,0) = g'(x) \qquad (43b)$$

and the airfoil boundary conditions to determine the external flow field. These relations coincide with the relations derived by Spence. They can be generalized for transonic flow by placing the ρ inside the integrand in (43a).

Upper Surface Blowing

To treat conditions on the blown part of the airfoil, Eq. (42) can be applied by approximating the radius R by $(f'')^{-1}$ to obtain the wall pressures, and by using the airfoil and jet boundary conditions to determine the upper slip line jet pressures.

From the thin jet theory derived earlier, it can be seen that rotational flow produces the same pressure jumps across the jet in the dominant approximation as the irrotational Spence models. Correspondingly, it can be shown that to within factors involving the density, qualitatively similar results are obtained for transonic flow. Another important aspect of the asymptotic representations derived here is that they lead to higher approximations for the structure of the jet and external flow which can be systematically obtained. Finally, the analytical solutions described above in Ref. 6 allow the systematic assessment of the effects of initial vorticity and skewness which are inaccessible to other theories.

3.2.3 Results and Discussion for Transonic Upper Surface Blowing

A successive line overrelaxation (SLOR) scheme within a Karman Guderley framework has been used to compute the flow field over an upper surface blown airfoil. On the blown portion, the jump conditions across the jet are determined by the asymptotic results given in previous sections, i.e., Eqs. (42) and (43b). Providing that the region is not too close to the jet exit or trailing edge, the streamwise gradients can be neglected in the entropy and velocity component parallel to the wall. Away from these regions, the pressure gradient perpendicular to the streamlines is balanced by centrifugal force. For the region near the jet exit, these assumptions become invalid. Here, the scale of

the gradients in the streamwise direction becomes important, principally due to the influence of wave interactions with the slip line. Similar fine structures occur near the trailing edge where the flow can stagnate on the unblown side, depending on the ratio of the stagnation values above and below the dividing streamline. For incompressible flow, the previous sections have discussed the tri-stable equilibrium at the trailing edge corresponding to the value of the stagnation pressure ratio, which leads to the dividing streamline leaving tangent to the upper surface if this is greater than unity. Consistent with the previous discussion, the appropriate generalization to transonic flow was assumed also to be this arrangement for a single valued pressure without a shock in that location. This assumption has been altered to assess the sensitivity of the flow to the dividing streamline angle. In this connection, surface pressures for the dividing streamline bisecting the trailing edge angle (as it would in incompressible flow) were compared with those for the tangent arrangement. Based on these studies, significant differences are anticipated only for large incidences and trailing edge angles.

Typical results obtained from the computational model are shown in Fig. 37 in which the flow over a thick airfoil designed at Rockwell's Columbus Aircraft Division (CAD) was analyzed with the SLOR code. Here, the pressures for various values of the blowing coefficient, C_j, are compared with those for the unblown case at a freestream Mach number $M_\infty = 0.703$ and angle of attack $\alpha = 0°$. Substantial lift augmentation is evident for blowing. Also evident is the associated rearward motion of the shock with increased blowing and sectional loading as if the incidence is increased.

Further parametric studies are provided in Fig. 38 which indicate the effect of parallel displacement of the slot x_j (in units of the chord), on the chordwise pressures. Three positions of the slot $x_j = 0.5$, 0.65, and 0.8 are shown. No systematic trend in the blown pressures is exhibited on this airfoil with downstream slot movement for fixed C_j. Evident, however, is a slight intensification of the terminating shock with slot downstream motion although its position remains unaltered. Despite the limitations of the model to describe

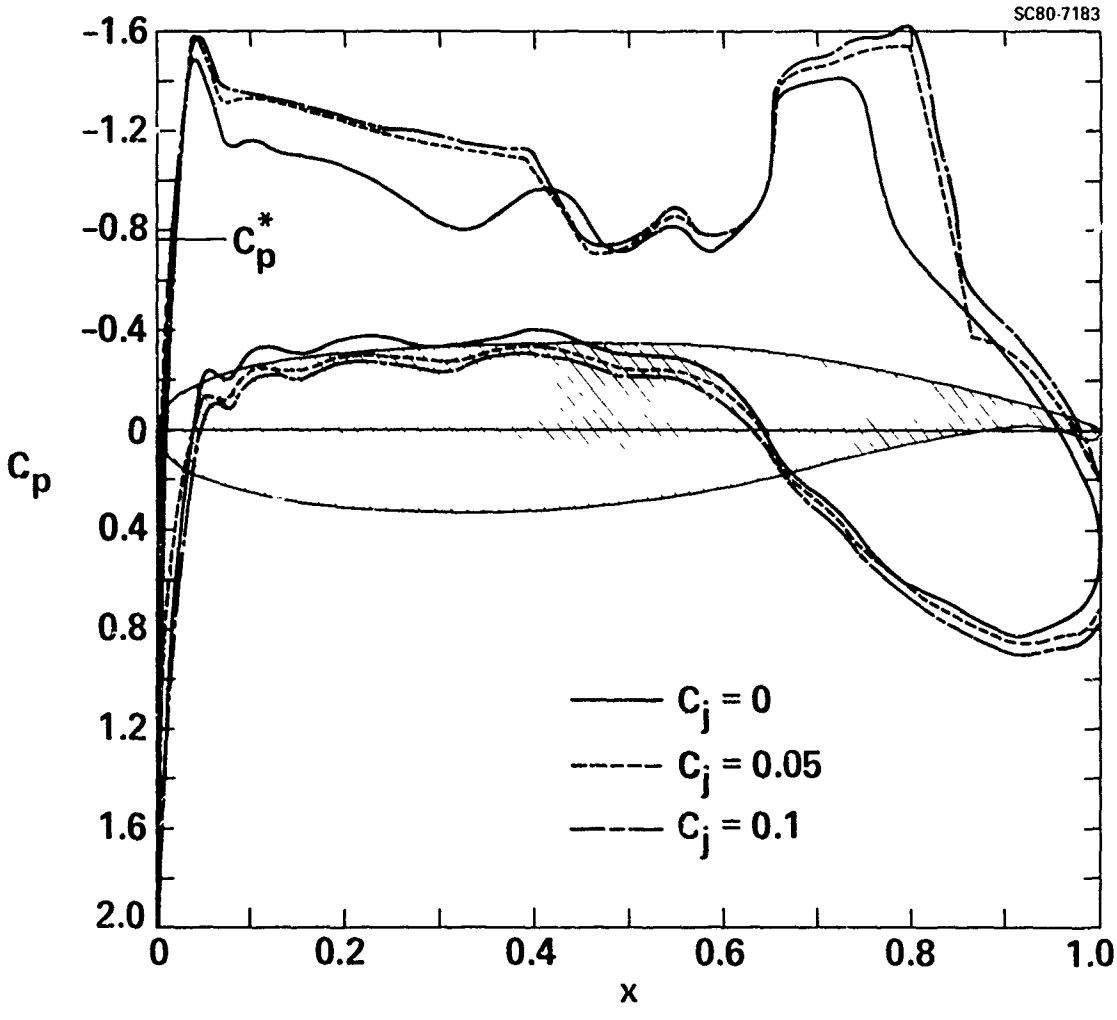

Fig. 37 Effect of blowing coefficient, (C_j), variations on chordwise pressures for CAD USB supercritical airfoil, $M_\infty = 0.703$, $\alpha = 0°$, (slot location at 65% chord).

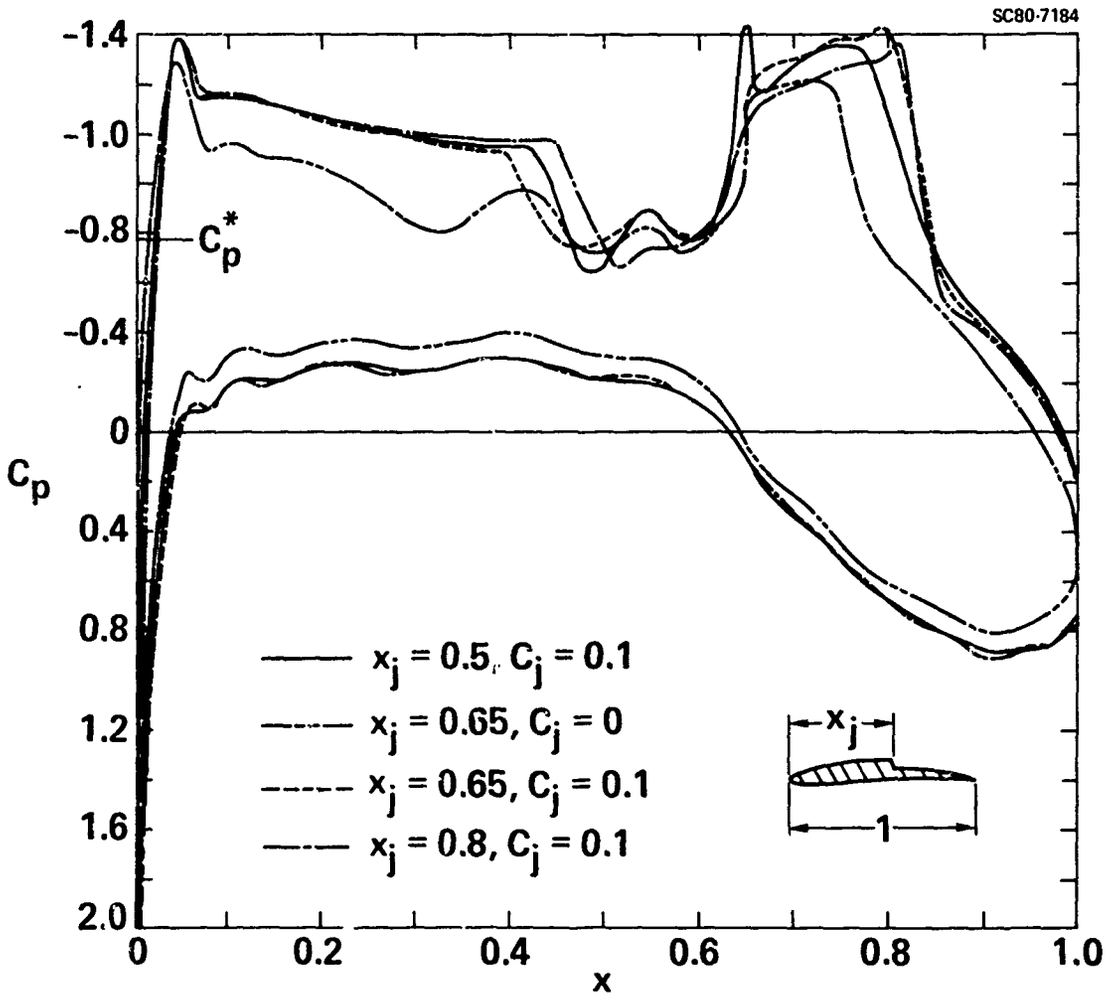

Fig. 38 Effect of slot location x_j in units of chord on chordwise pressures for CAD USB supercritical airfoil, $M_\infty = 0.703$, $\alpha = 0°$.

the fine structure of the jet exit region, a small suction peak which has been observed in experiments is exhibited in this vicinity for x_j = 0.5. In Fig. 39, the corresponding increase in lift coefficient C_L with slot downstream movement is also shown, as is the increase in the size of the supersonic region.

In Fig. 40, the increase of lift with blowing coefficient as well as size of the supersonic region is quantified.

Tests of the adequacy of the foregoing model to simulate realistic transonic USB airfoil flows have been inhibited by the lack of suitable experimental data. Information exists only for highly three-dimensional configurations, large thickness, or incidence in ranges beyond the validity of the assumptions of small disturbance theory. Another restriction is the unavailability of the associated geometric data and flow diagnostics accompanying the tests. The results of Yoshihara[25] and his coworkers were useful in this connection and allowed us to compare the jet flap specialized version of the USB theory with the data in Ref. 21. For the simulations described in this paper, tests performed by N.C. Freeman at NPL on a USB modified 6% thick RAE 102 airfoil, and described in Ref. 26, appear to have the most suitable results for comparison at present. Unfortunately, the angle of attack associated with the NPL data is 6°, which is marginal for the application of a small disturbance model.

Figure 41 indicates comparisons of chordwise pressures for various values of C_j. Also shown are schlierens, indicating the associated flow field structure. Turning to the C_j=0 results (Part (a)), massive shock induced separation is indicated and is apparently initiated at the downstream limb of the lambda shock on the upper surface. This is reflected in the classical erosion of the suction plateau and is responsible for the indicated disagreement between the inviscid computational results and the data. For these tests, nominal tangential blowing with a slot height of 0.07% of the chord was used. The slot location is 15% downstream of the nose. The Mach number M immediately above the slip line at the slot is approximately 1.29 for both C_j's indicated. For C_j=0.017, the slot Mach number M_e has been estimated as 1.79 and for C_j=0.048, $M_e \approx 2.36$.

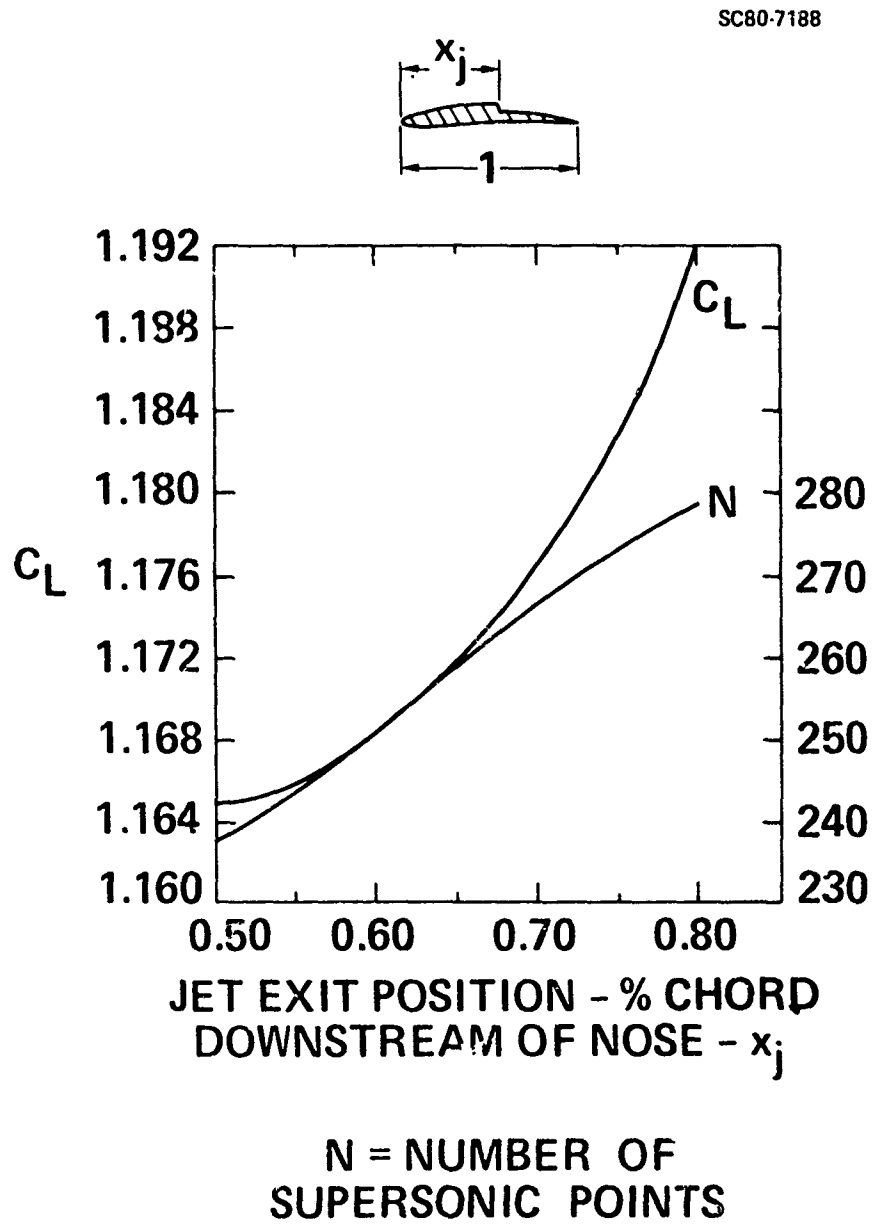

Fig. 39 Behavior of C_l and criticality as a function of extent of blowing, CAD USB airfoil, C_j = 0.1, M_∞ = 0.703, α = 0°, N = number of supersonic points.

SC80-7189

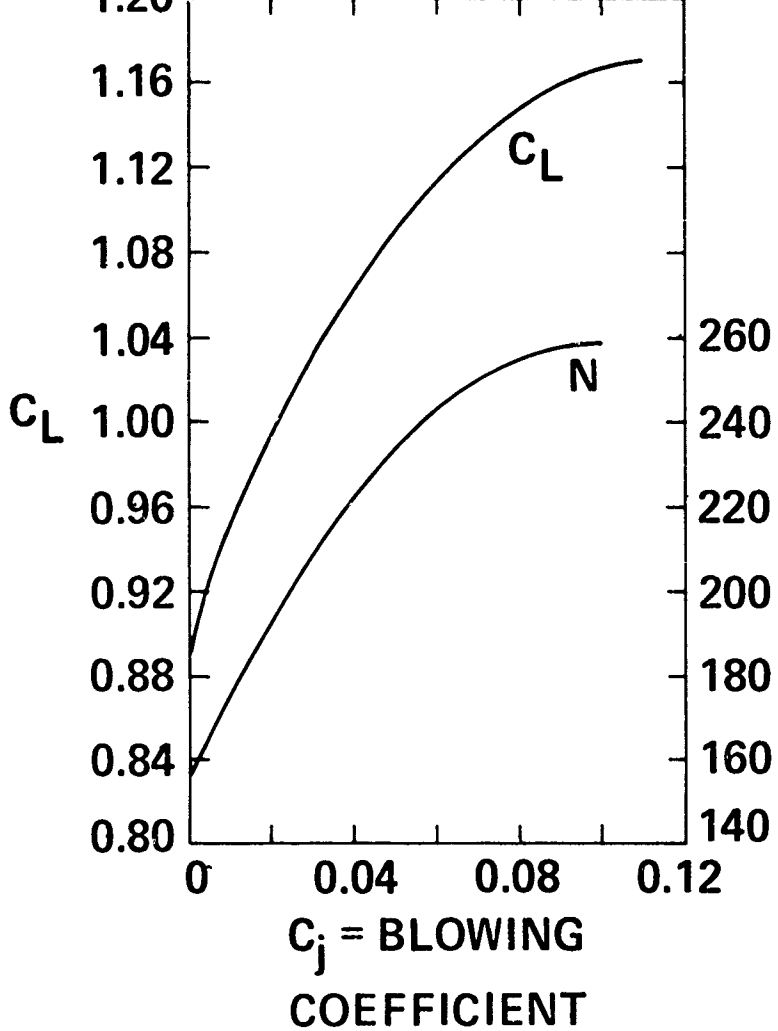

Fig. 40 Variation of C_L and criticality of CAD USB airfoil with blowing coefficient, $M_\infty = 0.703$, $\alpha = 0°$, $x_j = 0.65$, N = number of supersonic points.

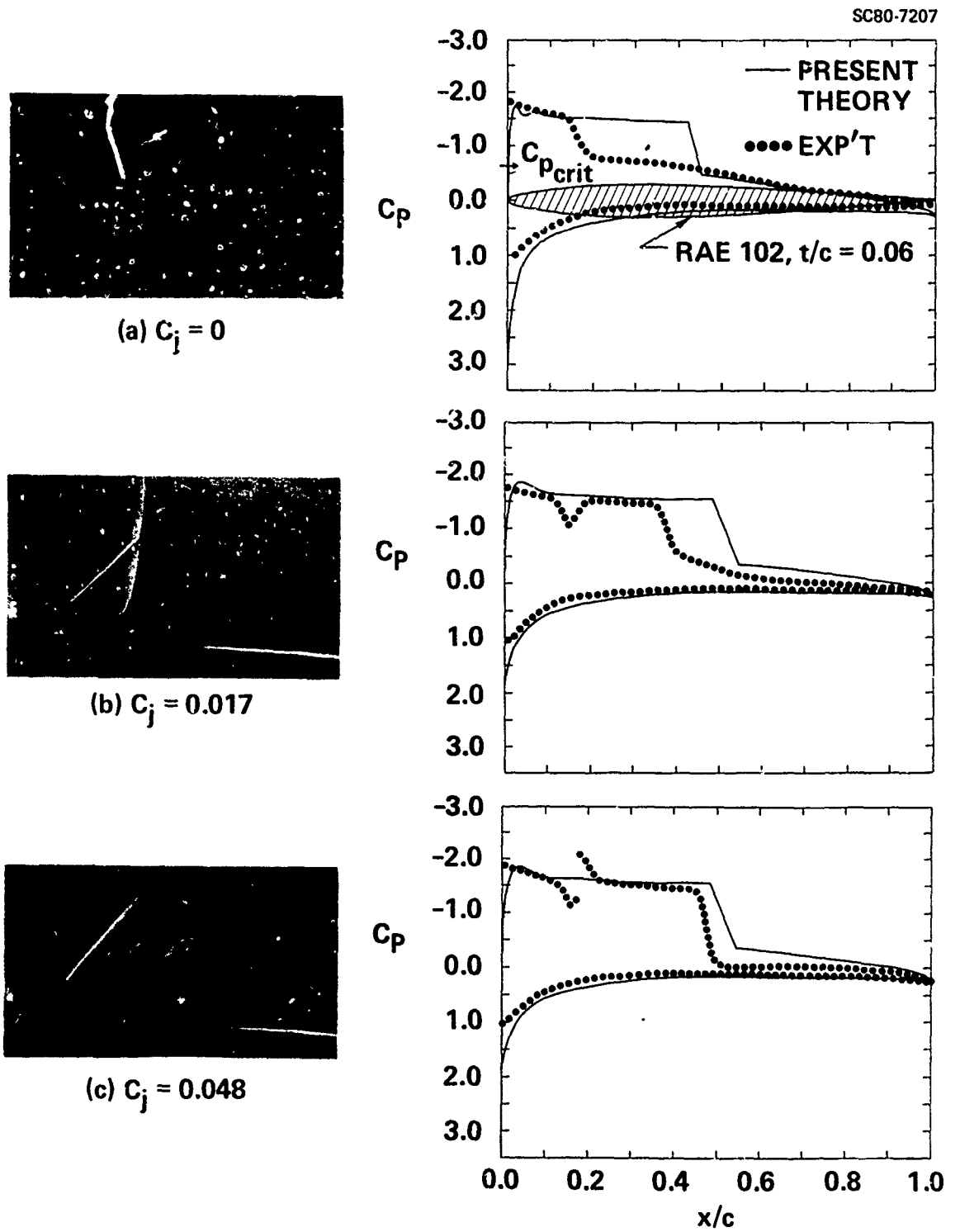

Fig. 41 Comparison of USB theory of this report with NPL tests of Freeman (Ref. 26), $M_\infty = 0.75$, $\alpha = 6°$, c = chord, t = maximum thickness.

Comparison between theory and experiment in Part (b) of Fig. 41 indicates reduced discrepancies on the upper surface associated with the limited separation. In Part (c), the agreement is correspondingly further improved.

To achieve adequate realism, it is important to discuss factors responsible for the disagreements. One feature not captured by the USB simulation is the pressure spike at the slot location. Based on the slot size, the streamwise scale for this phenomenon is at least an order of magnitude greater than the characteristic wavelength of a Mach diamond pattern in the wall jet. These fluctuations may not be resolvable with conventional pressure tap arrangements for the thin slot employed in the tests. If a rough model of a coflowing inviscid supersonic wall jet over a flat plate is used to describe the flow near the slot, the approach to a final steady state may be damped oscillatory or monotone, depending on whether the reflection coefficient R which is given by

$$R = \frac{\lambda-1}{\lambda+1} \tag{44}$$

where

$$\lambda = M_e^2\beta/M^2\beta_e \quad , \quad \beta = \sqrt{M^2 - 1} \quad , \quad \beta_e + \sqrt{M_e^2 - 1}$$

is respectively positive or negative.

The relaxation length L to achieve the downstream pressure in units of the exit height is of the order of ℓn R, which can be approximately 5 to 50 in the present case, depending on the accuracy of the estimate for M_e. Note in this connection that

$$R < 0 \text{ for } 1 < M < \frac{M_e^2}{\beta_e} \text{ , and } M_e < M < \infty$$

$$R > 0 \text{ for } \frac{M_e^2}{\beta_e} < M < M_e \quad .$$

For the submerged case, $R \to 1$, ($M_e \gg M$), and the Prandtl periodic pattern is obtained, with no radiation of energy to the external flow.

These facts suggest that one factor that may be responsible for the observed spike is the internal decay process in the jet. If transonic effects and wall curvature are accounted for, the presence of "ballooning" and throats in the jet may also be contributory. We have discussed such phenomena in connection with submerged transonic wall jets in Ref. 5 and earlier in this report and have reported analogous results for the coflowing case in previous sections. Selection rules in terms of M_e and M for the existence of throats in the jet near field have also been given previously and are based on an integral form of the Karman Guderley equation. A rough sketch of the wave system that could explain the spikes in Figs. 41b and 41c is shown in Fig. 42. Yet another phenomenon that would have a similar wave pattern would be a slight upward motion of the jet due to viscous mixing or a misalignment with the surface tangent at point A.

Turning now to the discrepancy of the values shown on the rear surface (downstream of 0.5c) in Fig. 41c, we note that in spite of the obvious elimination of separation, a thick viscous wall jet is present. Downstream diffusion will affect the application of the Spence relation on the blown portion as well as the shock jump. In view of the wall jet thickness shown on the schlierens, this factor appears to be more significant than shock obliqueness at its foot. A near term refinement being implemented employs a coupled inviscid-viscous model which uses second order boundary layer corrections to the Spence boundary conditions accounting for axial gradients of the displacement and momentum thickness. Once these refinements are incorporated, systematic optimization among separation suppression, wave drag minimization, and supercirculation control will be possible. It is envisioned that the design techniques contained in Refs. 27-29 will augment this capability by providing methods to modulate shock formation in concert with the blowing effects.

SC80-7223

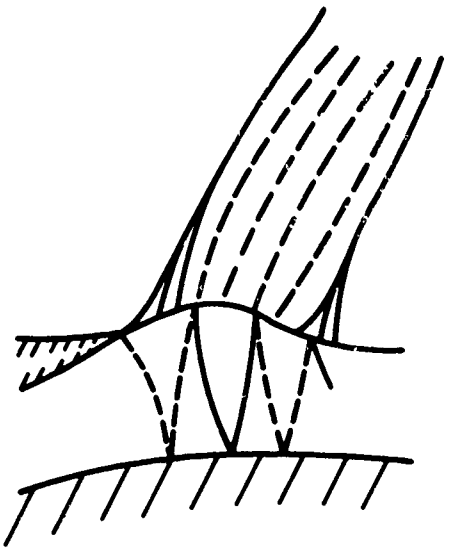

Fig. 42 Inviscid wave pattern associated with slip line ballooning and jet throat formation.

4.0 VISCOUS EFFECTS

4.1 Preliminary Remarks

A schematic of the blown airfoil is shown in Fig. 43, where the shaded region indicates the boundary layer and wake, P is the stagnation point, and S is the slot location. In the research performed, a computational model has been developed to treat the wall jet, wakes, and boundary layers, which without loss of generality have been assumed laminar. For treatment of the latter, integral methods have been discarded due to their highly empirical nature, lack of consistency, and questionable applicability to blowing cases. In fact, despite the unavailability of general accuracy criteria, it is well known that even for unblown incompressible decelerating laminar flows in adverse pressure gradients, integral methods such as those due to Pohlhausen and others[30-32] produce results that are increasingly inaccurate as the separation point is approached. For purposes of the present tangential injection study, this limitation is unacceptable. On the other hand, full elliptic Navier-Stokes solvers such as those employed by Diewert[33] have not been selected at this time because of their lengthy computational nature and associated need to resolve grid generation issues peculiar to the present blowing problem. By contrast, we believe that the most appropriate model is a zonal one, in which the inviscid region is treated by an iterative scheme such as Murman-Cole SLOR or any of the more modern techniques, and the viscous regions are treated by some parabolic solver such as Keller's box scheme.[34] A somewhat more sophisticated approach involving a parabolized or thin layer Navier-Stokes algorithm represents a future direction for refinement. The utilization of a finite difference approach for the viscous layers avoids the need for assumption of velocity profiles as in the integral methods. This is particularly crucial for tangential injection that carries with it the possibility of multiple extrema, overshoots, and exponential rather than algebraic decay of the wall jet velocity profile to the freestream levels.

Referring to Fig. 44, a viscous module has been developed to described the boundary layers in Regions (1'), (2'), (1), (2), and the blown wall jet (3). In

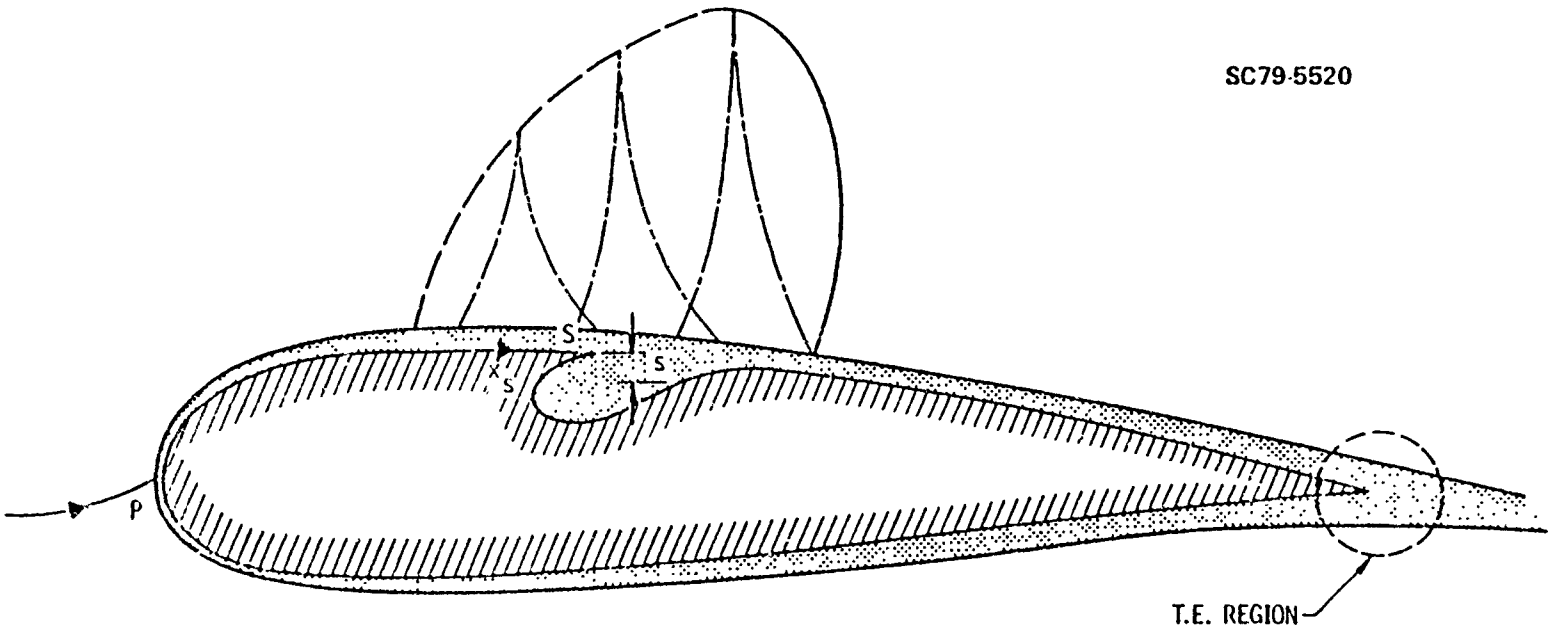

Fig. 43 Viscous transonic upper surface blowing (USB) problem.

SC80-9858

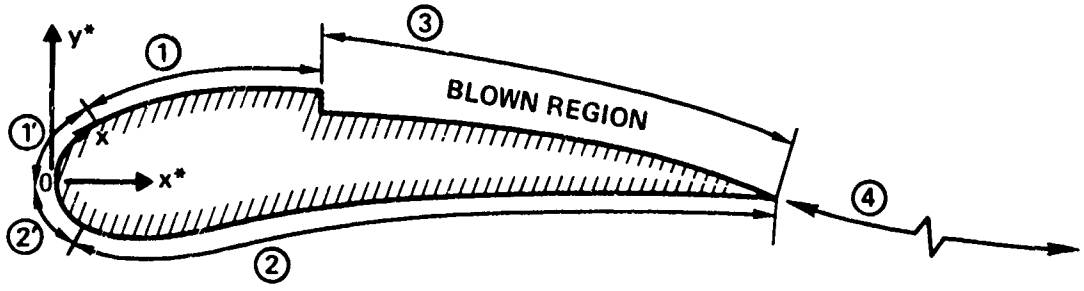

Fig. 44 Regions of consideration for USB airfoil.

a later section, preliminary results for a module for region (4) will be discussed. Zones (1') and (2') are in the vicinity of the nose and are especially important to treat properly in the small disturbance context of our effort. The correct synthesis and treatment of the small disturbance singularity near the stagnation point will be discussed and has important implications regarding the boundary layer development in (1') and (2'). Thus far, numerical investigations suggest that the precise flow details in (1') and (2') are, however, not decisive in their influence on the global structure of the field, in particular, the role of blowing in delaying transonic separation.

On this basis, a rough model for the nose region combining the essential features of incompressible stagnation point flow, and further downstream, small disturbance singular behavior, was implemented. More precise simulations involving asymptotic and computational matching of the aforementioned singular solution as an inner limit of the Karman Guderley outer flow and a full potential flow over a parabolic nose appropriate to finite curvature airfoils have been developed by K. Kusonose in a Ph.D. dissertation supervised by J.D. Cole.[35] This solution is appropriate for a more accurate description of the inviscid edge conditions of the boundary layer. A further refinement is to incorporate these boundary conditions in a compressible viscous stagnation point flow matching with the boundary layer.

4.2 Implementation and Results

By using the previously enumerated concepts, a laminar boundary layer module has been constructed based on a generalization to tangential blowing of the box method of Ref. 34. Results have been computed by coupling this element to the inviscid framework previously discussed to provide a blown boundary layer algorithm. Formulational details are given in the appendices. Specifically, Appendix A delineates a laminar framework, in which the normal coordinate is written as a Blasius like variable which is advantageous in resolving the steep gradients and treating the singular flow near the nose. Appendix B describes special procedures implemented at the nose that are required to properly interface with the small disturbance inviscid part of the flow. In Appendix C, a derivation of jump conditions across blown wakes according to matched asymptotic expansions

is given. These relations are of importance to future efforts on characterizing viscous modifications of the external flow.

Briefly, for the results to be discussed, a finite difference algorithm based on the compressible boundary layer equations was used. Furthermore, a unity Prandtl number, Chapman gas with constant density viscosity product across the boundary layer, and insulated wall was assumed. With these assumptions, an integral of the energy equation implies that the stagnation enthalpy in units of its value at the boundary layer edge, E, is a constant = 1 across this layer. The momentum equation is thereby decoupled. Thermodynamic variables such as the density in the layer can be calculated from the boundary layer assumption of constant pressure across the layer and E = 1. These observations lead to the following momentum equation for the normalized velocity f' in units of its boundary layer edge value:

$$(bf'')' + m_1 ff'' - m_2 f'^2 + m_{11} c = m_{10} \left[f' \frac{\partial f'}{\partial x} - f \frac{\partial f}{\partial x} \right] \qquad (1)$$

where the coefficients (defined in Appendix B) are related to the external pressure gradient, primes refer to partial differentiation with respect to ζ, a scaled Blasius coordinate in a direction perpendicular to the parallels to the airfoil. The quantity x refers to the coordinate along the parallels as shown in Fig. 44.

Figure 45 depicts a NACA 0012 airfoil, with a smoothed small disturbance SLOR chordwise pressure distribution on its upper surface for $M_\infty = 0.7$ and $\alpha = 3°$ as a basis of illustration; typical results, shown in Fig. 46, indicate the streamwise evolution of velocity profiles upstream of the slot and uncorrected for viscous interaction effects on the external flow field. Despite the rather severe adverse pressure gradients, particularly those associated with the nose singularity, and their significant influence on the source term in the momentum equations as the coefficients of the reduced form in the Blasius variables, the box scheme is robust enough to treat such variations. For the case at hand, the loss in fullness in the profile resulting from the adverse pressure gradient is evident. Associated decreasing wall shear stress is also apparent.

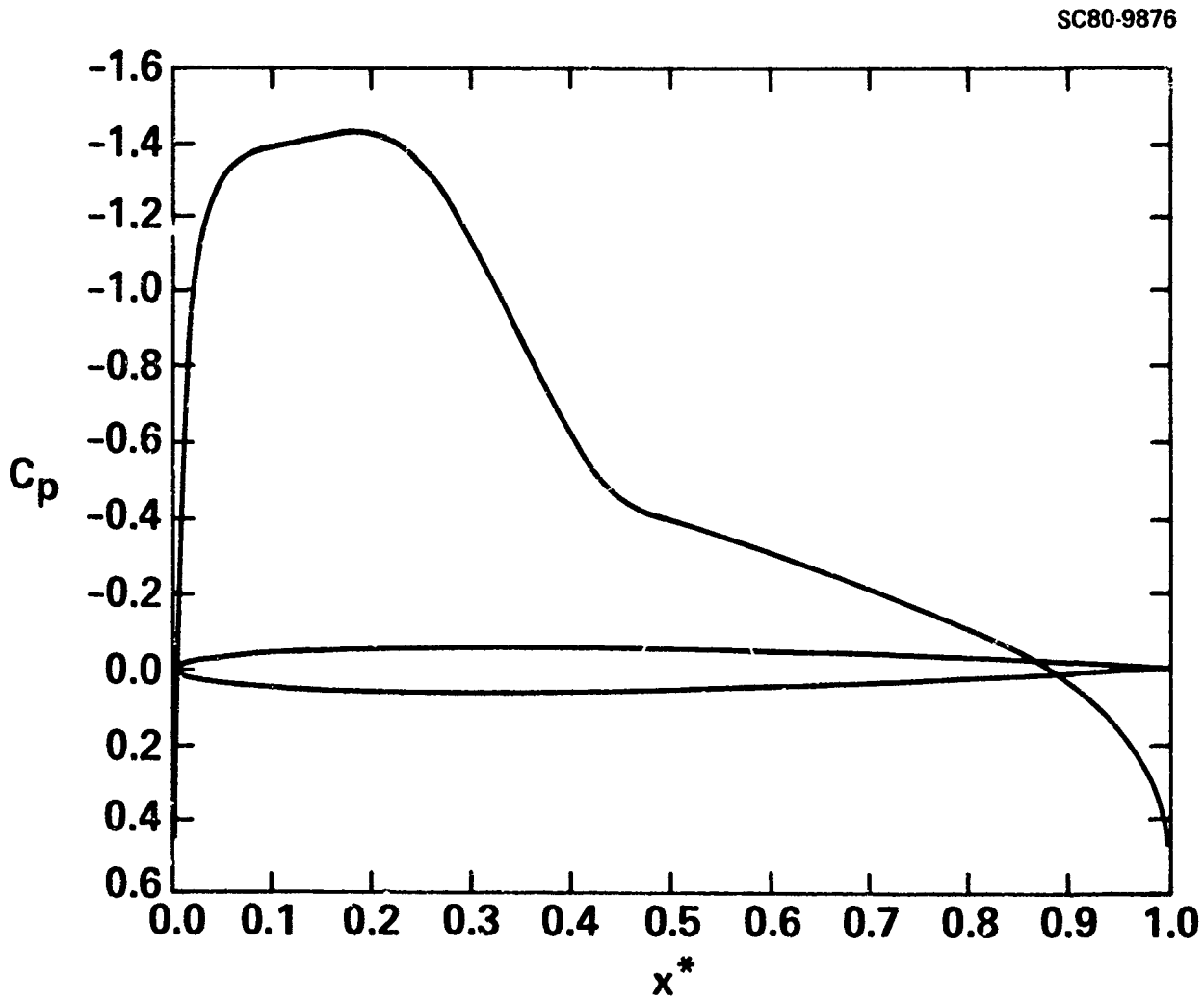

Fig. 45 Pressure distribution on upper surface of NACA 0012 airfoil, $M_\infty = 0.7$, $\alpha = 3°$.

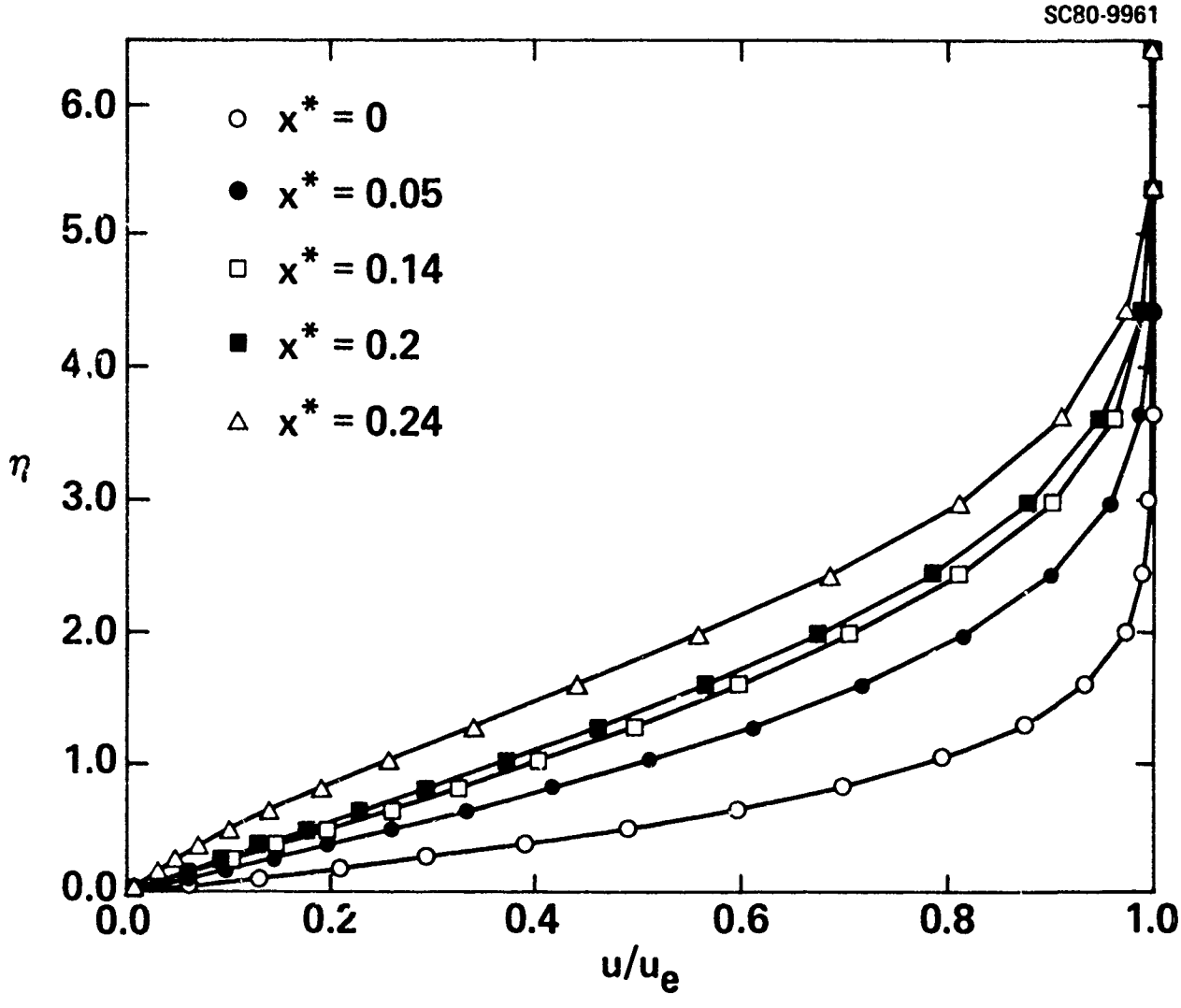

Fig. 46 Unblown streamwise profile development for case of Figure 45.

Regarding the influence of slot blowing, Fig. 47 shows evolution for the same airfoil of the profiles downstream of a slot located at $x^* = 0.2$ in which (x^*,y^*) refer hereinafter to Cartesian coordinates erected at the mean camber line in the usual way. For the examples selected, an initial parabolic slot profile was utilized, in which the velocity function at the slot station $x^* = x_s^*$ is given by

$$\frac{u}{u_e} = f'(x_s^*,\zeta^*) = -A(\zeta^*-\zeta_d)\zeta^* \quad , \quad 0 < \zeta^* < \zeta_d \tag{2a}$$

$$A = \frac{4\left(\frac{u}{u_e}\right)_{max}}{\zeta_d^2} \quad , \quad \zeta^* = \zeta + \zeta_d$$

and for the range of ζ^* above the slot lip,

$$f'(x_s^*+,\zeta^*) = f'(x_s^*-,\zeta^*) \quad , \quad \zeta_d < \zeta^* < \infty \tag{2b}$$

where the solution which had been marched from upstream to the slot location is assumed to have a continuous velocity component at the slot (excluding the pathological case of shocks at the slot location).

From (2a),

$$f = -\frac{A\zeta^{*3}}{3} + A\zeta_d\frac{\zeta^{*2}}{2} \quad , \quad 0 < \zeta^* < \zeta_d \tag{3a}$$

$$f(\zeta_d) = \frac{A\zeta_d^3}{6} \quad . \tag{3b}$$

For more general slot profiles in which

$$f'(x_s^*,\zeta^*) = F'(\zeta^*) \quad , \quad 0 < \zeta^* < \zeta_d \quad ,$$

the blowing coefficient $= C_J = \frac{J}{\rho_\infty U^2 c}$, where J = momentum flux/unit span, c = chord is given by

SC80-9868

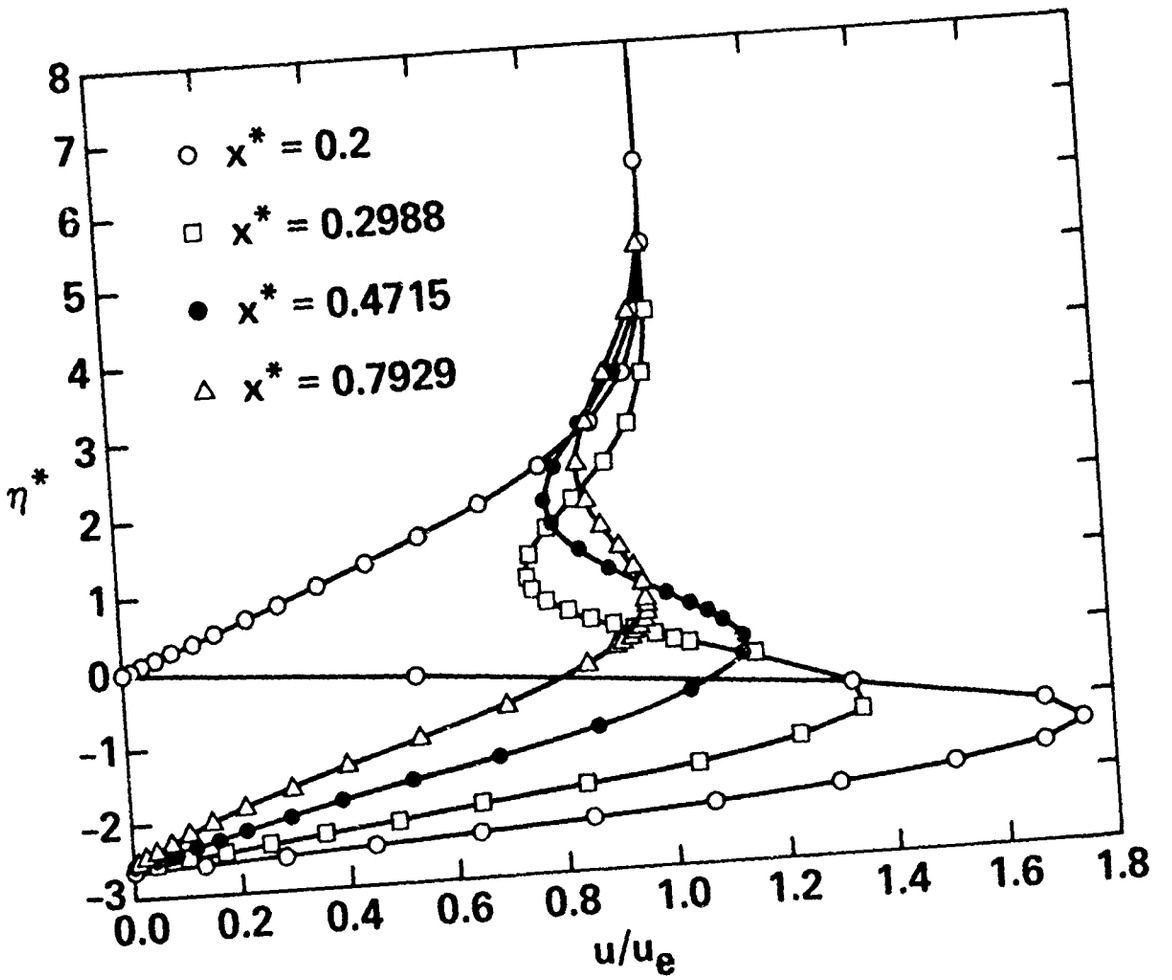

Fig. 47 Blown profiles A =1, ς_d = 2.65.

$$C_J = \sqrt{\frac{x^*_{sL}}{Re_\infty}} \int_0^{\zeta_d} F'^2(\zeta^*)d\zeta^* \quad , \tag{4}$$

where Re_∞ is the freestream Reynolds number based on the chord, and x^*_{sL} is the streamwise position of the slot in units of the chord. Actually, (4) is an approximation to within terms of $O(\delta^{2/3})$. In (4), the quantity ζ_d is given by:

$$\zeta_d = \frac{d}{c}\sqrt{\frac{\bar{\rho}}{\rho_e}\frac{Re_\infty}{x^*_s}} \tag{5}$$

where d is the dimensional slot height and $\bar{\rho}$ is the mean density across the slot.

For the example indicated in Fig. 45, the slot was located at 20% chord, very close to the onset of separation, which occurred at 27.6% chord for this case. It should also be noted that the location of the shock which had been slightly smoothed for purposes of initial checkout of the algorithm (which can handle non-smooth cases) is at about 23% chord. The characteristic diffusion of the profile associated with mixing of the jet is evident in the figure. More significant and not clearly indicated (but shown later), is the fact that the separation point has now been moved downstream to 79% chord. Other calculations show that with modest further increases in ζ_d, separation can be completely eliminated. (Note in this context that the peak velocity for (2a) is $A\zeta_d^2/4$.)

In Ref. 36 the corresponding profile development for an "underblown" case, where the peak is less than the freestream value, is discussed. Relaxation to a conventional profile occurs as previously. However, this blowing configuration actually results in premature separation, compared to the case of no blowing. This is indicated in Fig. 48 where the effect of blowing on the separation point location is shown. Despite the initially higher shear stress at the slot in the underblown case $\zeta_d = 1$, $A = 2$, the higher vorticity diffusion and lower overall momentum in the layer leads to earlier separation which can be seen as the leftmost solid circle in Fig. 48. This level should be related to the unblown result shown in dashed lines in the same plot. Moreover, the case $\zeta_d = 2.65$, $A = 1$, moves the separation point substantially downstream to almost 80% chord. Other cases are shown in Fig. 48, such as the one corresponding to

SC80-9874

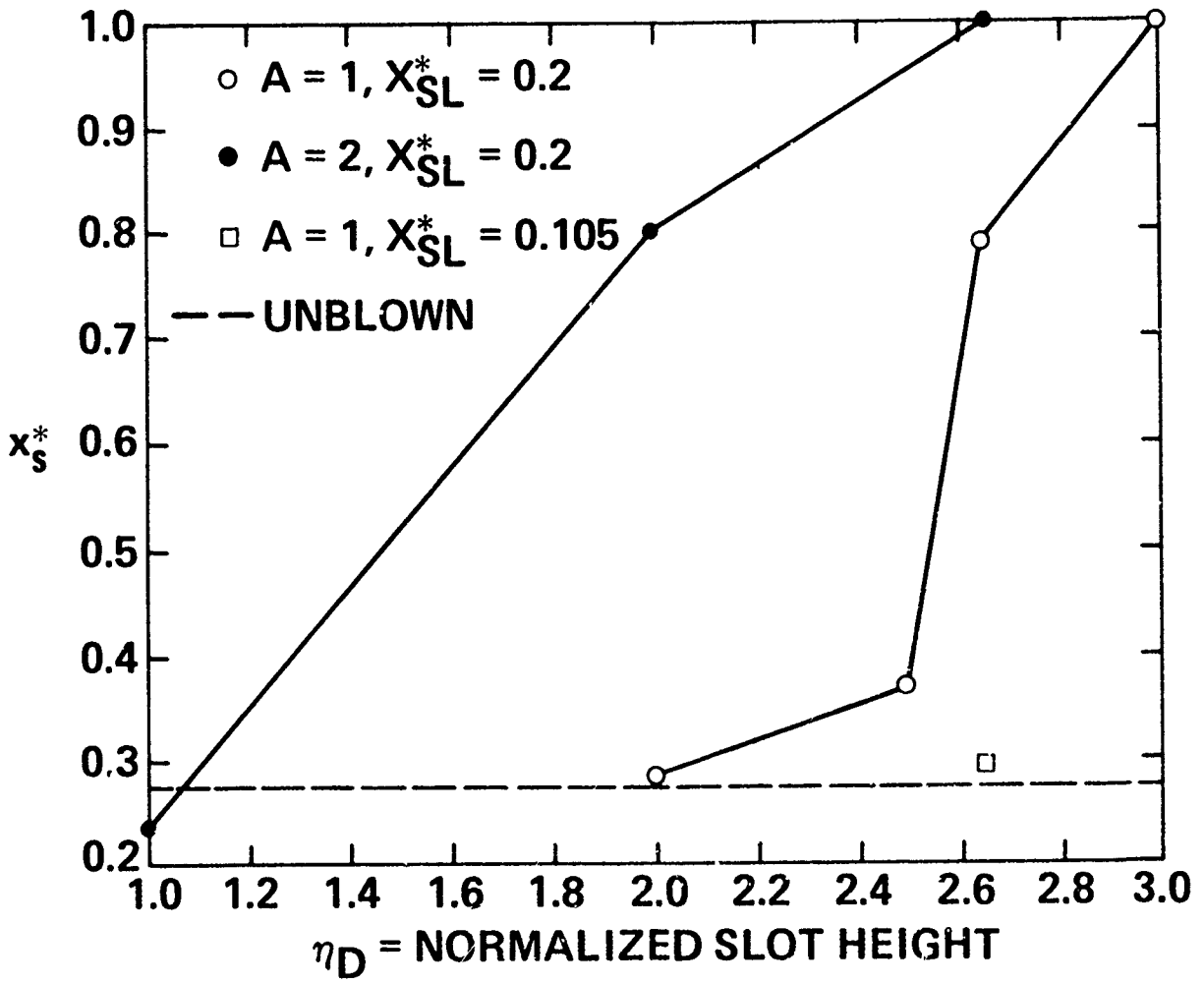

Fig. 48 Position of separation point x_s^*, with blowing - NACA 0012 airfoil, $M_\infty = 0.7$, $\alpha = 3°$.

the slot position at approximately 11% chord. This demonstrates the dramatic role of the slot location and upstream boundary layer thickness in delaying separation; where for the same slot height, the upstream slot location gives an almost trivial downstream movement of the separation location, in contrast to the potent effect of the downstream slot position.

The results of Fig. 48 can be replotted as in Fig. 49 to show the trends as a function of a momentum flux parameter which is proportional to C_j. By Eq. (3), $C_J = (x_{SL}/Re)^{1/2} A^2 \zeta_d^5/30$ for a parabolic profile. For the case at hand, according to Fig. 39, an $A^2\zeta_d^5 = 200$ represents a value sufficient to drive the separation point to the trailing edge. For $Re_\infty = 10^6$ and $\bar{\rho}/\rho_\infty = 1$, this implies that $C_J \approx 3 \times 10^{-3}$, a value that is surprisingly modest in view of the ease in which laminar boundary layers separate and the typical turbulent values of C_J associated with transonic experiments. These values which are betweeen 0.01 and 0.1 are selected to be large enough to provide significant supercirculation enhancements. Returning to the example calculated, Eq. (4) indicates that the slot height $d/c = 0.9 \times 10^{-3}$, corresponding to a $\zeta_d \approx 2.5$. For the limited number of cases run, there is a suggestion in Fig. 49 that the curves of Fig. 48 collapse to a single universal band of results. In view of the roles of the pressure gradient, and the multiple extrema in the velocity profile, this assertion must be regarded as tentative at best, pending more extensive parametric studies. What is significant, however, is that for the first time, the delay effect of tangential blowing on natural and shock induced separation over transonic airfoils has been inexpensively quantified.

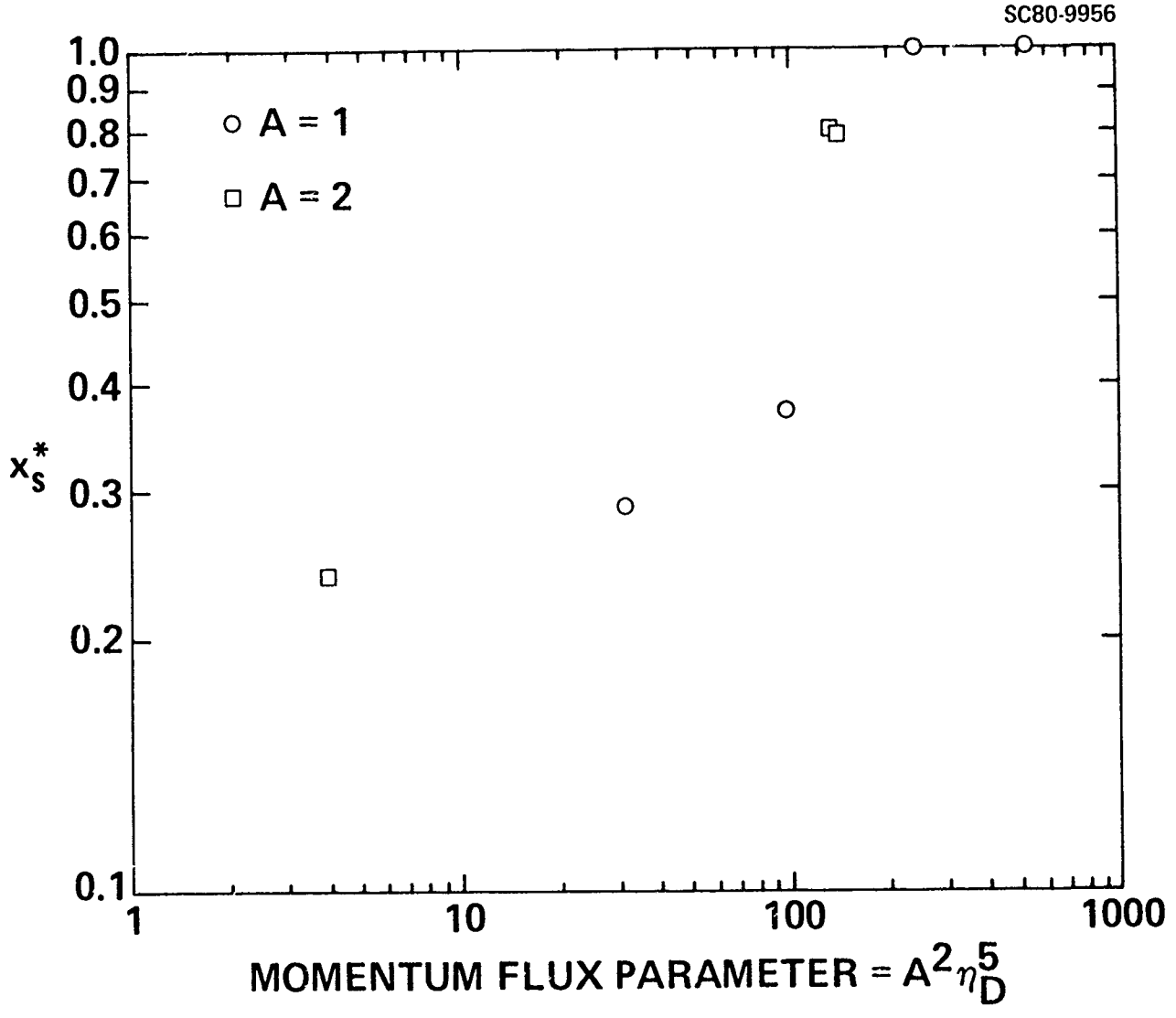

Fig. 49 Reduced plot of separation location x_s^* as a function of momentum flux parameter $A^2\zeta_d 5$.

5.0 WAKE STUDIES

5.1 Formulation

To obtain the wake structure, Eq. (1) of Section 4.2 is solved by using "initial" conditions at the trailing edge from the boundary layer solutions obtained with our parabolic solver upstream. In contrast to the no slip and asymptotic conditions required to complete the formulation over the airfoil, the wake requires the following conditions to be fulfilled:

$$\left.\begin{aligned} f'(x,\pm\infty) &= 1 \\ f(x,0) &= 0 \end{aligned}\right\} \quad x>1 \qquad \begin{aligned} &(1a) \\ &(1b) \end{aligned}$$

where x=1 is the location of the trailing edge.

Note that the zero argument in (1b) is a consequence of Prandtl's transposition theorem, where the boundary condition on the dividing streamline can be replaced by those at any other convenient location, e.g., ζ=0.

With the Box Scheme, Eq. (1) gives a three point boundary value problem for an inhomogeneous ordinary differential equation formulation based on the parabolic partial differential Eq. (1) of Section 4.2. With pivoting strategies to avoid singular matrices such as those developed by H.B. Keller, the iterative inversion of the associated block matrices can be achieved to satisfy (1b) directly. For coding expendiency, we have, however, elected to replace direct satisfaction of (1b) by an iterative approach, in which we introduce an eigenvalue γ for which

$$f(x,-\infty) = \gamma(x) \quad .$$

In our method, the quantity γ is determined iteratively so that (1b) is satisfied.

Numerical Details

On the upper and lower surfaces of the airfoil we solve the momentum equation (Eq. (1) of Section 4.2) with boundary conditions

$$f_u(x,0) = \frac{\partial f_u(x,0)}{\partial \eta} = 0, \quad \frac{\partial f_u(x,\infty)}{\partial \eta} = 1$$

and $f_\ell(x,0) = \partial f_\ell(x,0)/\partial\eta = 0$, $\partial f_\ell(x,-\infty)/\partial\eta = 1$ on the upper and lower surfaces, respectively. For $x = x_{TE}$, we form the vector

$$\vec{F}(x) = \begin{pmatrix} \vec{f}_u(x) \\ \vec{f}_\ell(x) \end{pmatrix}$$

where $\vec{f}_u$ and $\vec{f}_\ell$ are the discrete solution vectors obtained from solving the momentum equation. For $x > x_{TE}$, we continue to solve this equation with initial conditions $\vec{F}(x_{TE})$ and boundary conditions $F(x,-\infty) = \gamma(x)$ as well as

$$\frac{\partial F}{\partial \eta}(x,-\infty) = \frac{\partial F}{\partial \eta}(x,\infty) = 1 \quad .$$

Here, $\gamma(x)$ is selected in a Newton-like iterative scheme to ensure that $F(x,0) = 0$, i.e.,

$$\gamma^{(n+1)} = \gamma^{(n)} - \frac{F(x,0,\gamma^{(n)})}{\frac{\partial F}{\partial \gamma}(x,0,\gamma^{(n)})}$$

where the superscript is the iteration counter. In practice, we approximate the derivative by

$$\frac{\partial F}{\partial \gamma}(x,0,\gamma^{(n)}) \approx \frac{F(x,0,\gamma^{(n)}) - F(x,0,\gamma^{(n-1)})}{\gamma^{(n)} - \gamma^{(n-1)}} \quad .$$

One computational difficulty encountered was that the initial conditions $\vec{F}(x_{TE})$ were not smooth enough to guarantee convergence. Accordingly, a spline least square smoothing algorithm was employed to obtain smoother starting conditions.

5.2 Parametric Studies

Using the formulation and computational procedure described in the previous section, we performed a series of studies of the wake structure behind a tangentially blown wake. A blown NACA 0012 airfoil at $M_\infty = 0.7$ and $\alpha = 3°$ was investigated, in which tangential blowing was introduced on the lower as well as the upper surface at slots located at 21% chord. The pressure distribution on the latter is shown in Fig. 45. Blowing on both surfaces was required to maintain attached flow to the trailing edge in view of the adverse pressure gradient associated with the (smoothed) shock recompression indicated in Fig. 45.

In Fig. 50, a typical streamwise evolution of the velocity profile u/u_e downstream, including the trailing edge, is shown, where u_e = the external velocity $\approx$ U the freestream value. The slot height ζ_d is expressed in terms of the Blasius variable. If u_e is the velocity at the boundary layer edge, the peak velocity parameter A for a parabolic velocity profile at the slot where

$$A = \left[4 \left(\frac{u}{U}\right)_{\text{max at slot}}\right] / \zeta_d^2$$

was assigned the value 3. The other parameters for this case are indicated in the caption of this figure. Diffusion to the symmetrical bell shaped profile is evident in the figure. Actually, this shape was achieved as early as x = 5.96 for case 1 (not shown). In spite of the rapidity of this relaxation in view of the considerable initial asymmetry, the viscous interaction process could be sensitive to the details of streamwise profile evolution in the transition phases.

In Fig. 51, the peak velocity $(u/u_e)_{max}$ as well as displacement thickness δ and momentum thickness θ, in units of $c/\sqrt{Re_\infty}$ where c = airfoil chord and Re_∞ = freestream Reynolds number, are shown. By contrast to the classical submerged jet studied by Schlichting[36] and Bickley[37] for incompressible flows, the momentum thickness in this coflowing case is strongly affected by the external pressure gradient and has a significant decay for the first 3 chord lengths downstream. Thereafter, this parameter remains almost constant as in

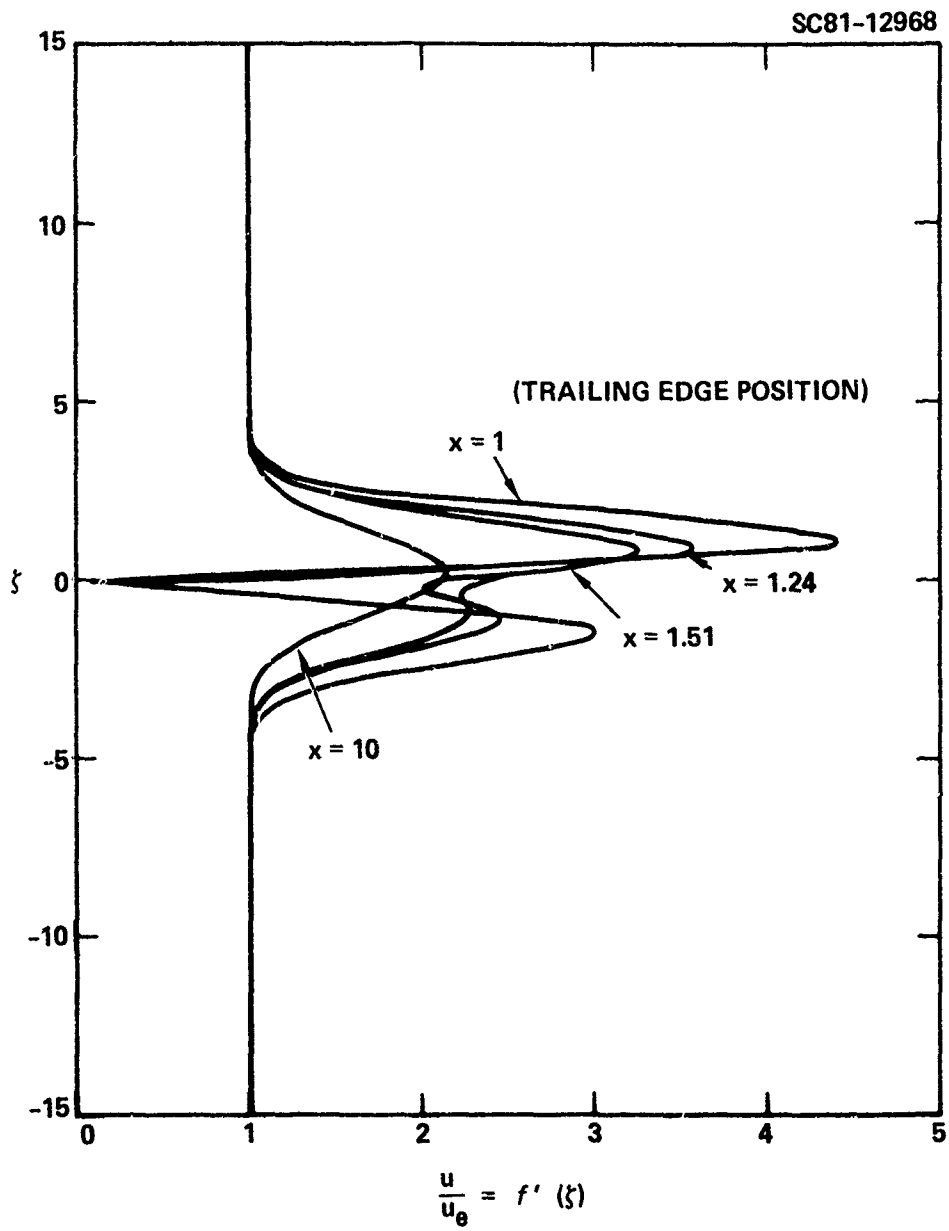

Fig. 50 Streamwise evolution from trailing edge of wake velocity profiles for NACA 0012 airfoil, $M_\infty = 0.7$, $\alpha = 3°$, blown tangentially on upper and lower surfaces at slot position x_{SL} of 21% chord, peak velocity parameter A = 3, normalized slot height $\zeta_{/j} = 2.5$.

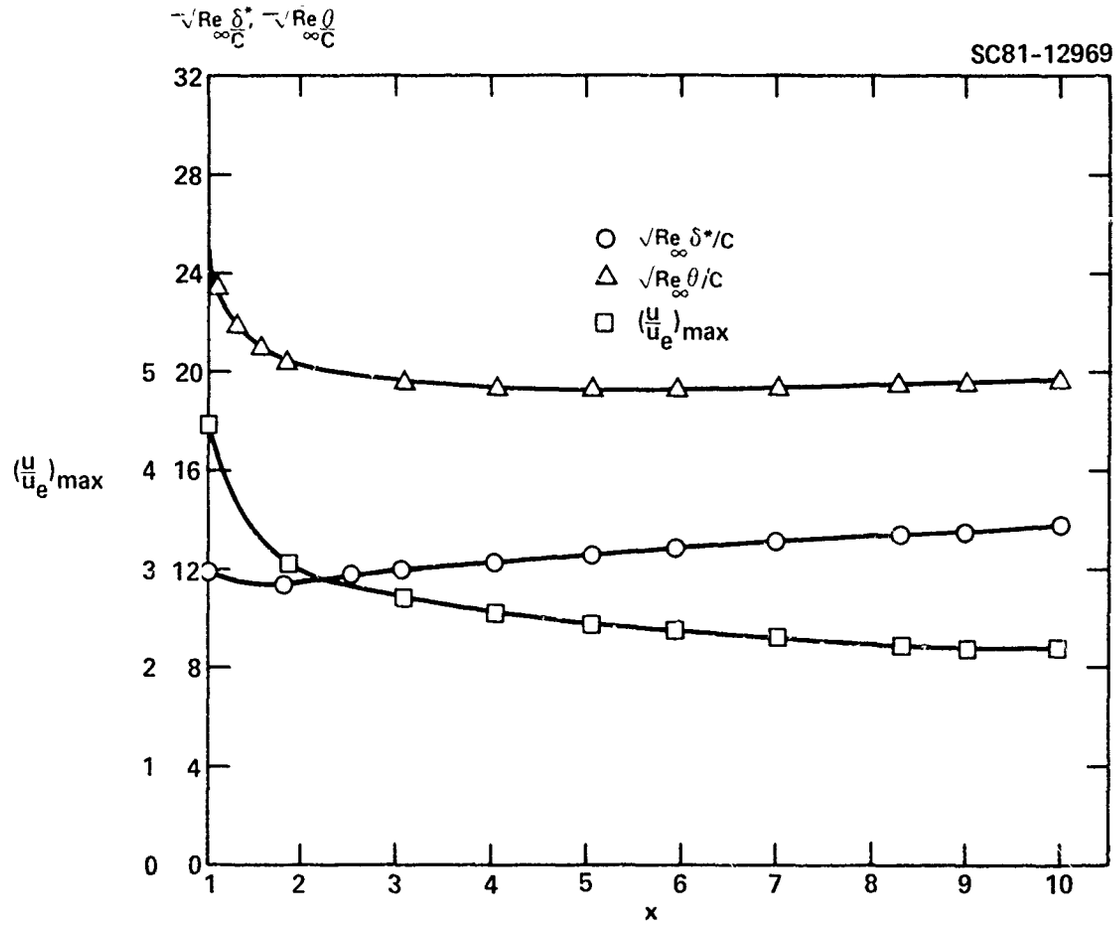

Fig. 51 Streamwise evolution from trailing edge of peak velocity and normalized displacement and momentum thicknesses for case of Figure 50.

the submerged case, in spite of the external stream. (As an approximation to obtain these results, the pressure coefficient C_p at the wake edge calculated with an SLOR solution* has been extrapolated downstream by using a monomial fit $C_p = Ax^B$.) Correspondingly, the displacement thickness relaxes to a similar invariance more quickly, as indicated in Fig. 51.

It was of interest to compare the bell shape profile to an asymptotic flat plate wake solution. Strictly speaking, this comparison is only of validity when the reduced perturbation velocity is small. Although this is not the case at the streamwise stations under consideration, we study here the extended validity of this behavior, from the viewpoint of experimental and theoretical interest.

Denoting the perturbation velocity $(u - U)/U$ as u', where U is the freestream, we define g' and ε such that

$$f' = 1 + u' \equiv 1 + \varepsilon g \quad , \quad (\varepsilon \to 0)$$
$$f = \eta + \varepsilon g$$

The momentum Eq. (1) of Section 4.2 specialized to this laminar case which is

$$f''' + \frac{ff''}{2} = x\left(f' \frac{\partial f'}{\partial x} - f'' \frac{\partial f}{\partial x}\right) \tag{2}$$

where the coefficients in the original equation have taken on limiting values in the asymptotic nearly zero pressure gradient flow reduces to the linearized form

$$g''' + \frac{\eta}{2} g'' - x \frac{\partial g'}{\partial x} = 0 \quad , \quad \left(' \equiv \frac{\partial}{\partial \eta}\right) \tag{3a}$$

with the boundary conditions

$$g(0) = g'(\infty) = g''(0) = 0 \quad . \tag{3b}$$

*Assistance of V. Shankar in obtaining these results is gratefully acknowledged.

On the basis of the invariance of θ and, correspondingly, the momentum flux J, for large x where

$$J = \int_{-\infty}^{\infty} \rho u^2 dy = \text{const.} \quad , \tag{4}$$

with y a Cartesian coordinate normal to the freestream, ρ = density, the quantity g' has the following similitude

$$g' = \frac{1}{\sqrt{x}} G(\eta) \quad . \tag{5}$$

This leads to the well known solution of (3) given by

$$g' = \frac{Ce^{-\eta^2/4}}{\sqrt{x}} \quad . \tag{6}$$

The effect of the finite size of the perturbation velocity u' is shown in Fig. 52, where the scaling of the peak velocity $u'_{peak} = \varepsilon g_\eta(x,0)$ is indicated. By contrast to (6), the numerical results suggest that $u'_{peak} \sim x^{-0.3010}$. If, however, C in (6) is determined by matching with the numerical solution such as shown in Fig. 53, or alternatively, u' is normalized to the peak velocity at each x station, a strikingly good agreement between Eq. (6) and the computationally obtained wake profile is obtained, as indicated for the conditions delineated in the figure for the blown NACA 0012 airfoil.

Regarding these facts, we have also determined that $u_{peak} \sim x^{-0.1885}$ as $x \to \infty$ for the case at hand, in contrast to the Bickley submerged jet solution where $u_{peak} \sim x^{-1/3}$. The slower rate of decay of the present coflowing jet seems consistent with the reduced action of viscous dissipation associated with the lower relative velocity between the jet and external flow. It should also be noted that this trend differs from that discussed in Birkhoff's book[38] regarding wakes with "hydrodynamic self propulsion" associated with self propelled objects such as boats or airplanes. For these cases, if no acceleration occurs, the thrust, T, is equal to the drag, D, leading to

$$J = \int_{-\infty}^{\infty} u' dy = T - D = 0 \quad . \tag{7}$$

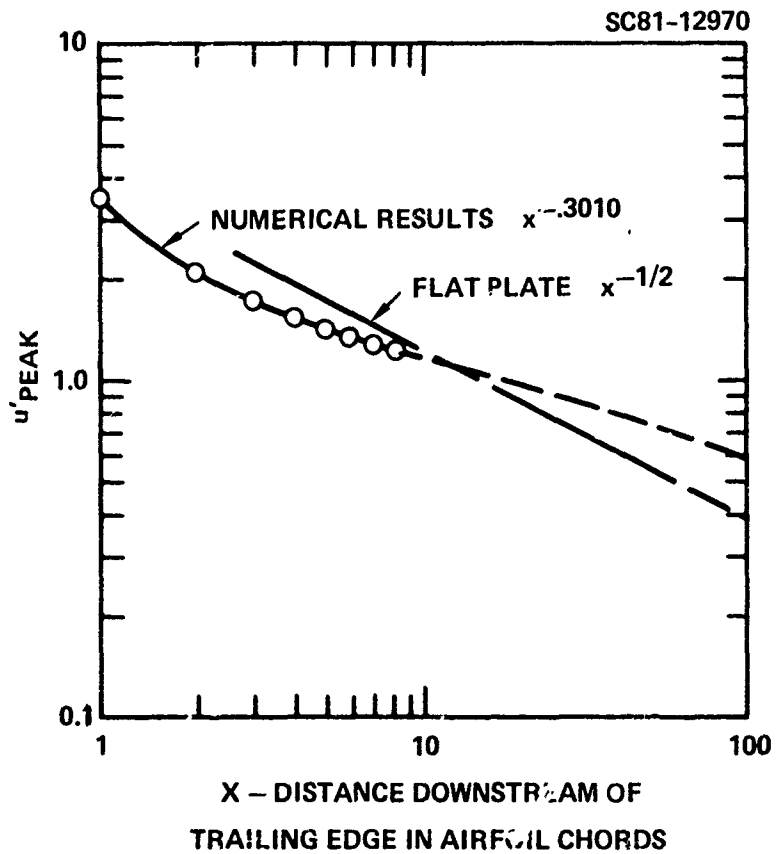

Fig. 52 Comparison of peak wake perturbation velocity (from freestream) downstream decay against flat plate similarity solution for case of Figures 50 and 51.

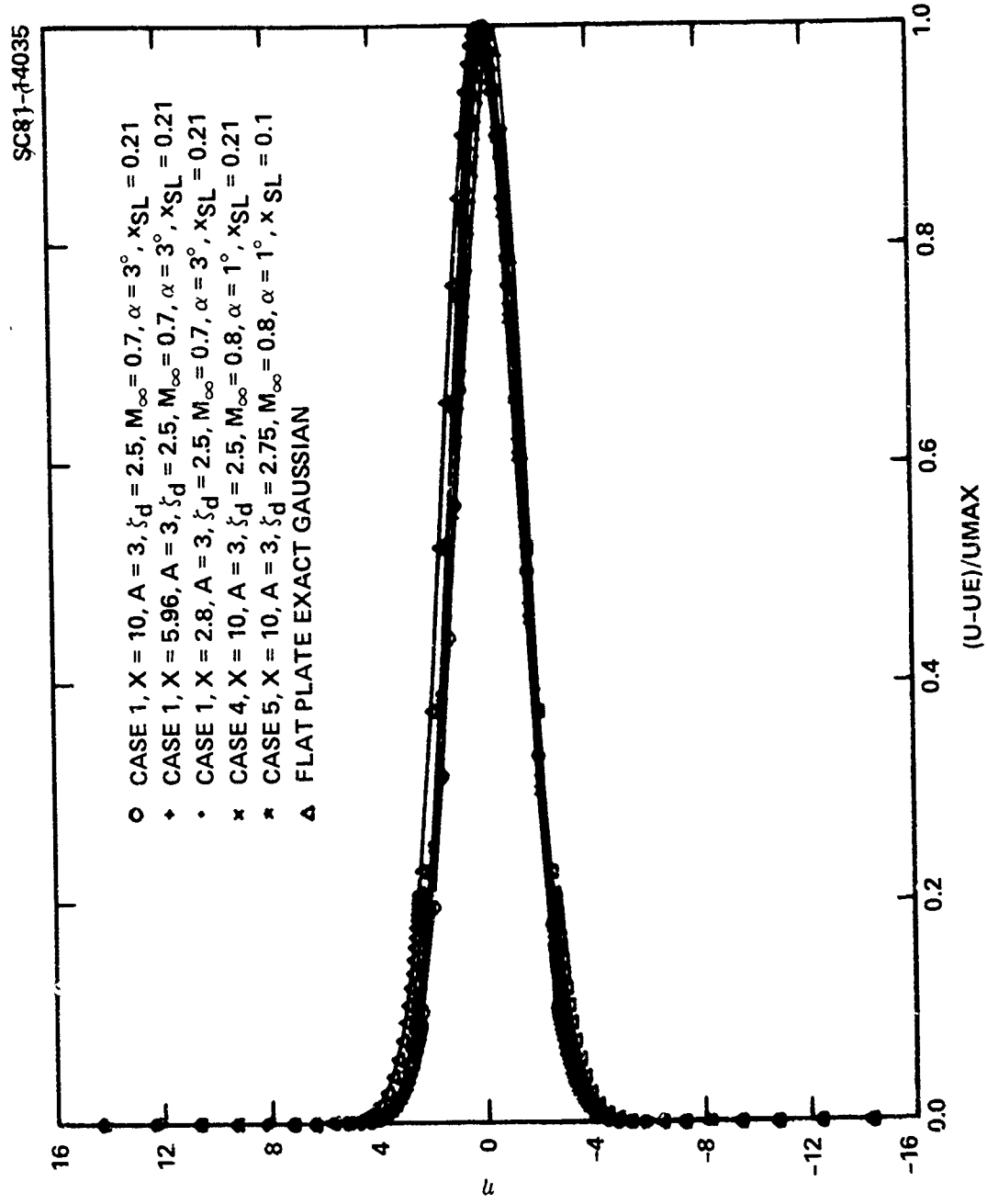

Fig. 53 Normalized wake profiles for various slot blowing cases, x is distance in chord lengths downstream of trailing edge.

For such cases, it can be shown that

$$M = \int_{-\infty}^{\infty} y^2 u dy \quad , \quad \text{invariant with } x. \tag{8}$$

The invariance (8) leads to a different similarity than for the Bickley jet. For self propelled wakes, $u_{peak} \sim x^{-3/2}$. The weaker decay experienced in the present studies is associated with the lack of similarity arising from the presence of two characteristic velocities, i.e., that from the jet momentum, and the other corresponding to the freestream. The latter boundary condition and (4) impose conflicting requirements negating similitude. The other reason for deviation from the self propelled case is the fact that T > D in the flow being computed here.

In future studies, two regimes will be considered appropriate to the blown wakes considered. For T >> D, the blown wake can be considered as a linear nonsimilar perturbation on the Bickley submerged jet similar solution for sufficiently small x. For $x \to \infty$, the wake behaves like a classical flat plate structure in which T - D is conserved.

Besides their theoretical significance, these considerations are of importance in assessing the net thrust of propulsive wings in experimental simulations. In addition, the asymptotic wake characteristics discussed here will be employed in modeling the far field for the blown viscous interaction problem in subsequent studies.

6.0 CONCLUSIONS

During the course of the research program, a number of areas received attention in connection with the study of tangentially blown airfoils. Particular emphasis has been placed on understanding the structure of compressible wall jets occurring in such flow fields. Modern relaxation methods have provided an efficient means of analyzing the diversity of wave patterns arising in these jets. For submerged transonic jets, with subsonic conditions infinitely far downstream and a specified exit velocity profile, the following specific findings arise associated with unchoked flow over a series of wall shapes.

- The Kutta condition on the nozzle rim can be satisfied merely by requiring streamwise continuity of the potential across the rim as a trailing edge for the flow. With the use of this procedure, the numerical algorithm correctly tracks a local singular solution which has a square root zero and is locally harmonic in scaled variables, providing the rim is not transonic.

- As compared to unconfined flows, the slip line boundaries create a rapid decay of the disturbances. The functional form of the far field perturbation potential is an exponential damped sine, similar to that encountered for incompressible flow but different in that its amplitude interacts nonlinearly with the near field.

- Analysis of the free jet case indicates subcritical monotone streamwise variations of the pressure for a subsonic jet exit, as in linear subsonic flow.

- Acceleration of the wall jet to criticality over convex walls is accomplished by stream tube contractions and throats induced by upstream influence of the turning.

- The upper slip line of the wall jet becomes asymptotically parallel to that emanating from the trailing edge infinitely far downstream.

For this phase of the effort, as well as that dealing with coflowing jets, the inverse methods reported in Refs. 27-29 appear to be an attractive means to reduce wave drag and enhance thrust recovery by elimination of shock waves by suitable wall contouring.

With regard to the investigation of coflowing wall jets, selection rules have been identified for the existence of throats in the jets on the basis of an integral theorem based on small disturbance formulation of a unit problem involving a flat plate cowl. The latter has important features that are of relevance to more complicated cowl geometries. For a slightly subsonic external flow, with an embedded jet at nearly the same velocity and settling pressure, approximately sixteen cases have been enumerated depending on the range of jet similarity parameter. Computational results have validated some of these cases. The information provided in this phase illuminates factors influencing the penetration length of initially supersonic jets and the scales affecting overexpansion spikes evident in experiments over blown surfaces of propulsive wings.

In the portion of the study dealing with the complete problem of a tangentially blown airfoil, asymptotic and computational simulations have received attention in incompressible and transonic regimes. These analyses have utilized models of the jet that are accurate in regions away from the nozzle exits and that are capable of later integration of the results of the aforementioned basic studies of coflowing wall jets appropriate to a local description of the exit flows. For the more globally oriented inviscid blown airfoil models, the analytical and computational models indicate that:

- In the thin jet small deflection approximation, the pressure jumps associated with the Spence theory prevail even if the flow is rotational and compressible.

- The asymptotic developments provided allow further systematic refinements.

- Effects associated with initial skewness and vorticity inaccessible to other theories can be assessed.

- For finite trailing edge angles, the dividing streamline leaves tangent to the higher stagnation pressure side if upper and lower stagnation pressures are not equal and at the trailing edge bisector if they are.

- Computational results obtained for transonic USB configurations indicate significant enhancements of lifting pressures associated with blowing.

- Comparisons with experiment indicate the need for refinements incorporating wave interaction phenomena near the jet exit as well as viscous interaction processes in the downstream portion of the wall jet.

Initial results characterizing viscous effects using finite difference laminar descriptions of the flow fields demonstrate clearly that:

- Substantial downstream movements in the shock-induced separation point are achievable with application of tangential blowing. By computational schemes, these delays can be inexpensively quantified as compared to experimental methods.

- The propulsive wake at great distances downstream gives a nearly Gaussian normalized velocity profile in spite of a lack of self similarity which occurs in purely submerged or self propelled cases. This result is of significance for assessment of net thrust in experimental simulations and theoretical far-field modeling.

With the viscous module and the appropriate iterative coupling algorithm to the external flow to be implemented in the near future, optimization between separation suppression, wave drag minimization, and supercirculation control will be possible. It is envisioned that the design techniques contained in Refs. 27-29 will augment this capability by providing methods to modulate shock formation in concert with the blowing effects.

On a more ambitious scale, which will depend on further developments in current parabolic marching schemes and improvement and application of multiple deck asymptotic models, future effort should consider blowing effects on:

- Strong shock boundary layer interactions with limited separation near the foot of the incident normal shock and trailing edge
- Blowing effect on near wake curvature modification of viscous lift at trailing edge and cowl lip
- Impact of shock waves in the jet on wall jet transition and separation.

7.0 REFERENCES

1. Spence, D.A., "The Lift Coefficient of a Thin Jet Flapped Wing," Proc. Roy. Soc., Ser. A., 238, December 1956, pp. 46-48.

2. Sato, J., "Discrete Vortex Method of Two-Dimensional Jet Flaps," AIAA J., Vol. 11, July 1973, pp. 968-973.

3. Halsey, N.D., "Methods for the Design and Analysis of Jet Flapped Airfoils," AIAA Paper 74-188, AIAA 12th Aerospace Sciences Meeting, 1974.

4. Leoman, R.G. and Plotkin, A., "An Improved Solution of the Two-Dimensional Jet Flapped Airfoil Problem," J. Aircraft, Vol. 9, September 1972, pp. 631-635.

5. Malmuth, N.D. and Murphy, W.D., "An Inviscid Model for Submerged Transonic Wall Jets," AIAA Paper 77-174 (1977).

6. Malmuth, N.D., Murphy, W.D., Shankar, V., Cole, J.D., and Cumberbatch, E., "Studies of Upper Surface Blown Airfoils in Incompressible and Transonic Flows," AIAA Paper 80-0270, AIAA 18th Aerospace Sciences Meeting, Pasadena, California, January 14-16, 1980 and to be published in the AIAA J. November 1981.

7. Malmuth, N.D., Murphy, W.D., Shankar, V., Cole, J.D. and Cumberbatch, E., "Flow Structures Associated with Upper Surface Blown Airfoils," Invited paper presented at the Symposium on Numerical and Physical Aspects of Aerodynamic Flows, California State University, Long Beach, California, January 19-21, 1981, in proceedings to be published by Springer-Verlag.

8. Chaplygin, S.A., "On Gas Jets," NACA Technical Memorandum, TM 1063, 1944.

9. Frankl, F.I., "On the Problem of Chaplygin for Mixed Subsonic and Supersonic Flows," NACA Technical Memorandum TM 1155, 1947.

10. Guderley, K.G., The Theory of Transonic Flow, Pergamon Press, Oxford, 1962, pp. 124-127.

11. Courant, R., and Hilbert, D., Methods of Mathematical Physics, Vol. II, Interscience Publishers, N.Y., pp. 225-226.

12. Weinstein, A., "Conformal Representation and Hydrodynamics," Proc. First Canadian Math. Congress, University of Toronto Press, Toronto (1946), pp. 355-364.

13. Murman, E.M., "Analysis of Embedded Shock Waves Calculated by Relaxation Methods," Proc. Computational Fluid Dynamics Conference, Palm Springs, Calif., July 19-20, 1973, pp. 27-40.

14. Jameson, A., "Iterative Solution of Transonic Flows over Airfoils and Wings, Including Flows at Mach 1," Comm. Pure Appl. Math. 27, 1974, pp. 283-309.

15. Bailey, F.R. and Ballhaus, W.F., "Comparisons of Computed and Experimental Pressures for Transonic Flows About Isolated Wings and Wing-Fuselage Configurations," in Proc. Conference on Aerodynamic Analyses Requiring Advanced Computers, Part II, Langley Research Center, Hampton, Va., NASA SP-347, March 4-6, 1975, pp. 1213-1232.

16. Murman, E.M. and Cole, J.D., "Calculations of Plane Steady Transonic Flows," AIAA J. 9, January, 1971, pp. 114-121.

17. Krupp, J.A., "The Numerical Calculation of Plane Steady Transonic Flows Past Thin Lifting Airfoils," Ph.D. Thesis, University of Washington, June 1971.

18. Woods, L.C., "The Relaxation Treatment of Singular Points in Poisson's Equations," Quart. J. Mech. and Appl. Math. VI pt. 2, 1953, pp. 163-185.

19. Murman, E.M., "Computation of Wall Effects in Ventilated Transonic Wind Tunnels," AIAA Paper 72-1007, September 1972.

20. Pinzola, M. and Lo, C.F., "Boundary Interference at Subsonic Speeds in Wind Tunnels with Ventilated Walls," AEDC Technical Report TR-69-47, May 1969.

21. Malmuth, N.D. and Murphy, W.D., "A Relaxation Solution for Transonic Flow over Jet Flapped Airfoils," AIAA J., Vol. 14, September 1976, pp. 1250-1257.

22. Noble, B. Methods Based on the Weiner-Hopf Technique for the Solution of Partial Differential Equations, Pergamon Press, London, New York, 1958, (problem 3.20 p. 139).

23. Cole, J.D., Perturbation Methods in Applied Mathematics, Ginn and Blaisdell, Waltham, Massachusetts (1968).

24. Mangler, K.W. and Smith, J.H.B., "Behavior of the Vortex Sheet at the Trailing Edge of a Lifting Wing," Aeronautical Journal, Vol. 74, November 1970, pp. 906-908.

25. Yoshihara, H., Carter, W.V., Fatta, J.G., and Magnus, R.G., "Aeronautical Exploratory Research on Jet Flapped Airfoils," Convair Report L-112173, February 1972.

26. Pearcey, H.H., "Shock Induced Separation and Its Prevention by Design and Boundary Layer Control," Boundary Layer and Flow Control, Lachmann, G.V., ed., Pergamon, Oxford, London, 1961, pp. 1166-1344.

27. Shankar, V., Malmuth, N.D., and Cole, J.D., "Computational Transonic Airfoil Design in Free Air and a Wind Tunnel," AIAA Paper 78-103, AIAA 16th Aerospace Sciences Meeting, Huntsville, Alabama, January 16-18, 1978.

28. Shankar, V., Malmuth, N.D., and Cole, J.D., "A Consistent Design Procedure for Supercritical Airfoils in Free Air and a Wind Tunnel," invited paper presented at NASA-Langley Conference on Advanced Technology Research, also in Proceedings, March 1978.

29. Shankar, V., Malmuth, N.D., and Cole, J.D., "A Computational Inverse Procedure for Three-Dimensional Wings and Wing-Body Combinations," AIAA Paper 79-0344, presented at the 17th Aerospace Sciences Meeting, New Orleans, Louisiana, January 15-17, 1979.

30. Schlichting, H., Boundary Layer Theory, McGraw Hill, New York, 1st ed., 1955, pp. 215, 216.

31. Goldstein, S., Modern Developments in Fluid Dynamics, Vol. I, Oxford, London, 1938, p. 163.

32. Schubauer, G.B., "Air Flow in a Separating Laminar Boundary Layer," NACA Rep. 527 (1935).

33. Diewert, S., "Numerical Simulation of High Reynolds Number Transonic Flows," AIAA J. 13, October 1975, pp. 1354-1359.

34. Keller, H.B. and Cebeci, T., "Accurate Numerical Methods for Boundary Layers, II, Two-Dimensional Turbulent Flows," AIAA J., 10, September 1972, pp. 1197-1200.

35. Kusunose, K., "Two-Dimensional Flow Past Convex and Concave Corners at Transonic Speed and Two-Dimensional Flow Around a Parabolic Nose at Transonic Speeds," Ph.D. Thesis, University of California at Los Angeles, 1979.

36. Schlichting, H., "Laminare Strahlenaushbreitung," ZAMM 13 1933, pp. 260-263.

37. Bickley, W., "The Plane Jet," Phil. Mag. Ser. 7, 23, 1939, pp. 727-731.

38. Birkhoff, G. and Zarantonello, E., Jets, Wakes, and Cavities, Applied Mathematics and Mechanics, Vol. 2, Academic Press, N.Y., 1957, pp. 307-309.

39. Cebeci, T., Kaups, K., and Ramsey, J., "A General Method for Calculating Three-Dimensional Compressible Laminar and Turbulent Boundary Layers on Arbitrary Wings," NASA Contractor Rep. NASA CR 2777, January 1977.

40. Preston, J.H., "Note on the Circulation in Circuits Which Cut the Wake of an Airfoil at Right Angles," Rep. Memor. Aero. Res. Counc. Lond. 2957, 1954.

8.0 PUBLICATIONS AND PAPERS ARISING FROM THE RESEARCH PROGRAM

1. Malmuth, N.D. and Murphy, W.D., "An Inviscid Model for Submerged Transonic Wall Jets," AIAA Paper 77-174 (1977).

2. Malmuth, N.D., Murphy, W.D., Shankar, V., Cole, J. and Cumberbatch, E., "Studies of Upper Surface Blown Airfoils in Incompressible Flow," AIAA Paper 80-0270, presented at the AIAA Aerospace Sciences Meeting, January 14-16, 1980, Pasadena, California, (to be published in generalized form in AIAA J. November 1981.

3. Malmuth, N.D., Cole, J.D. and Murphy, W.D., "Flow Regimes in Coflowing Transonic Wall Jets," in preparation for submission to AIAA J.

4. Malmuth, N.D., Murphy, W.D., Shankar, V., Cole, J.D., and Cumberbatch, E., "Flow Structures Associated with Upper Surface Blown Airfoils," invited paper presented at the Symposium of Numerical and Physical Aspects of Aerodynamic Flows, California State University, Long Beach, California, January 19-21, 1981, in proceedings to be published by Springer-Verlag.

5. Malmuth, N.D., Murphy, W.D., and Cole, J.D., "Studies of Lift Enhancement and Separation Control for Transonic Upper Surface Blowing," invited briefing presented at "Ejector Workshop for Aerospace Applications," University of Dayton Research Institute, August 3-5, 1981.

6. Murphy, W.D., Malmuth, N., and Cole, J.D., "Numerical Treatment of Blown Boundary Layers and Wakes Over Transonic Airfoils," invited paper to be presented at the Second International Conference on Boundary and Interior Layers - Computational and Asymptotic Methods, under the auspices of the Numerical Analysis Group and cosponsored by the American Institute of Aeronautics and Astronautics, American Meteorological Society, Institute for Numerical Computation and Analysis, Irish Mathematical Society, Dublin, Ireland, June 16-18, 1982.

APPENDIX A
DETAILS OF VISCOUS FORMULATION

Governing Equations

In what follows, the approach to treat the viscous regions of the flow field will be described. In major respects, the formulational aspects given here resemble those given in Ref. 39. However, certain important details associated with the blowing application require special treatment. For a self contained account, therefore, some of the unblown formulation is repeated here. Referring to the curvilinear axis system shown in Fig. A1, the boundary layer equations (which include laminar and turbulent cases) to be utilized to calculate viscous zones are as follows:

Continuity

$$\frac{\partial}{\partial x}(\rho u) + \frac{\partial}{\partial y}(\overline{\rho v} h_1) = 0 \tag{1a}$$

x-Momentum

$$\frac{\rho u}{h_1}\frac{\partial u}{\partial x} + \overline{\rho v}\frac{\partial u}{\partial y} = -\frac{1}{h_1}\frac{\partial p}{\partial x} + \frac{\partial}{\partial y}\left(\mu \frac{\partial u}{\partial y} - \rho\overline{u'v'}\right) \tag{1b}$$

Energy

$$\frac{\rho u}{h_1}\frac{\partial H}{\partial x} + \overline{\rho v}\frac{\partial H}{\partial y} = \frac{\partial}{\partial y}\left[\frac{\mu}{Pr}\frac{\partial H}{\partial y} + \mu\left(1 - \frac{1}{Pr}\right)\frac{\partial}{\partial y}\left(\frac{u^2}{2}\right) - \rho\overline{v'H'}\right] \tag{1c}$$

where as a typical average, $\overline{\rho v} = \rho v + \overline{\rho' v'}$, and as usual, the primes denote fluctuations about temporal averages,* Pr is the Prandtl number, ρ = density, u,v are velocity components in the x and y direction, respectively, H = total

*The appropriate eddy viscosity representations for the Reynolds stresses have not been considered in this phase of the effort, but will receive attention in later aspects concerning marching of the boundary layer downstream of impingement points of shocks from the external flow.

SC80-8069

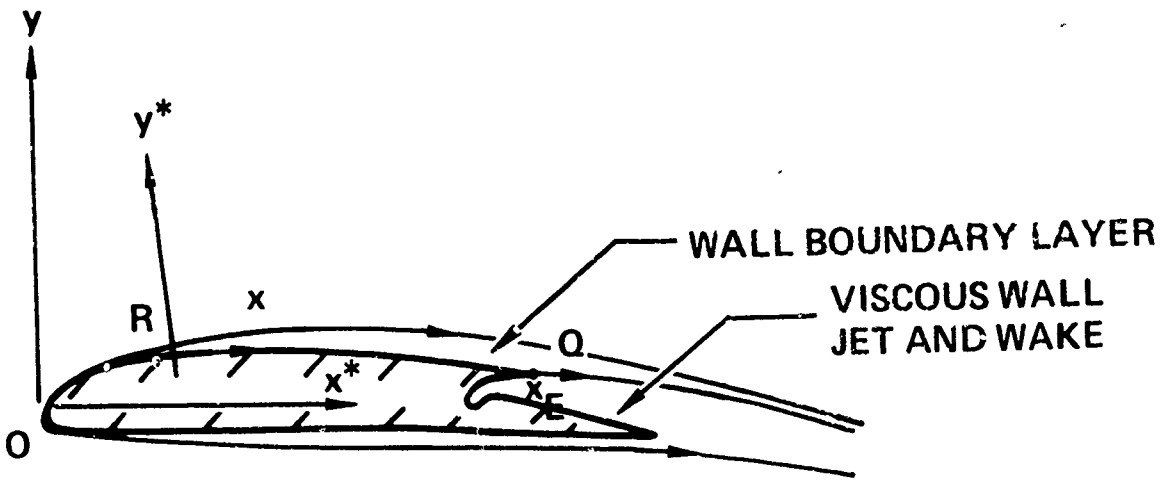

Fig. A1 Upper surface blown airfoil showing viscous zones.

enthalpy, μ = dynamic viscosity, and h_1 = metric. If in the x*,y* Cartesian coordinate system shown in Fig. A1, the surface of the airfoil is given as

$$y = F(x^*) \quad ,$$

then the metric h_1 is given by

$$h_1 = \sqrt{1 + [F'(x^*)]^2} \quad .$$

Boundary Conditions

The appropriate conditions for the solution of (1) consist of surface constraints, initial conditions, and matching considerations to the outer flow. The surface conditions are given as follows:

Surface (No Slip and Adiabatic Wall)

$$u(x,0) = v(x,0) = 0 \tag{2a}$$

$$\frac{\partial H}{\partial y}(x,0) = 0 \quad . \tag{2b}$$

Initial Conditions

In Appendix B, a local nose solution is considered which is utilized to start the solution in a manner appropriate to the parabolic initial boundary value problem for Eqs. (1).

At the jet exit, $x = x_E$, referring to Fig. A2; an initial profile is specified on the blown section AB. The data on BC is "inherited" from history of the flow field which has been marched to this point from the boundary layer and external flow through iterations between successive sweeps of some sort of successive line relaxation method or other inviscid solver. A key point is the following: The solution of (1), subject to the initial conditions in ABC, characterizes the mixing of the flow exhausting from the nozzle and the boundary layer along the upper surface of the airfoil (ORC in Fig. A1). A similar treat-

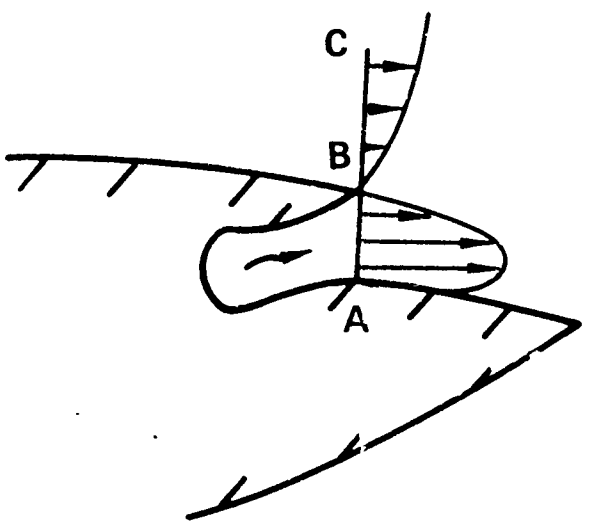

Fig. A2 Confluence of streams at jet exit.

ment has been used to handle the mixing of the upper and lower streams in the wake region downstream of the trailing edge and to establish the jump conditions for the pressure. These will be a viscous modification of the Spence jump conditions developed from concepts of Preston and implemented by us (Refs. 5-7).

Matching with Outer Flow

The appropriate boundary conditions at the edge of the viscous region are:

$$\lim_{y \to \infty} u(x,y) = u_e(x) \tag{3a}$$

$$\lim_{y \to \infty} v(x,y) = v_e(x) \tag{3b}$$

$$\lim_{y \to \infty} \rho(x,y) = \rho_e(x) \quad , \tag{3c}$$

where the quantities on the right side of Eqs. (3) are effectively the inner limit of the outer flow, i.e., if $W(x,y)$ is one typical such quantity, then $W_e(x) \sim \lim_{y \to \infty} W(x,y)$. (e ~ external.)

Transformed Problem

In this section, we generalize the procedure given in Ref. 2 to the blown boundary layer problem indicated previously. On introduction of transformed independent variables

$$x = x, \; d\zeta = \left(\frac{u_e}{\rho_e \mu_e s_1}\right)^{1/2} \rho dy \quad , \quad s_1 = \int_0^x h_1 dx \tag{4a}$$

and the dependent variables

$$\rho u = \frac{\partial \psi}{\partial y} \quad , \quad \overline{\rho v} h_1 = -\frac{\partial \psi}{\partial x} \tag{4b}$$

with

$$\psi = (\rho_e \mu_e u_e s_1)^{1/2} f(x;\zeta) \quad , \tag{4c}$$

the system (1) under the transformation (4) becomes

$$(bf'')' + m_1 ff'' + m_2 f'^2 - m_{11} c = m_{10}\left[f' \frac{\partial f'}{\partial x} - f'' \frac{\partial f}{\partial x}\right] \tag{5a}$$

$$(\mu_1 E')' + \mu_2 E' + \mu_3' = m_{10}\left(f' \frac{\partial E}{\partial x} - E' \frac{\partial f}{\partial x}\right) \tag{5b}$$

where primes denote partial differentiation with respect to ζ, and

$$f' = \frac{u}{u_e}\ ,\ E = \frac{H}{H_e}\ ,\ b = C(1 + \varepsilon_m^\dagger)\ ,\ c = \frac{\rho\mu}{\rho_e\mu_e}\ ,\ c = \frac{\rho_e}{\rho}$$

$\varepsilon_m^\dagger$ = eddy viscosity (= 0 for laminar flow)

e signifies conditions on the edge of the boundary layer

$$m_1 = \frac{1}{2}\left(1 + \frac{s_1}{h_1 u_e}\frac{\partial u_e}{\partial x}\right) + \frac{s_1}{h_1\sqrt{\rho_e\mu_e}}\frac{\partial}{\partial x}\left(\sqrt{\rho_e\mu_e}\right) = \frac{1}{2}(1 + m_2) + \frac{s_1}{h_1\sqrt{\rho_e\mu_e}}\frac{\partial}{\partial x}\left(\sqrt{\rho_e\mu_e}\right)$$

$$s_1 = \int_0^x h_1 dx$$

$$m_2 = \frac{s_1}{h_1 u_e}\frac{\partial u_e}{\partial x}$$

$$m_{10} = \frac{s_1}{h_1}$$

$$m_{11} = \frac{s_1}{u_e h_1}\frac{\partial u_e}{\partial_x} = m_2$$

$$\mu_1 = \frac{C}{Pr}\left(1 + \varepsilon_m^\dagger \frac{Pr}{Pr_t}\right),\ \mu_2 = m_1 f\ ,\ \mu_3 = C\frac{u_e^2}{H_e}(1 - Pr^{-1})\ f'f''\ .$$

Here, dagger superscripts refer to turbulent quantities. Herein, it will be assumed for convenience that the Prandtl number is unity.

Boundary Conditions

The transformed versions of (2) and (3) are

$$\zeta = 0 \ , \ f = f' = E' = 0 \tag{6a}$$

$$(\zeta = \zeta_\infty) \gg 1) \ , \ f' = E' = 1 \quad . \tag{6b}$$

In accord with the remarks given in Section 4.1, we have assumed in our studies that Pr = 1, C = 1 (Chapman gas). An integral of (5b) satisfying these conditions is E = 1. In addition, we assume throughout that $\mu_e = \mu_\infty$, where subscript ∞ denotes freestream conditions.

Numerical Procedures

The discretization of the system (5) appropriate to treatment of the viscous regions will be indicated. These equations are written as a first order system by introducing the new independent variables $u(x,\zeta)$, $v(x,\zeta)$, and $G(x,\zeta)$. Thus, Eqs. (5) can be written as

$$f' = u \tag{7a}$$

$$u' = v \tag{7b}$$

$$(bv)' + m_1 fv + m_2(c-u^2) = m_{10}\left(u \frac{\partial u}{\partial x} - v \frac{\partial f}{\partial x}\right) \tag{7c}$$

$$E' = G \tag{7d}$$

$$(\mu_1 G)' + \mu_2 G + \mu_3' = m_{10} \left(u \frac{\partial E}{\partial x} - G \frac{\partial f}{\partial x}\right) \quad . \tag{7e}$$

Using Keller's box scheme (7a), (7b), and (7d) become

$$\frac{f_j^n - f_{j-1}^n}{h_j} = u_{j-1/2}^n \tag{8a}$$

$$\frac{u_j^n - u_{j-1}^n}{h_j} = v_{j-1/2}^n \tag{8b}$$

$$\frac{E_j^n - E_{j-1}^n}{h_j} = G_{j-1/2}^n \tag{8c}$$

where we have averaged about the point $(x_n, \zeta_{j-1/2})$. Using the box centered at $(x_{n-1/2}, \zeta_{j-1/2})$, Eq. (7c) is discretized as:

$$\frac{(bv)_j^n - (bv)_{j-1}^n}{h_j} + (m_1)_{n-1/2} f_{j-1/2}^n v_{j-1/2}^n + (m_2)_{n-1/2} (c-u^2)_{j-1/2}^n$$

$$+ (m_{10})_{n-1/2} \left[v_{j-1/2}^n \frac{(f_{j-1/2}^n - f_{j-1/2}^{n-1})}{k_n} + \frac{v_{j-1/2}^{n-1} f_{j-1/2}^n}{k_n} - \frac{(u_{j-1/2}^n)^2}{k_n} \right] = s_{n-1} \tag{8d}$$

where

$$s_{n-1} = \frac{(bv)_{j-1}^{n-1} - (b)_j^{n-1}}{h_j} - (m_1)_{n-1/2} (fv)_{j-1/2}^{n-1} - (m_2)_{n-1/2} (c-u^2)_{j-1/2}^{n-1}$$

$$- (m_{10})_{n-1/2} \left(u_{j-1/2}^{n-1} u_{j-1/2}^{n-1} + v_{j-1/2}^{n-1} f_{j-1/2}^{n-1} \right) \Big/ k_n \quad .$$

Similarly, Eq. (7e) is discretized

$$\frac{(\mu_1 G)_j^n - (\mu_1 G)_{j-1}^n}{h_j} + (\mu_2)_{j-1/2}^{n-1/2} G_{j-1/2}^n + (m_{10})_{n-1/2}$$

$$\times \left[G_{j-1/2}^n \frac{(f_{j-1/2}^n - f_{j-1/2}^{n-1})}{k_n} - 2u_{j-1/2}^{n-1/2} \frac{E_{j-1/2}^n}{k_n} \right] = t_{n-1} \tag{8e}$$

where

$$t_{n-1} = \frac{(\mu_1 G)_{j-1}^{n-1} - (\mu_1 G)_j^{n-1}}{h_j} - (\mu_2)_{j-1/2}^{n-1/2} G_{j-1/2}^{n-1} + \frac{(\mu_3)_{j-1}^{n-1/2} - (\mu_3)_j^{n-1/2}}{h_j}$$

$$= (m_{10})_{n-1/2} \left[2u_{j-1/2}^{n-1/2} E_{j-1/2}^{n-1} + G_{j-1/2}^{n-1} \left(f_{j-1/2}^{n} - f_{j-1/2}^{n-1} \right) \right] \Big/ k_n \quad .$$

The boundary conditions for system (8) are

$$f_0^n = u_0^n = 0 \qquad u_J^n = 1 \tag{9a}$$

$$G_0^n = 0 \qquad E_j^n = 1 \quad . \tag{9b}$$

Note that (8c) and (8e) form a linear system which is decoupled from (8abc). Therefore, we first solve the nonlinear system (8abc) with boundary conditions (9a). Then, we solve the linear system (8de) with boundary conditions (9b). Initial conditions are obtained from considerations in Appendix B and the jet exit conditions.

APPENDIX B
NOSE SOLUTION AND SPECIAL PROCEDURES

The approximate uniformly valid solution utilized applies to a wide class of airfoils of finite radius of curvature. Denoting x*,y* Cartesian coordinates as shown in Fig. 44, this family of airfoils has a local representation near the nose given by

$$y^* = \delta\left[a_0\sqrt{x^*} + a_1 x^* + \mathcal{O}(x^{*2})\right] \tag{1}$$

where a_0 and a_1 are constants and δ is the thickness ratio. For example, the NACA 0012 has

$$\delta = 0.12 \quad , \quad a_0 = 1.4845 \quad , \; a_1 = 0.63 - \alpha$$

where α is the incidence, and all lengths are units of the chord.

Based on the previous remarks, a uniformly valid representation for the edge velocity component parallel to the surface u_e was assumed to be

$$\frac{u_e}{U} = 1 - \frac{\delta^{2/3} C_0}{\left[\sqrt{x^*} + \delta C_0^{3/2}\right]^{2/3}} \tag{2}$$

where the constant C_0 is determined by patching to the SLOR solution and U is the freestream velocity. Note that as $x^* \to \infty$

$$\frac{u_e}{U} \doteq \delta^{2/3} \phi_{x^*}$$

$$\Rightarrow \phi_x \doteq - C_0 x^{*-1/3} \quad , \tag{3}$$

which is in agreement with the inner expansion of the Karman Guderley flow. On the other hand, as $x^* \to 0$

$$\frac{u_e}{U} \triangleq Ax + Bx^2 + \cdots \text{ (incompressible stagnation point flow)}$$

x = arc length

with

$$A = \frac{2}{3\delta^2 a_0 C_0^{3/2}} \quad , \quad B = -\frac{2}{3}\frac{a_1}{\delta^3 a_0^3 C_0^{3/2}} + \frac{5}{9\delta^4 a_0^2 C_0^3} \quad .$$

We note that (1) can be reverted to give

$$\sqrt{x^*} = \frac{x}{\delta a_0} + \frac{1}{\delta^2}\frac{a_1 x^2}{a_0^3} + \quad (x^3) \quad . \tag{4}$$

From (2)-(4), the pressure gradient parameter

$$G(x) \equiv \frac{x}{u_e}\frac{\partial u_e}{\partial x}$$

appearing in the m_i's defined in Appendix A can be evaluated as

$$G(x) = 1 + \frac{B}{A}x + \mathcal{O}(x^2) \quad .$$

Furthermore, the quantity c appearing in Eq. (5a) is obtained as

$$c = \frac{1 - mf'^2}{1 - m} \tag{5a}$$

with

$$m \equiv \frac{(\frac{u_e}{U})^2}{1 + \frac{2}{(\gamma-1)M_\infty^2}} \quad . \tag{5b}$$

In our procedure, the foregoing relations in this section are utilized to obtain a boundary layer solution from the stagnation point, x_s, to a downstream station x_1. For $x > x_1$, u_e is determined from the SLOR solution and the boundary layer equations are matched using the data at x_1 as initial conditions.

APPENDIX C
JUMP CONDITIONS ACROSS BOUNDARY LAYERS AND WAKES

In this section, the appropriate jump conditions across the viscous regions will be studied by using second order boundary layer theory. For this purpose, matched asymptotic expansion procedures will be employed by using intermediate variables to effect the matching. The derivation indicated will be for incompressible conditions. However, similar results are envisaged for the compressible case.

In Fig. C1, a coordinate system consisting of parallels to the surface and their orthogonal trajectories is indicated. The Navier-Stokes equations for incompressible flow are:

Continuity: $\nabla \cdot \vec{q} = 0$

Momentum: $\nabla(\frac{q^2}{2}) - \vec{q} \times \vec{\omega} = - \vec{q} \cdot \nabla\vec{q} = - \frac{\nabla p}{\rho} - \nu \text{ curl } \vec{\omega}$

where ω = vorticity = curl $\vec{q}$, $\vec{q}$ = velocity vector, p = pressure, and ν = kinematic viscosity. In the coordinates indicated, denoting s as the arc length along the parallels t = constant,

ds_1 = differential arc length along surface = $R(s)d\theta$
R = radius of curvature, θ = angle between normals, s = constant
ds = differential arc length along arc above surface = $(R+t)d\theta$.

For this system, an elementary displacement vector $d\ell$ can be expressed in terms of the metrics h_1 and h_2 as

$$d\ell^2 = h_1^2 ds^2 + h_2^2 dt^2$$

where

$$h_1 = \frac{t}{1 + R(s)} \quad , \quad h_2 = 1 \quad .$$

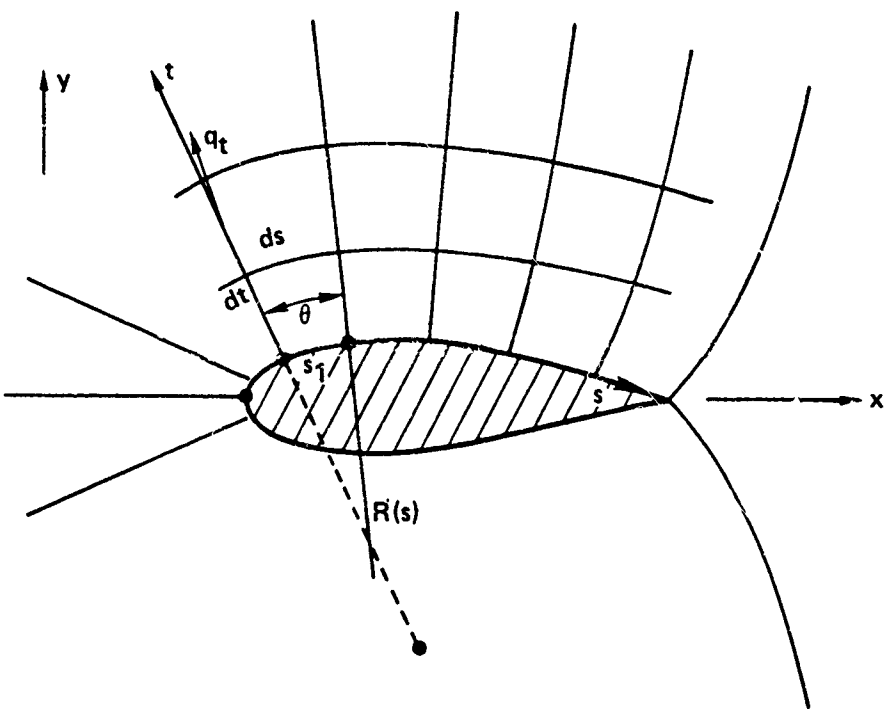

Fig. C1 Curvilinear coordinates.

If q_t and q_s represent the velocity components in the t and s directions, respectively, then the vorticity $\vec{\omega}$ can be expressed as

$$\vec{\omega} = \omega \vec{k}$$

where $\vec{k}$ is normal to the x,y plane, with x and y being Cartesian coordinates as indicated in Fig. C1. The quantity ω is then given by

$$\omega = \frac{1}{1 + \frac{t}{R}} \left[\frac{\partial q_t}{\partial s} - \frac{\partial}{\partial t} \left(1 + \frac{t}{R(s)} q_s\right) \right] .$$

Moreover,

$$\text{curl } \vec{\omega} = \frac{\partial \omega}{\partial t} \vec{t}_s + \frac{1}{1 + \frac{t}{R}} \frac{\partial \omega}{\partial s} \vec{t}_t$$

where $\vec{t}_s$ and $\vec{t}_t$ are unit vectors in the s and t directions, respectively. By using the appropriate relations for the divergence and gradient in this curvilinear coordinate system and

$$\vec{q} \times \vec{\omega} = - q_s \omega \vec{t}_t + q_t \omega \vec{t}_s \quad ,$$

we obtain the following component form of the Navier-Stokes equations, where the kinematic viscosity has been normalized to be proportional to the reciprocal of the Reynolds number, ε:

Continuity

$$\frac{\partial q_s}{\partial s} + \frac{\partial}{\partial t} \left[\left(1 + \frac{t}{R}\right) q_t \right] = 0 \qquad \text{(1a)}$$

Momentum

$$q_s \frac{\partial q_s}{\partial s} + (1 + \frac{t}{R})q_t \frac{\partial q_s}{\partial t} + \frac{q_t q_s}{R} = - \frac{\partial p}{\partial s} - \varepsilon(1 + \frac{t}{R}) \frac{\partial \omega}{\partial t} \qquad (1b)$$

$$\frac{q_s}{1 + \frac{t}{R}} \frac{\partial q_t}{\partial s} + q_t \frac{\partial q_t}{\partial t} - \frac{q_s^2}{R + t} = - \frac{\partial p}{\partial t} - \frac{\varepsilon}{1 + \frac{t}{R}} \frac{\partial \omega}{\partial s} \qquad (1c)$$

$$\omega = \frac{1}{1 + \frac{t}{R}} \frac{\partial q_t}{\partial s} - \frac{\partial q_s}{\partial t} - \frac{q_s}{R + t} \quad .$$

The boundary layer equations for this curvilinear network are obtained using the following limit process asymptotic expressions for the flow variables:

$$q_s = u_1(s,t^*) + \sqrt{\varepsilon}\, u_2(s,t^*) + \cdots \qquad (2a)$$

$$q_t = \sqrt{\varepsilon}\, v_1(s,t^*) + \varepsilon v_2(s,t^*) + \cdots \qquad (2b)$$

$$p = p_1(s) + \sqrt{\varepsilon}\, p_2(s,t^*) + \cdots \qquad (2c)$$

$$\varepsilon \to 0 \quad , \quad s,t^* \text{ fixed} \quad . \qquad (2d)$$

Substitution of (2) into (1) gives the following hierarchies on retention of the indicated orders of terms:

$$\mathcal{O}(1): \quad u_1 \frac{\partial u_1}{\partial s} + v_1 \frac{\partial u_1}{\partial t^*} = - \frac{\partial p_1(s)}{\partial s} + \frac{\partial^2 u_1}{\partial t^{*2}} \qquad (3a)$$

$$\mathcal{O}(\frac{1}{\sqrt{\varepsilon}}): \quad 0 = - \frac{\partial p_1}{\partial t^*} \Rightarrow p_1 = p_1(s) \qquad (3b)$$

$$\mathcal{O}(\sqrt{\varepsilon}): \quad u_1 \frac{\partial u_2}{\partial s} + u_2 \frac{\partial u_1}{\partial s} + v_1 \frac{\partial u_2}{\partial t^*} + v_2 \frac{\partial u_1}{\partial t^*} + \frac{t^*}{R} v_2 \frac{\partial u_1}{\partial t^*} + \frac{u_1 v_1}{R} = - \frac{\partial p_2}{\partial s} \qquad (4a)$$

$$\mathcal{O}(1): \quad -\frac{u_1^2}{R} = -\frac{\partial p_2}{\partial t^*} \tag{4b}$$

$$\mathcal{O}(1): \quad \frac{\partial u_1}{\partial s} + \frac{\partial v_1}{\partial s} = 0 \tag{5a}$$

$$\mathcal{O}(\sqrt{\varepsilon}): \quad \frac{\partial u_2}{\partial s} + \frac{\partial v_2}{\partial t^*} + \frac{\partial}{\partial t^*}\left(\frac{t^* v_1}{R}\right) = 0 \quad . \tag{5b}$$

For the outer inviscid flow, the appropriate asymptotic expansions are written as

$$q_s = U_1(s,t) + \sqrt{\varepsilon}\, U_2(s,t) + \cdots \tag{6a}$$

$$q_t = V_1(s,t) + \sqrt{\varepsilon}\, V_2(s,t) + \cdots \tag{6b}$$

$$p = P_1(s,t) + \sqrt{\varepsilon}\, P_2(s,t) + \cdots \tag{6c}$$

for

$$\varepsilon \to 0 \quad , \quad t,s \text{ fixed} \quad . \tag{6d}$$

On substitution of (6) into (1) and retention of the indicated orders, the following equations for the approximate quantities in (6) are obtained:

$$\mathcal{O}(1): \quad U_1 \frac{\partial U_1}{\partial s} + \left(1 + \frac{t}{R}\right) V_1 \frac{\partial U_1}{\partial t} = -\frac{\partial P_1}{\partial s} \tag{7a}$$

$$\frac{U_1}{1 + \frac{t}{R}} \frac{\partial V_1}{\partial s} + V_1 \frac{\partial V_1}{\partial t} - \frac{U_1^2}{R} = -\frac{\partial P_1}{\partial t} \tag{7b}$$

$$\frac{\partial U_1}{\partial s} + \left(1 + \frac{t}{R}\right) \frac{\partial V_1}{\partial t} - \frac{V_1}{R} = 0 \tag{7c}$$

$$\mathcal{O}(\sqrt{\varepsilon}): \quad U_1 \frac{\partial U_2}{\partial s} + U_2 \frac{\partial U_1}{\partial s} + \left(1 + \frac{\tau}{R}\right)\left(V_1 \frac{\partial U_1}{\partial t} + U_1 \frac{\partial V_1}{\partial t}\right)$$

$$+ \frac{V_1 U_2 + V_2 V_1}{R} = - \frac{\partial P_2}{\partial s} \tag{8a}$$

$$\frac{U_1 \frac{\partial V_2}{\partial s} + U_2 \frac{\partial V_1}{\partial s}}{1 + \frac{t}{R}} + V_1 \frac{\partial V_2}{\partial t} + V_2 \frac{\partial V_1}{\partial t} - \frac{2U_1 U_2}{R} = - \frac{\partial P_2}{\partial t} \tag{8b}$$

$$\frac{\partial U_2}{\partial s} + \left(1 + \frac{t}{R}\right) \frac{\partial V_2}{\partial t} + \frac{V_2}{R} = 0 \quad . \tag{8c}$$

The appropriate matching between the inviscid and viscous regions is obtained by writing the expression for both regions in intermediate variables and equating like terms. The appropriate intermediate variable is defined as

$$t_\eta = \frac{t}{\eta(\varepsilon)} \quad ; \quad \text{where} \quad \varepsilon \ll \eta(\varepsilon) \ll 1 \quad . \tag{9}$$

Thus:

$$t^* = \frac{t}{\sqrt{\varepsilon}} \quad , \quad t = \eta t_\eta \to 0$$

$$t^* = \frac{\eta}{\sqrt{\varepsilon}} t_\eta \to \infty \quad .$$

Matching

By using the process indicated, the inner (viscous) and outer inviscid representations are matching schematically, indicated by $\leftrightarrow$ (asymptotic equality) as follows:

$$P_1(s,\eta t_\eta) + \sqrt{\varepsilon}\, P_2(s,\eta t_\eta) \leftrightarrow p_1(s) + \sqrt{\varepsilon}\, p_2\, s, \frac{\eta}{\sqrt{\varepsilon}} t_\eta + \cdots$$

or

$$P_1(s,0) + \eta t_\eta \frac{\partial P_1}{\partial t}(s,0) + \cdots + \sqrt{\varepsilon}\, P_2(s,0) + \sqrt{\varepsilon} \frac{\partial P_2}{\partial t} \eta t_\eta + \cdots$$

$$\leftrightarrow p_1(s) + \sqrt{\varepsilon} \lim_{t\to\infty} p_2(s,t) + \cdots$$

which for matching implies

$$p_1(s) = P_1(s,0) \tag{10a}$$

$$p_2(s,t) = \frac{\partial P_1}{\partial t}(s,0)t + P_2(s,0) \tag{10b}$$

and for $t \to \infty$

$$p_2(s,t) \to \frac{U_1^2(s,0)}{R(s)}\, t + P_2(s,0) \quad . \tag{10c}$$

For the vertical velocity component, we have analogously

$$V_1(s,\eta t_\eta) + \sqrt{\varepsilon}\, V_2(s,\eta t_\eta) + \cdots \leftrightarrow \sqrt{\varepsilon}\, V_1(s,\frac{\eta}{\sqrt{\varepsilon}} t_\eta) + \varepsilon v_2(s,\frac{\eta}{\sqrt{\varepsilon}} t_\eta) + \cdots$$

$$V_1(s,0) + \eta t_\eta \frac{\partial V_1}{\partial t}(s,0) + \sqrt{\varepsilon}\, V_2(s,0) + \cdots \leftrightarrow \sqrt{\varepsilon}\, v_1(s,\frac{\eta}{\sqrt{\varepsilon}} t_\eta) + \cdots \quad . \tag{11}$$

For compatibility with the boundary conditions, we assert that $V_1(s,0) = 0$. From (11), we have finally,

$$V_2(s,0) = \lim_{t^*\to\infty} \left\{ v_1(s,t) - t^* \frac{\partial V_1}{\partial t}(s,0) \right\}$$

$$= \lim_{t^*\to\infty} \left\{ v_1(s,t) + t^* \frac{\partial U_1}{\partial s}(s,0) \right\}$$

$$V_2(s,0) = \lim_{t^*\to\infty} \frac{\partial}{\partial s} \int_0^{t^*} (U_1(s,0) - u_1(s,\tau))d\tau = \frac{d\delta^*}{ds} \tag{12}$$

δ^* = displacement thickness $= \int_0^\infty [U_e - u_1(s,\tau)]d\tau$, $U_e \equiv U_1(s,0)$

where by virtue of (5a) the following relation has been used to obtain the displacement thickness integral in (12)

$$v_1 = \int_0^{t^*} \frac{\partial u_1}{\partial s}(s,\tau)d\tau \quad .$$

Pressure Jump Conditions on Wake and Boundary Layer

Referring to Fig. C2, we consider the section AB of the wake. The viscous interaction with the inviscid portion of the solution will be effected by pressure jump conditions related to the momentum defect in the viscous layers. This defect plays the role of the classical Spence blowing coefficient utilized in our jet flap algorithm. To see this, we recall from previously derived relations that

$$P_2(s,t^*) \to \frac{\partial P_1}{\partial t}(s,0)t^* + P_2(s,0-) \quad , \quad t^* \to \infty$$

$$P_2(s,t^*) \to \frac{\partial P_1}{\partial t}(s,0)t^* + P_2(s,0-) \quad , \quad t^* \to -\infty$$

$$\frac{\partial p_2}{\partial t^*}(s,t^*) = \frac{u_1^2(s,t^*)}{R(s)} \quad .$$

On integration:

$$p_2(s,t^*) - p_2(s,0) = \frac{1}{R}\int_0^{t^*} u_1^2(s,t^*)dt^* \quad .$$

Also,

$$\frac{\partial P_1}{\partial t}(s,0+) = \frac{1}{R}U_1^2(s,0+)$$

$$\frac{\partial P_1}{\partial t}(s,0-) = \frac{1}{R}U_1^2(s,0-)$$

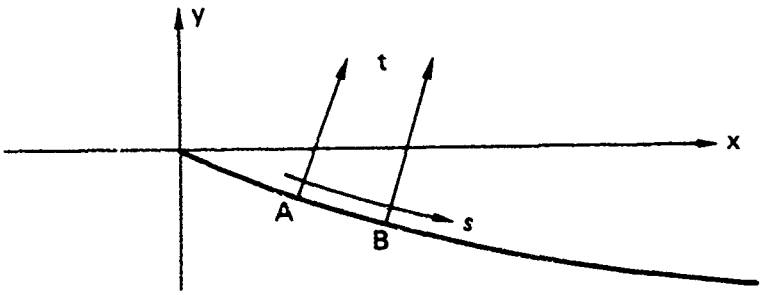

Fig. C2 Section of wake.

so that,

$$\lim_{t \to \infty} \frac{1}{R} \int_0^{t^*} u_1^2(s,\tau(d\tau + \frac{1}{R}\, t^* U_1^2(s,0+) + P_2(s,0+) + p_2(s,0)$$

$$\lim_{t \to -\infty} \frac{1}{R} \int_0^{t^*} u_1^2(s,\tau) d\tau + \frac{1}{R}\, t^* U_1^2(s,0-) + P_2(s,0-) + p_2(s,0) \quad .$$

But,

$$P_1(s,0+) = P_1(s,0-)$$

by matching

$$\frac{\partial p_1}{\partial s} = 0 \quad ,$$

and by Bernoulli

$$P_1(s) + \frac{U_1^2}{2} = \text{constant} \quad .$$

Thus:

$$U_1^2(s,0+) = U_1^2(s,0-) = U_e^2(s)$$

where e signifies external conditions.

By virtue of these relations, we obtain

$$P_2(s,0+) - P_2(s,0-) = \left[P_2\right]_{\text{wake}} = \frac{1}{R}\left\{\int_0^{t_1^*} u_1^2(s,\tau)d\tau - \int_0^{t_2^*} u_1^2(s,\tau)d\tau - (t_1^* - t_2^*)U_e^2\right\}$$

or

$$\left[P_2\right] = \frac{1}{2}\int_{t_2^* \to -\infty}^{t_1 \to +\infty} [u_1^2(s,\tau) - U_e^2(s,\tau)]d\tau$$

$$= \frac{1}{R}\int_{-\omega}^{\infty} [u_1 - U_e][u_1 + U_e]d\tau$$

$$= \frac{1}{R}\int_{-\infty}^{\infty} (u_1 - U_e)u_1 d\tau + \frac{U_e}{R}\int_{-\infty}^{\infty} (u_2 - U_e)d\tau = -\frac{\theta + \delta^*}{R} \qquad (13)$$

where

$$\theta = \int_{-\infty}^{\infty} (U_e - u_1)u_1 = \text{momentum thickness} \quad .$$

Analogous results to (13) can be obtained for the compressible case from (4b), by recognizing that the significant difference will be folding the density factor inside the integrands of δ^* and θ in the appropriate definitions of these thicknesses, and by employing the adiabatic energy invariant rather than Bernoulli to obtain the relationship of P_1 and U_1 in the outer flow.

Rockwell International
Science Center

SC5055.21FR

DISTRIBUTION LIST FOR UNCLASSIFIED
TECHNICAL REPORTS AND REPRINTS ISSUED UNDER
CONTRACT N00014-76-C-0352 TASK 061-264

All addresses receive one copy unless otherwise specified

Technical Library
Building 313
Ballistic Research Laboratories
Aberdeen Proving Ground, MD 21005

Mr. Aviars Celmins
Ballistic Research Laboratory
Ballistic Modelling Division
Aberdeen Proving Ground, MD 21005

Dr. P. J. Roache
Ecodynamics Research Associates, Inc.
P. O. Box 8172
Albuquerque, NM 87108

Defense Documentation Center
Cameron Station, Building 5
Alexandria, VA 22314 — 12 copies

Library
Naval Academy
Annapolis, MD 21402

Director, Tactical Technology Office
Defense Advanced Research Projects Agency
1400 Wilson Boulevard
Arlington, VA 22209

Code 211
Office of Naval Research
800 N. Quincy Street
Arlington, VA 22217

Code 436
Office of Naval Research
800 N. Quincy Street
Arlington, VA 22217 — 2 copies

Dr. J. L. Potter
Deputy Director, Technology
von Karman Gas Dynamics Facility
Arnold Air Force Station, TN 37389

Professor J. C. Wu
School of Aerospace Engineering
Georgia Institute of Technology
Atlanta, GA 30332

Library
Aerojet-General Corporation
6352 North Irwindale Avenue
Azusa, CA 91702

NASA Scientific and Technical Information Facility
P. O. Box 8757
Baltimore/Washington International Airport, MD 21240

Dr. K. C. Wang
Martin Marietta Corporation
Martin Marietta Laboratories
1450 South Rolling Road
Baltimore, MD 21227

Professor A. J. Chorin
Department Mathematics
University of California
Berkeley, CA 94720

Professor M. Holt
Department of Mechanical Engineering
University of California
Berkeley, CA 94720

Dr. H. R. Chaplin
Code 1600
David W. Taylor Naval Ship Research and Development Center
Bethesda, MD 20084

Dr. Hans Lugt
Code 1802
David W. Taylor Naval Ship Research and Development Center
Bethesda, MD 20084

Dr. Francois Frenkiel
Code 1802
David W. Taylor Naval Ship Research and Development Center
Bethesda, MD 20084

Dr. G. R. Inger
Department of Aerospace Engineering
Virginia Polytechnic Institute and
State University
Blacksburg, VA 24061

Professor C. H. Lewis
Department of Aerospace and Ocean
Engineering
Virginia Polytechnic Institute and
State University
Blacksburg, VA 24061

Professor A. H. Nayfeh
Department of Engineering Science
Virginia Polytechnic Institute and
State University
Blacksburg, VA 24061

Dr. A. Rubel
Research Department
Grumman Aerospace Corporation
Bethpage, NY 11714

Commanding Officer
Office of Naval Research Branch Office
666 Summer Street, Bldg. 114, Section D
Boston, MA 02210

Dr. J. C. Erickson, Jr.
CALSPAN Corporation
Advanced Technology Center
P. O. Box 400
Buffalo, NY 14225

Dr. T. J. Falk
CALSPAN Corporation
Advanced Technology Center
P. O. Box 400
Buffalo, NY 14225

Dr. C. Witliff
CALSPAN Corporation
Advanced Technology Center
P. O. Box 400
Buffalo, NY 14225

Professor R. F. Probstein
Department of Mechanical Engineering
Massachusetts Institute of Technology
Cambridge, MA 02139

Commanding Officer
Office of Naval Research
Branch Office
536 South Clark Street
Chicago, IL 60605

Code 753
Naval Weapons Center
China Lake, CA 93555

SC5055.21FR

Mr. J. Marshall
Code 4063
Naval Weapons Center
China Lake, CA 93555

Professor R. T. Davis
Department of Aerospace Engineering
University of Cincinnati
Cincinnati, OH 45221

Professor S. G. Rubin
Department of Aerospace Engineering
and Applied Mechanics
University of Cincinnati
Cincinnati, OH 45221

Library MS 60-3
NASA Lewis Research Center
21000 Brookpark Road
Cleveland, OH 44135

Dr. J. D. Anderson, Jr.
Chairman, Department of Aerospace
Engineering
College of Engineering
University of Maryland
College Park MD 20742

Professor O. Burggraf
Department of Aeronautical and
Astronautical Engineering
Ohio State University
1314 Kinnear Road
Columbus, OH 43212

Technical Library
Naval Surface Weapons Center
Dahlgren Laboratory
Dahlgren, VA 22448

Dr. F. Moore
Naval Surface Weapons Center
Dahlgren Laboratory
Dahlgren, VA 22448

Technical Library 2-51131
LTV Aerospace Corporation
P. O. Box 5907
Dallas, TX 75222

Library, United Aircraft Corporation
Research Laboratories
Silver Lane
East Hartford, CT 06108

Professor G. Moretti
Polytechnic Institute of New York Long
Island Center
Department of Aerospace Engineering and
Applied Mechanics
Route 110
Framingdale, NY 11735

Dr. W. R. Briley
Scientific Research Associates, Inc.
P. O. Box 498
Glastonbury, CT 06033

Professor P. Gordon
Calumet Campus
Department of Mathematics
Purdue University
Hammond, IN 46323

Library (MS 185)
NASA Langley Research Center
Langley Station
Hampton, VA 23665

Professor A. Chapmann
Chairman, Mechanical Engineering
Department
William M. Rice Institute
Box 1892
Houston, TX 77001

Technical Library
Naval Ordnance Station
Indian Head, MD 20640

Professor D. A. Caughey
Sibley School of Mechanical and
Aerospace Engineering
Cornell University
Ithaca, NY 14850

Professor E. L. Resler
Sibley School of Mechanical and
Aerospace Engineering
Cornell University
Ithaca, NY 14850

Professor S. F. Shen
Sibley School of Mechanical and
Aerospace Engineering
Cornell University
Ithaca, NY 14850

Library
Midwest Research Institute
425 Volker Boulevard
Kansas City, MO 64110

Dr. M. M. Hafez
Flow Research, Inc.
P. O. Box 5040
Kent, WA 98031

Dr. E. M. Murman
Flow Research, Inc.
P. O. Box 5040
Kent, WA 98031

Dr. J. J. Riley
Flow Research, Inc.
P. O. Box 5040
Kent, WA 98031

Dr. S. A. Orszag
Cambridge Hydrodynamics, Inc.
54 Baskin Road
Lexington, MA 02173

Dr. P. Bradshaw
Imperial College of Science and
Technology
Department of Aeronautics
Prince Consort Road
London SW7 2BY, England

Professor T. Cebeci
Mechanical Engineering Department
California State University, Long
Beach
Long Beach , CA 90840

Dr. H. K. Cheng
University of Southern California,
Department of Aerospace Engineering
University Park
Los Angeles, CA 90007

Professor J. D. Cole
Mechanics and Structures Department
School of Engineering and Applied Science
University of California
Los Angeles, CA 90024

Engineering Library
University of Southern California
Box 77929
Los Angeles, CA 90007

Dr. C. -M. Ho
Department of Aerospace Engineering
University of Southern California
University Park
Los Angeles, CA 90007

Dr. T. D. Taylor
The Aerospace Corporation
P. O. Box 92957
Los Angeles, CA 90009

Commanding Officer
Naval Ordnance Station
Louisville, KY 40214

Mr. B. H. Little, Jr.
Lockheed-Georgia Company
Department 72-74, Zone 369
Marietta, GA 30061

Professor E. R. G. Eckert
University of Minnesota
241 Mechanical Engineering Building
Minneapolis, MN 55455

Dr. Gary Chapman
Mail Stop 227-4
Ames Research Center
Moffett Field, CA 94035

Library
Naval Postgraduate School
Monterey, CA 93940

Dr. J. L. Steger
Flow Simulations, Inc.
735 Alice Avenue
Mountain View, CA 94041

Dr. S. S. Stahara
Nielsen Engineering and Research, Inc.
510 Clyde Avenue
Moutain View, CA 94043

Engineering Societies Library
345 East 47th Street
New York, NY 10017

Professor A. Jameson
Courant Institute of Mathematical Sciences
New York University
251 Mercer Street
New York, NY 10012

Professor G. Miller
Department of Applied Science
New York University
26-36 Stuyvesant Street
New York, NY 10003

Office of Naval Research
New York Area Office
715 Broadway - 5th Floor
New York, NY 10003

Dr. A. Veglio-Laurin
Department of Applied Science
New York University
26-36 Stuyvesant Street
New York, NY 10003

Mr. D. Farmer
Naval Ocean Research and Development Activity
Code 332
NSTL Station, MS 39522

Librarian, Aeronautical Library
National Research Council
Montreal Road
Ottawa 7, Canada

Lockheed Missiles and Space Company
Technical Information Center
3251 Hanover Street
Palo Alto, CA 94304

Commanding Officer
Office of Naval Research Branch Office
1030 East Green Street
Pasadena, CA 91106

Engineering Division
California Institute of Technology
Pasadena, CA 91109

Library
Jet Propulsion Laboratory
4800 Oak Grove Drive
Pasadena, CA 91103

Professor H. Liepmann
Department of Aeronautics
California Institute of Technology
Pasadena, CA 91109

Mr. L. I. Chasen, MGR-MSD Lib.
General Electric Company
Missile and Space Division
P. O. Box 8555
Philadelphia, PA 19101

Technical Library
Naval Missile Center
Point Mugu, CA 93042

Professor S. Bogdonoff
Gas Dynamics Laboratory
Department of Aerospace and
Mechanical Sciences
Princeton University
Princeton, NJ 08540

Professor S. I. Cheng
Department of Aerospace and
Mechanical Sciences
Princeton University
Princeton, NJ 08540

Dr. J. E. Yates
Aeronautical Research Associates
of Princeton, Inc.
50 Washington Road
Princeton, NJ 08540

Professor L. Sirovich
Division of Applied Mathematics
Brown University
Providence, RI 02912

Redstone Scientific Information Center
Chief, Document Section
Army Missile Command
Redstone Arsenal, AL 35809

U.S. Army Research Office
P. O. Box 12211
Research Triangle, NC 27709

Editor, Applied Mechanics Review
Southwest Research Institute
8500 Culebra Road
San Antonio, TX 78228

Library and Information Services
General Dynamics-CONVAIR
P. O. Box 1128
San Diego, CA 92112

Dr. R. Magnus
General Dynamics-CONVAIR
Kearny Mesa Plant
P. O. Box 80847
San Diego, CA 92138

Office of Naval Research
San Francisco Area Office
One Hallidie Plaza, Suite 601
San Francisco, CA 94102

Library
The RAND Corporation
1700 Main Street
Santa Monica, CA 90401

Dr. P. E. Rubbert
Boeing Aerospace Company
Boeing Military Airplane Development
Organization
P. O. Box 3707
Seattle, WA 98124

Dr. H. Yoshihara
Boeing Aerospace Company
P. O. Box 3999
Mail Stop 41-18
Seattle, WA 98124

Librarian
Naval Surface Weapons Center
White Oak Laboratory
Silver Spring, MD 20910

Dr. J. M. Solomon
Naval Surface Weapons Center
White Oak Laboratory
Silver Spring, MD 20910

Professor J. H. Ferziger
Department of Mechanical Engineering
Stanford University
Stanford, CA 94305

Professor K. Karamcheti
Department of Aeronautics and Astronautics
Stanford University
Stanford, CA 94305

Professor O. Bunemann
Institute for Plasma Research
Stanford University
Stanford, CA 94305

Engineering Library
McDonnell Douglas Corporation
Department 218, Building 101
P. O. Box 516
St. Louis, MO 63166

Dr. R. J. Hakkinen
McDonnell Douglas Corporation
Department 222
P. O. Box 516
St. Louis, MO 63166

Dr. N. Malmuth
Rockwell International Science Center
1049 Camino Dos Rios
P. O. Box 1085
Thousand Oaks, CA 91360

Library
Institute of Aerospace Studies
University of Toronto
Toronto 5, Canada

Professor W. R. Sears
Aerospace and Mechanical Engineering
University of Arizona
Tucson, AZ 85721

Professor A. R. Seebass
Department of Aerospace and Mechanical Engineering
University of Arizona
Tucson, AZ 85721

Dr. K. T. Yen
Code 3015
Naval Air Development Center
Warminster, PA 18974

Air Force Office of Scientific Research (SREM)
Building 1410, Bolling AFB
Washington, DC 20332

Chief of Research and Development
Office of Chief of Staff
Department of the Army
Washington, DC 20310

Library of Congress
Science and Technology Division
Washington, DC 20540

Director of Research (Code RR)
National Aeronautics and Space Administration
600 Independence Avenue, SW
Washington, DC 20546

Library
National Bureau of Standards
Washington, DC 20234

National Science Foundation
Engineering Division
1800 G Street, NW
Washington, DC 20550

AIR 320D
Naval Air Systems Command
Washington, DC 20361

AIR 950D
Naval Air Systems Command
Washington, DC 20375

Code 2627
Naval Research Laboratory
Washington, DC 20375

SEA 03512
Naval Sea Systems Command
Washington, DC 20362

SEA 09G3
Naval Sea Systems Command
Washington, DC 20362

Dr. A. L. Slafkosky
Scientific Advisor
Commandant of the Marine Corps
(Code AX)
Washington, DC 20380

Director
Weapons Systems Evaluation Group
Washington, DC 20350

Research Library
AVCO Corporation
Missile Systems Division
201 Lovell Street
Wilmington, MA 01887

AFAPL (AFSC)
AB
Wright Patterson, AFB, OH 45433

Dr. Donald J. Harney
AFFDL/FX
Wright Patterson AFB, OH 45433